M_5Si_3 (M=Ti, Nb, Mo) based transition-metal silicides for high temperature applications

by

Zhihong Tang

A dissertation submitted to the graduate faculty

in partial fulfillment of the requirements for the degree of

DOCTOR OF PHILOSOPHY

Major: Materials Science and Engineering

Program of Study Committee:
Mufit Akinc, Co-major Professor
Matthew J. Kramer, Co-major Professor
Alan I. Goldman
Brian Gleeson
Kurt Robert Hebert
Xiaoli Tan

Iowa State University

Ames, Iowa

2007

TABLE OF CONTENTS

List of Figures

List of Tables

Abstract

Transition metal silicides are being considered for future engine turbine components at temperatures up to 1600ºC. Although significant improvement in high temperature strength, room temperature fracture toughness has been realized in the past decade, further improvement in oxidation resistance is needed.

Oxidation mechanism of Ti_5Si_3-based alloys was investigated. Oxidation behavior of Ti_5Si_3-based alloy strongly depends on the atmosphere. Presence of Nitrogen alters the oxidation behavior of Ti_5Si_3 by nucleation and growth of nitride subscale. $Ti_5Si_{3.2}$ and $Ti_5Si_3C_{0.5}$ alloys exhibited an excellent oxidation resistance in nitrogen bearing atmosphere due to limited dissolution of nitrogen and increased Si/Ti activity ratio.

$MoSi_2$ coating developed by pack cementation to protect Mo-based Mo-Si-B composites was found to be effective up to 1500ºC. Shifting coating composition to T1+T2+Mo_3Si region showed the possibility to extend the coating lifetime above 1500ºC by more than ten times via formation of slow growing Mo_3Si or T2 interlayer without sacrificing the oxidation resistance of the coating.

The phase equilibria in the Nb-rich portion of Nb-B system has been evaluated experimentally using metallographic analysis and differential thermal analyzer (DTA). It was shown that Nb_{ss} (solid solution) and NbB are the only two primary phases in the 0-40 at.% B composition range, and the eutectic reaction $L \leftrightarrow Nb_{ss} + NbB$ was determined to occur at 2104±5˚C by DTA.

Chapter 1. General Introduction

Dissertation Organization

The dissertation is organized in an alternate format, such that it is composed of four original manuscripts which have already been published or are to be submitted for publication. The manuscript chapters are preceded by a general introduction and followed by general conclusions.

The general introduction gives a broad overview of high-temperature structural materials developed in the last few decades, including Ni_3Al, NiAl, γ-TiAl, Ti_5Si_3, and Mo-Si-B *in-situ* composites, as well as the motivation of this research. The first manuscript "Role of nitrogen on the oxidative stability of Ti_5Si_3 based alloys at elevated temperature", which has been published in *Intermetallics* in 2006. The second manuscript, "Mechanism of high temperature oxidation of Ti_5Si_3-based alloys", will be submitted to *Intermetallics* in 2007. The third manuscript, "Characterization and oxidation behavior of silicide coating on multiphase Mo-Si-B alloys", will also be submitted to *Intermetallics* in 2007. The fourth manuscript, "Evaluation of phase equilibria in the Nb-rich portion of Nb-B system", will be submitted to *Intermetallics* in 2007.

The general conclusions section summarizes the most important results of these studies and gives suggestions for future research.

Although all four manuscripts are largely the work of the dissertation author, the work was benefited by the contributions of co-authors. Dr. Mufit Akinc made a significant contribution as major professor and appears as a co-author on all four papers. Dr. Matthew J. Kramer is also included as co-author on several papers for his guidance and oversight. I must

also mention that the technical discussion and critical assessments by Dr. Andrew Thom, a significant contributor to this dissertation, are greatly appreciated.

An Overview of High Temperature Materials beyond Nickel-based Superalloys

Introduction

Nickel-based superalloys exhibit an exceptional combination of high-temperature strength, toughness, and resistance to degradation in aggressive environments including nitridation, carbonization, oxidation and sulfidation[1]. Currently, the vast majority of use is found in aircraft and power generation turbines, rocket engines and other challenging environments, including nuclear power and chemical processing plants. Superalloys were initially developed for use on aircraft piston engine components, and their development over the last 70 years has been paced by the demands of advancing gas-turbine engine technology. Advances in the processing of Ni-based superalloys have allowed evolution of microstructure from equiaxed structures three to four decades ago, to directionally solidified (DS) multi-grain and single crystal (SC) components today. With added capacity from compositional flexibility coupled with processing over that time period, high pressure turbine blade temperatures have increased by 125ºC. Metal surface temperatures at the hottest locations on state-of-the-art jet engine airfoils now approach 1150ºC. Thermal barrier coatings (TBC's) provide insulation from the hot gas, so that TBC surface temperatures are appreciably higher[2]. The most severe combination of stress and temperature in present engine designs corresponds to bulk average metal temperatures approaching 1000ºC, using first- and second-

generation single crystal alloys. These materials, which were developed in 1970's and 1980's, rely on the use of substantial additions of W, Ta, Mo and Re to strengthen the γ and γ' phases[3]. The concentration of the sum of these elements has been further increased in the third- and fourth-generation single crystal, to >20 wt.%. From the standpoint of strength, the newest superalloys may allow metal surface temperature of 1200ºC and bulk average temperatures of 1050ºC[4].

Substantial improvement beyond the fourth-generation single-crystal alloys will be very difficult to implement for Ni-based systems. Most advanced superalloys melt at approximately 1350ºC. Depending on processing and heat treatment, chemical segregation in the superalloys can lead to incipient melting at ~1270ºC. The interaction zone created between the bond coating (such as NiAl or Pt-modified NiAl) and the single-crystal airfoil can also lead to reduction in melting point, to <1250ºC[4]. In service, the TBC may be lost due to foreign object damage or excessive growth of the protective alumina scale. Once the TBC is lost, the nominal maximum local metal surface temperature may rise above 1200ºC, and incipient melting of alloy may occur. Single crystal superalloy strength levels may be improved to allow bulk temperatures in excess of 1050ºC, but any increase toward a 1200ºC metal surface temperature may require substantial gains in TBC damage tolerance and reliability. Consequently, the attainment of improvement in engine efficiency and thrust-to-weight ratio is very much dependant on the development of new materials systems[4].

There are only four categories of materials that can be considered: refractory alloys, structural ceramics, structural intermetallics, and refractory metal-intermetallic composites. Alloys based on high-melting or refractory elements with superior high-temperature creep strength, such as TZM (Mo-0.5Ti-0.08Zr-0.03C, wt.%) or niobium alloys, may be considered,

but the poor oxidation resistance is unacceptable and has restricted their application in low-temperature or non-oxidizing high-temperature environments. Several ceramic materials with superior environmental stability, such as $MoSi_2$ or Si_3N_4 could potentially meet the temperature requirements; however, there is little evidence to suggest that an adequate balance of mechanical properties can be readily achieved for fracture-critical, dynamically loaded components. These materials will have limited applications in turbine engines without further development of improved materials and innovative system architectures. Structural intermetallics and refractory metal-intermetallic composites have stimulated great interest due to a combination of promising properties, and a great deal of fundamental and engineering research has been made aiming at implementation of these materials in aerospace, automotive and land-based applications. The recent progress and current status of the research and development of these high-temperature intermetallics and composites are summarized in the following sections. Their emerging applications are also reviewed.

Aluminides

Alloys based on ordered intermetallic compounds constitute a unique class of metallic materials that form long-range ordered crystal structures below a critical temperature. These compounds generally exhibit promising high-temperature properties, because the long-range ordered superlattice lowers the dislocation mobility and diffusion processes at elevated temperatures. However, the intermetallics have been mainly used as strengthening constituents in structural materials because of the brittleness. For example, Ni-based superalloys owe their outstanding strength properties to a fine dispersion of ordered γ'-Ni_3Al-based precipitates embedded in a ductile, disordered matrix of γ-Ni. Research in 1980's and 1990's focused on understanding the brittle fracture and low ductility observed in ordered

intermetallics. Alloying and processing have been employed to control the ordered crystal structure, microstructure features, grain-boundary structure, and composition to overcome the brittleness problem of the ordered intermetallics. Success in this work has inspired parallel efforts aimed at improving high-temperature mechanical properties. The results have led to the development of a number of attractive intermetallic alloys having useful ductility and strength. Some intermetallics, such as γ-TiAl based alloys, have advanced to the commercialization stage for structural applications at 550-750ºC service temperature regime in advance turbine engines. The following sections summarize the research and development for several promising structural intermetallics: Ni_3Al, NiAl, γ-TiAl, and Ti_5Si_3.

Ni_3Al

Ni_3Al has an LI_2 crystal structure, a derivative of the fcc crystal structure, as shown in Fig.1[3]. Ni_3Al is of interest because of its excellent strength and oxidation resistance at elevated temperatures. Ni_3Al is also the most important strengthening constituent in Ni-based superalloys. Single crystals of Ni_3Al are ductile at ambient temperatures, but polycrystalline Ni_3Al fails by brittle grain-boundary facture with very little plasticity. A study of ductility and strength of Ni_3Al has lead to the development of ductile nickel aluminide alloys for structural applications with the following composition range (in atomic percent)[5]

Ni-(14-18)Al-(6-9)Cr-(1-4)Mo-(0.01-0.15)Zr/Hf-(0.01-0.20)B

In these alloys, 6 to 9 at.% Cr is added to reduce the environmental embitterment in oxidizing environments at elevated temperature. Zr and Hf additions most effectively improve high-temperature strength via solid solution hardening effects. Mo additions improve strength at ambient and elevated temperature. Micro-alloying with B reduces moisture-induced hydrogen embitterment and enhances grain-boundary cohesive strength, resulting in sharply

increased ductility at ambient temperatures. The yield strength of cast Ni_3Al alloy is stronger than Ni-based superalloys at elevated temperature. The Ni_3Al alloy generally possesses ductility of 25 to 40 % at temperatures up to 700ºC, and 15 to 30 % at up to 1000ºC in air. The creep properties of Ni_3Al alloys are dependent on the stress, temperature, composition and grain size [6]. In general, the creep resistance of Ni_3Al is comparable to that of most of the nickel-based superalloys.

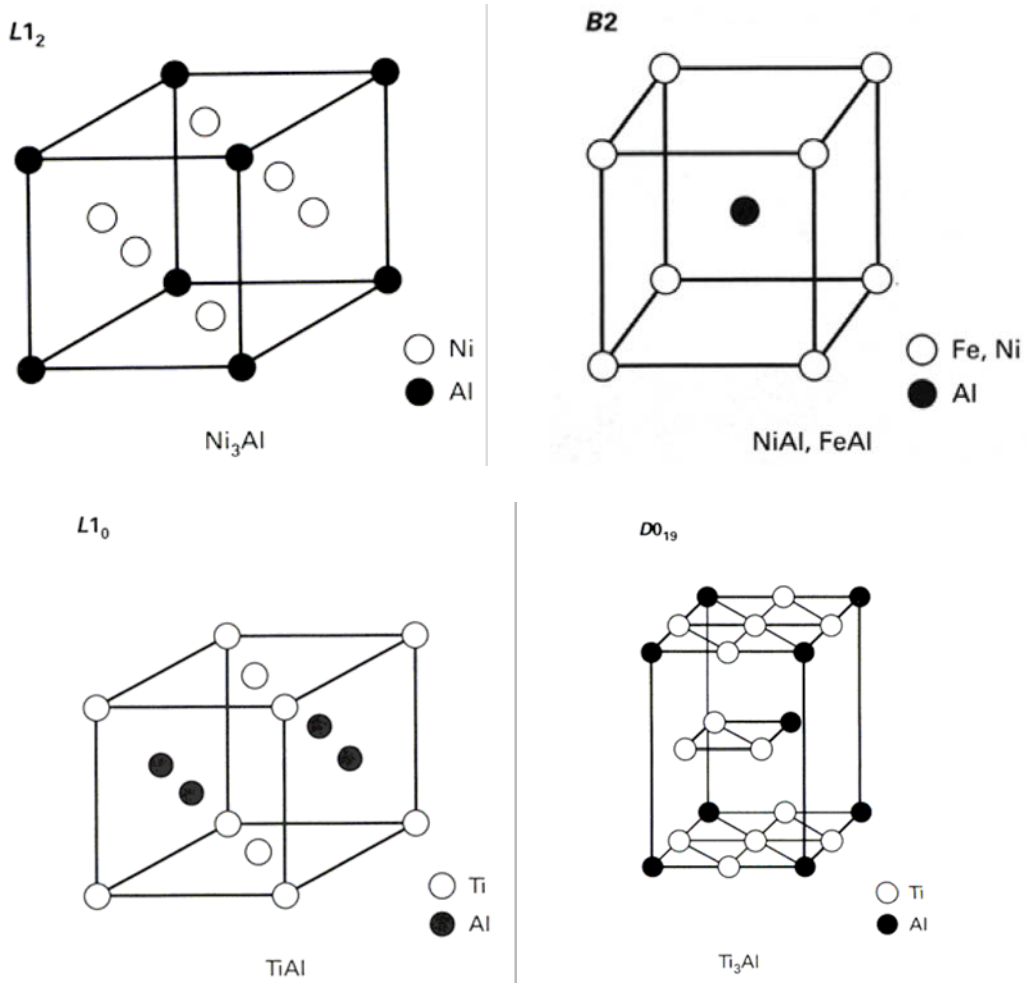

Figure 1 The crystal structure of Ni_3Al, NiAl, TiAl and $TiAl_3$

Although the properties of alloys based on Ni_3Al approach those of established superalloys, the Ni_3Al alloys are unlikely replace superalloys in aircraft engine application. The opportunity exists, however, in corrosion-related structural applications [7, 8]. This is because oxidation and carburization resistance are high, as is wear resistance. The current and potential applications of cast components include: 1) heat-treating trays and fixtures for carburizing and air environments, 2) radiant burner tubes for heat-treating furnace, 3) muffles for heat-treating furnace in hydrogen or inert gas annealing, 4) transfer rolls for austenitizing furnace in steel mills, 5) forging dies for close die forging of steel components[7, 9].

NiAl

Nickel Aluminide containing more than about 40 at.% Ni starts to form a single phase B2-type ordered crystal structure based on the bcc lattice. NiAl appears very attractive on a specific strength basis for such application as high-temperature gas turbine airfoils for a number of reasons. First, β-NiAl is a much higher melting compound in the same binary phase diagram that γ/γ' superalloys derive and NiAl has been used for years as oxidation resistant coating for Ni-based superalloys. In addition to these advantages, NiAl has a density (5.9 g/cm^3) that is approximately 2/3 that of Ni-based superalloys, a thermal conductivity which is 4 to 8 times greater than superalloys, and it is relatively easy to process and machine by conventional techniques. An additional advantage is the ability to attain high-temperature creep resistance in NiAl alloys, a benefit that has been realized in the last several years and represents one of greatest achievements in current alloy design.

Unfortunately, the structural use of NiAl is hindered by poor fracture toughness and tensile ductility at low temperature [10, 11]. NiAl exhibits mainly $\{100\}$ slip, rather than $\{111\}$ slip as commonly observed for bcc materials. The lack of sufficient slip systems has

been regarded as the major cause of low ductility in NiAl. It has been reported that the brittleness of NiAl may not be overcome without modifying the slip systems[11].

γ-TiAl based alloys

γ-TiAl alloys are attractive due to their low density, high modulus, high creep and oxidation resistance compared to other Ti-based alloys. The **γ-**TiAl phase has an $L1_0$ ordered face-centered tetragonal structure, which has a wide range (49 to 66 at.% Al) of temperature-dependent stability. The currently investigated **γ-**TiAl based alloys of engineering importance are two-phase alloys with Al content from 44 to 48at.%, which consists of major γ phase and minor α_2 phase [12].

Single-phase γ-TiAl is brittle; however, aluminum-lean alloys containing a small amount of Ti_3Al (α_2) are found to be more ductile. The optimum ductility occurs at about 10 vol.% α_2; when the α_2 phase exceeds 20 vol.%, the ductility goes down [13]. Small addition of V, Cr, or Mn increases the ductility of two-phase **γ-**TiAl based alloy [14]. For a given two-phase alloy composition, microstructure variations directly influence the RT tensile ductility, which range from 0.5-4% plastic elongation. The highest tensile ductility results from fine-grain duplex (DP) materials with uniform grain size and fracture strains ranging from 2-4% in as-machined conditions. In general, fully lamellar (FL) microstructures both in wrought alloys and cast alloys exhibit poor ductility and low room-temperature strength. However, refinement in lamellar grain size by thermal-mechanical treatment or small addition of boron increases both strength and ductility. The ability of deform plastically in γ-TiAl based alloys at room temperature (between 1 to 4% ductility) enable to reduce the local stress concentrations, and are quite important in structural design.

Room-temperature fracture toughness values of wrought alloys range from 10-16 $MPa\sqrt{m}$ for duplex microstructures, and from 20-35 $MPa\sqrt{m}$ for FL microstructures depending on grain sizes[15, 16]. As-cast alloys shows properties similar to those of FL wrought alloys: high fracture toughness and low strength/ductility. However, cast ingot alloy specimen often show large variations of fracture toughness values; for example, K_{IC}=12-20 $MPa\sqrt{m}$, probably due to the large-grained, textured, and nonuniform cast microstructure.

Creep properties of γ-TiAl based alloy in duplex forms measured at a temperature of 700-950ºC are better than those of superalloy IN718 when normalized by density. Lamellar (both FL and RFL) structure show drastic improvements in creep resistance over duplex microstructure at all temperatures. The superior creep resistance for lamellar structure was originally explained in term of composite-like strengthening. In spite of extensive investigation, however, the fundamental mechanism in FL materials is basically unknown. The creep behavior resembles that for high-temperature in two phases materials, indicating the deformation anisotropy in the lamellar structure may play an important role.

In general, TiAl alloys promise to extend the temperature capability of titanium-based materials and to replace much heavier Ni-based superalloys in some applications with a materials one-half the density. A major effort has been made over the last 20 or so years to introduce γ-TiAl based alloys into the market-place for structural applications for 560-750ºC service in advance aircraft turbine engines and automotive industry. Gas turbine engine applications for TiAl include compressor blades, vanes, shrounds, turbine disk cover plates, blade outer air seals, and low pressure blades. Also under consideration are large static structures, such as diffusers, ducts and cases [17, 18].

Ti_5Si_3

Crystal structure

Ti_5Si_3 is an attractive silicide compound due to its high melting point (~2130ºC), low density (4.3g/cm^3), and capacity to retain high strength up to and beyond 1200ºC [19]. In binary Ti-Si phase diagram, Ti_5Si_3 has a homogeneity range of 4 at.%, as shown in Fig.2.

Ti_5Si_3 possesses a complex hexagonal D_8^8 structure representing the space group $P6_3/mcm$ (Pearson symbol hp16). The compound contains two formula units per unit cell, and belongs to the Mn_5Si_3 prototype structure shown in Fig.3 [20, 21]. The D_8^8 structure is built up by two atomic species, which occupy three different crystallographic positions. The structure consists of two chains of titanium atoms: one being a linear chain of Ti (1) atoms, the other being a chain of face-shared octahedra formed by six Ti (2) atoms. The Si atoms surround octahedrally the Ti (2) atoms. The octahedral interstices along the c-axis may be partially or completely filled by an interstitial element. According to published data [21], the diameter of this interstitial hole is approximately 1.34 Å, which is large enough to accommodate second period elements. In fact, several experimental studies [21-24] have shown that a significant amount of boron, carbon, nitrogen and oxygen can dissolve in the Ti_5Si_3, and solubility of C, N or O in Ti_5Si_3 is about 8-10 at.%. Also, work done on compounds with identical Mn_5Si_3-type crystal structures by Corbett et al.[25] has shown that atoms as massive as fourth-period elements can be incorporated into the interstitial position, resulting in a significant expansion of the lattice. Thus Ti_5Si_3 presents a wealth of potential interstitial chemistries by alloying with a wide variety and substantial amount of Z elements. The resulting $Ti_5Si_3Z_x$ ($x \leq 1$) compound retains the Mn_5Si_3 type structure. Thermodynamic

calculations showed that the additions of these interstitial elements can lower the Gibbs free energy of formation and stabilize the Ti_5Si_3 hexagonal phase, as shown in Table 1.

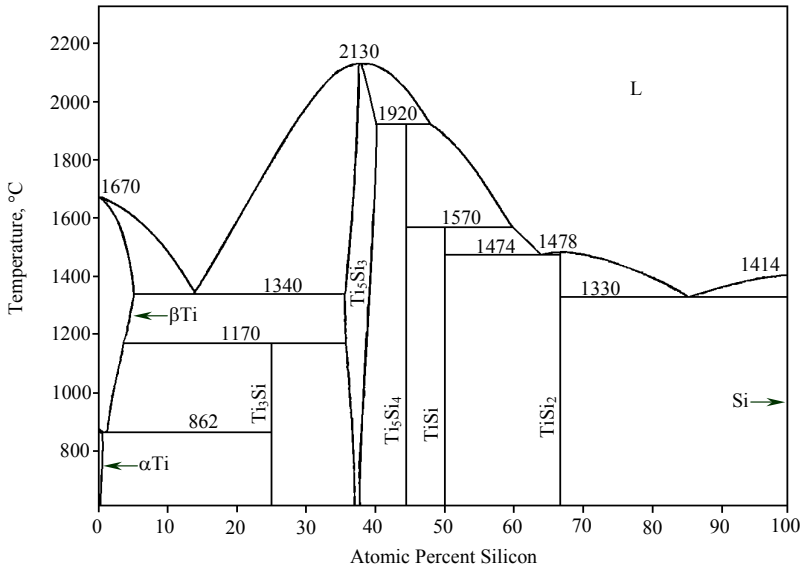

Figure 2 Ti-Si binary phase diagram

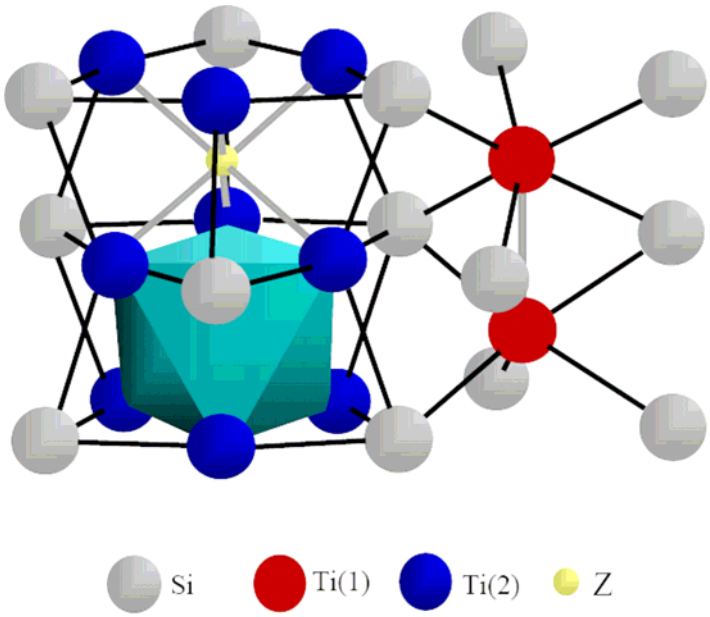

Figure 3 Portion of the Ti_5Si_3Z crystal structure, illustrating stacking of the anti-prisms along the c-axis

Table 1 Calculated Gibbs energy of formation, $\Delta G_f^{\circ}(kJ/g \cdot at.)$ for $Ti_5Si_3Z_X$ at 1100°C

Ti_5Si_3	Ti_5Si_3C	Ti_5Si_3N	Ti_5Si_3O
-73.7	-77.2	-82.0	-104.0

Two recent studies by Radhakrishnan et al.[26] and Thom et al.[27] highlighted the difficulty of synthesizing and consolidating Ti_5Si_3 without carbon, nitrogen and/or oxygen. In particular, studies that use metal powder as a staring material are likely to result in oxygen impurity of at least one or two weight percent. Thus, the sample purity must be carefully considered when studying the properties of Ti_5Si_3.

Physical and mechanical properties

The thermal expansion coefficient of Ti_5Si_3 has been investigated, but considerable scattering exists [28-32]. The only consistent result between these studies is that the coefficient of thermal expansion (CTE) along the c-axis is significantly larger than that along the a-axis. The scatters in the data were attributed to the impurities in the samples. Most measurements have been done with the interstitially doped sample. Williams *et al*. [28] measured the linear coefficient of thermal expansion of a pure sample via arc-melting, the CTE along a axis is $5.9\pm0.2 \times 10^{-6}$ °C, while the CTE along c-axis is $16.9\pm0.6 \times 10^{-6}$ °C. Thus there is a large thermal anisotropy with α_c/α_a 2.9±0.2. The interstitial and substitutional addition of B, C, N and O altered the bonding in Ti_5Si_3 so as to lower the thermal expansion anisotropy. For instance, the addition of 6.25 at.% B, 6.25 at.% C, 6.25 at.% N and 5 at.% O reduce thermal expansion anisotropy of Ti_5Si_3 by as much as 31%, 34%, 28% and 14% respectively [28].

Frommeyer *et al*.[33] measured the Young's modulus in the temperature range from 20°C to 1000°C using the resonance frequency method. Ti_5Si_3 shows a small decrease in Young's modulus with increasing temperature. At room temperature and at 1000°C, the elastic modulus of Ti_5Si_3 is about 156GPa and 141GPa, respectively. Ti_5Si_3 alloy exhibits a much higher Young's modulus-to-density ratio (36.3 GPa·cm^3/g) than do nickel base superalloys (for example, carpenter MP35N, 27.6 GPa·cm^3/g).

Room temperature fracture toughness of the coarse-grained (20-50μm) Ti_5Si_3 was found to be 2.1 MPa m$^{1/2}$, while that of fine-grained (5-6μm) specimens has been reported to be about 2.7 or 3.2 MPa m$^{1/2}$, depending on processing conditions[34]. R-curve behavior suggests improvement in fracture toughness with reduction in grain size. While the fracture toughness of the coarse-grained (20–50μm) samples increased to 7.5 $MPa\sqrt{m}$ at 800ºC, it increased to about 12 $MPa\sqrt{m}$ for fine-grained samples (5-6 μm). Thus grain size reduction is helpful in improving fracture toughness more significantly at elevated temperatures.

Ti_5Si_3 behaves brittle at deformation temperatures below 950°C and no macroscopic ductility has been observed even under compressive loads. The ductile-to-brittle transition occurs in the temperature range from 850°C to 950°C. At the test temperature of 1000°C a remarkable high flow stress of about 1048 MPa was determined. Crack initiation occurred after plastic deformation of about 1.5%. The flow stress of Ti_5Si_3 drops drastically to 250 MPa and 50 MPa at 1300°C and 1500°C [20, 34]. TEM studies showed dislocations and a large number of deformation twin.

Oxidation behavior

It has been shown that Ti_5Si_3 possesses good oxidation up to 850ºC. However, published studies on the oxidation resistance of Ti_5Si_3 above 850ºC have shown considerable scatter, as shown in Table 2. Studies by Thom et al. [35, 36], Kim et al.[37] and Abba et al.[38] have reported poor oxidation resistance in air above 850 ºC, while studies by Mitra et al. [19] and Taniguchi et al. [39] reported excellent oxidation resistance in air up to 1250 ºC. One of the explanations for the discrepancies in oxidation behavior of Ti_5Si_3 is the slight variation in alloy composition and alloy synthesis methods employed in those studies. The samples prepared by Thom et al.[35, 36], Kim et al.[37] and Abba et al. [38] were all reported to be single phase and assumed to be stoichiometric Ti_5Si_3. Those samples formed a mixed rutile-silica scale in contact with the base alloy upon exposure to air, and poor oxidation resistance was reported. The studies that reported excellent oxidation resistance for Ti_5Si_3 at 1200 ºC reported that their samples contained a small amount of silicon-rich phases (Ti_5Si_4 or $TiSi_2$). These silicon-rich samples exhibited excellent oxidation resistance in air due to the formation of a continuous and protective SiO_2 scale.

Though there are some discrepancies, most studies reported totally different oxidation resistance behavior in air versus in pure oxygen or Ar-21% O_2. For example, Williams et al. [40] reported that Ti_5Si_3 shows slow parabolic oxidation kinetics in pure oxygen at 1000ºC while a “breakaway oxidation” is observed after 12 hours exposure to air. This, so called “nitrogen effect” is well established, but the underlying mechanism still remains unknown.

Table 2 Summary of oxidation behavior of Ti_5Si_3-based alloys at elevated temperatures

Composition	Processing Method	Oxidation Temp., ºC	Atmosphere	Oxidation behavior		Ref.
				Model	K[1]	
Ti_5Si_3	HIP	1000	Air	Cracking		[35]
Ti_5Si_3 coating on Ti	Deposition of Si	950	Air	Breakaway oxidation		[38]
Ti_5Si_3 with Ti_5Si_4 & TiSi	E-beam melting	1200	Air	Cubic	8×10^{-11}	[39]
Ti_5Si_3 with ~5% TiSi	Hot pressing of TiH_2/Si powder	1200	Air	Parabolic	5×10^{-3}	[19]
Ti_5Si_3	Arc-melting	1000	Ar-21%O_2	Parabolic	2×10^{-3}	[40]
Ti_5Si_3	Arc-melting	1000	Air	Breakaway oxidation after 12 hours		[40]
$Ti_5Si_{3.2}$	Arc-melting	1000	Air	Parabolic	5×10^{-5}	[40]
$Ti_5Si_3C_{0.5}$	Arc-melting	1000	Air	Parabolic	5×10^{-5}	[40]

[1]rate constant, for a parabolic model, $mg^2/cm^4/hr$; for a cubic model, $mg^3/cm^6/hr$.

Another contributing factor regarding the oxidation behavior of Ti_5Si_3 is that the samples used in most studies were assumed to be contaminated with interstitial impurity atoms because of the open Mn_5Si_3 prototype structure of Ti_5Si_3. Two recent studies by Radhakrishnan et al. [26] and Thom et al.[27] highlighted the difficulty of synthesizing and consolidating Ti_5Si_3 without contamination by carbon, nitrogen and/or oxygen by powder metallurgy. In particular, studies that use metal powder as a staring material are highly likely to contain an oxygen impurity of at least one or two weight percent. Furthermore, studies [40, 41] on the oxidation behavior of oxygen- or carbon-doped Ti_5Si_3 suggested that the addition of oxygen or carbon promote the formation of thin silica layer in the early stage of oxidation. However, only alloying with carbon showed dramatic improvement for the long-term oxidation resistance. Though the underlying mechanism of the improvement in oxidation resistance due to carbon addition remains largely unknown, preferential bonding of carbon to titanium, which decreases the activity of Ti while increasing the activity of Si in the alloy,

was offered as a plausible mechanism. Unfortunately, most previous studies on the oxidation behavior of Ti_5Si_3 also suffered from interstitial impurities. Thus intrinsic oxidation behavior of stoichiometric Ti_5Si_3, the effect of ternary addition on the oxidation mechanism and influence of gas composition on the oxidation rate and oxide scale formation remain unclear.

Mo-Si-B *in-situ* composites

Molybdenum-based alloys such as TZM (Mo-0.5Ti-0.08Zr-0.03C (all compositions expressed in weight percent), and others without Si or B additions, are well established high-temperature materials for inert environments because of their excellent strength at elevated temperatures. However, the utility of molybdenum alloys in jet engines has been limited by its susceptibility to oxidation. When molybdenum or molybdenum alloys are exposed to oxygen at temperatures in excess of about 800ºC, the molybdenum is rapidly oxidized to molybdenum trioxide and vaporized from the surface; resulting in shrinkage and eventually disintegration of the molybdenum or molybdenum alloys. Alternatively, $MoSi_2$-based compounds are long known to provide outstanding oxidation resistance at extremely high temperatures as a result of SiO_2 formation. However, extensive study of these alloys shows there is no feasible path that can provide both an oxidation-resistant $MoSi_2$ alloy combined with the creep and fracture resistance required for structural design. Thus, there has been diminishing interest in $MoSi_2$ alloys for the last several years. The silicide Mo_5Si_3 has a somewhat higher melting point than $MoSi_2$ and appears to be more creep resistance than $MoSi_2$. However, its oxidation resistance is significantly inferior to $MoSi_2$. The oxidation resistance of Mo_5Si_3 can be greatly improved with the addition of 1-2 wt.% boron due to the formation of a protective boronsilicate glass [45]. This approach resulted in significant efforts for the development of oxidation-resistant Mo-Si-B alloys. These alloys are typically

multi-phase composites and provide a SiO_2-based oxidation-protection mechanism which is distinctly different from that of the traditional Mo-based alloys. They also exhibit adequate creep and fracture resistance[42]. The following is a review of recent progress in the development of Mo-Si-B *in-situ* composites for elevated temperature applications.

Crystal structure and phase equilibria

Most molybdenum silicides except Mo_3Si are non-cubic and highly anisotropic, as shown in Fig.4. Mo_3Si has a cubic A15 structure comprising eight atoms in the unit cell, with six atoms of Mo and two atoms of Si, while $MoSi_2$ has a body centered tetragonal (bct) structure ($C11_b$) with eight atoms in the unit cell. The bct structure of $MoSi_2$ has a fixed c/a ratio of 2.452, and appears to have three bcc unit cells stacked with the body centered site being occupied by alternating Mo or Si. Mo_5Si_3 (T1 phase) have a body-centered tetragonal $D8_m$ structure. The tetragonal structure of Mo_5Si_3 is quite different with respect to that of $MoSi_2$, as the former exhibits the following characteristics: i) the a-lattice parameter is larger than its c-lattice parameter ($a/c<2$), ii) close-packed planes are absent, and iii) the –Si–Mo–Si– chains are along the [100] and [010] directions, while the –Mo–Mo– and –Si–Si–chains are along the [001] direction. New Ternary Mo_5SiB_2 phase has the $D8_l$ structure, which has a body-centered tetragonal unit cell (space group *I*4*/mcm*). The unit cell contains 32 atoms, with 20 Mo, 4 Si, and 8 B atoms situated in layered arrangements. Three types of layers were identified: layer A, having only Mo atoms; layer B, having only Si atoms; and layer C, having a mixture of Mo and B atoms. The structure arrangement of these layers in T2 may be viewed as a means to achieve efficient atomic packing between metal atoms such as Mo and metalloid constituents (Si and B in this case).

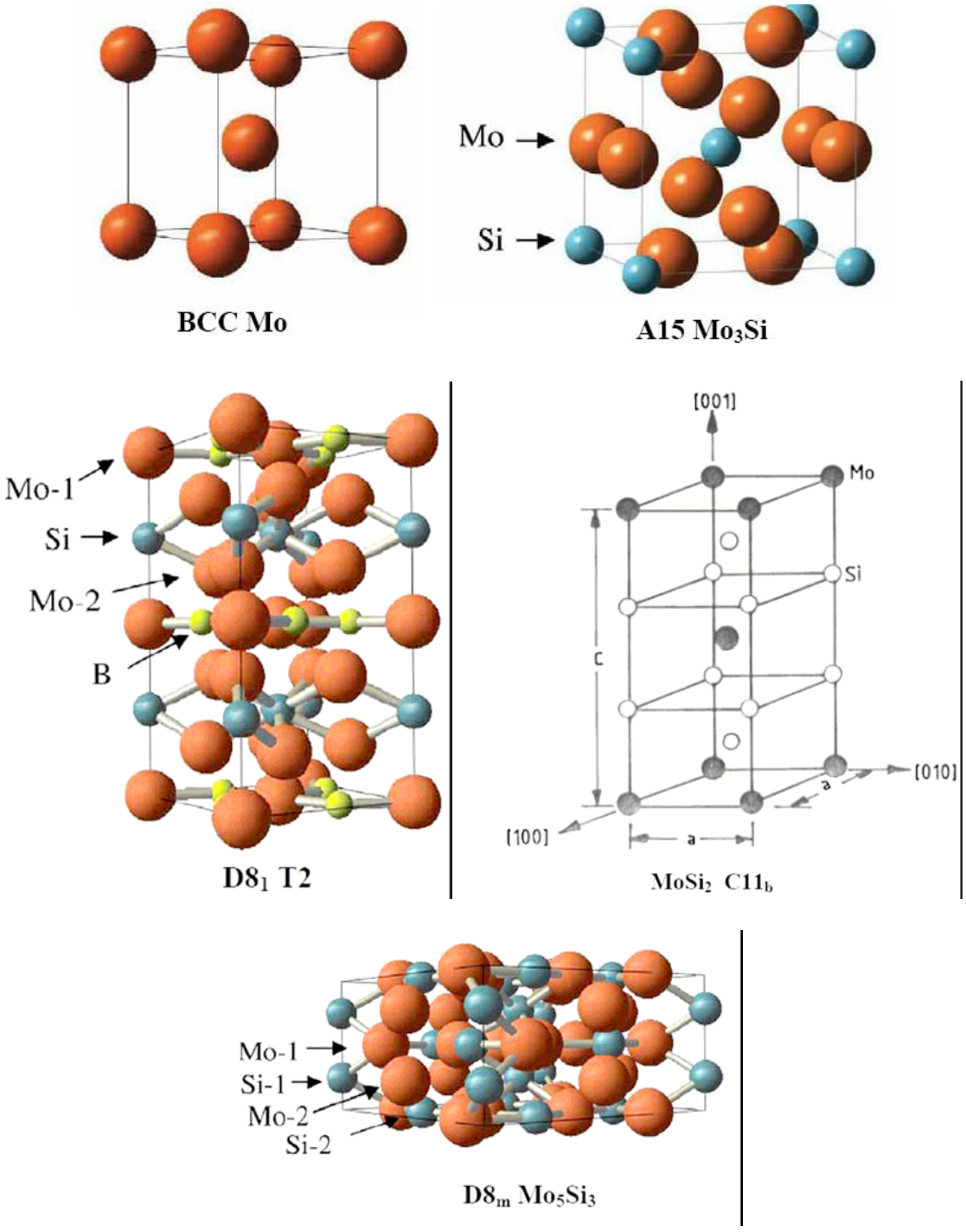

Figure 4 Crystal structures of phases present in Mo-Si-B systems: bcc (Mo); A15 (Mo3Si); $D8_1$ (Mo_5SiB_2); $C11_b$ ($MoSi_2$); and $D8_m$ (Mo_5Si_3)

The Mo-rich section of the ternary isothermal phase diagram of Mo-Si-B system is well established and shown in Fig.5. The BCC-Mo(ss) phase has a negligible B solubility, but appreciable Si solubility of about 3 at.% Si. Both Mo_3Si and $MoSi_2$ are stoichiometric compounds with a negligible solubility of B and Si. Mo_5Si_3Bx (T1 phase) with a body-centered tetragonal $D8_m$ structure has a homogeneity range of 3 at.% Si and a limited B solubility. Boron solubility in the T1 phase was estimated to be about 4.5±5 at% in an earlier study by Nowotny et al.[43]. However, a recent study by Huebsch [44] indicated that boron solubility in $Mo_{5+y}Si_{3-y}$ at 1800ºC reaches a maximum value of approximately 2 at.% in a narrow region within the homogeneity range of $-0.08 \le y \le 0.04$. The ternary Mo_5SiB_2 (T2) phase also has a modest homogeneity range. The compositional variation in the T2 phase with respect to the B:Si ratio in the off-stoichiometric region is mainly toward B-rich values, which is indicated by B:Si ratio values greater than 2.0. The variation in the Mo content is limited. From the standpoint of the phase equilibria, the Mo-rich section of the Mo-Si-B system is attractive in that it consists of simple mixtures of nearly line compounds (only slight solubility range) with stability to 1600°C or higher.

Alloy development

As indicated in the schematic ternary phase diagram in Fig.5, two main alloy systems have been examined to date. The first one, which was developed by Akinc and his coworkers [45], is $Mo_5Si_3B_x$ (T1)-based composites consisting of either T1+T2+Mo_3Si or T1+MoB+$MoSi_2$. They exhibit excellent oxidation resistance at elevated temperatures up to 1600ºC, which is comparable to that of $MoSi_2$. The addition of boron is critical for the excellent oxidation resistance provide by a protective boronsilicate glass scale. The second system has mostly investigated and pioneered by Berczik et al.[46] in 1997, and consists of

α-Mo, Mo_3Si and Mo_5SiB_2 (T2) phases. While these alloys are not as oxidation resistant as T1-based Mo-Si-B composites, they contain a relatively ductile phase, α-Mo. Depending on its volume fraction and distribution, the α-Mo can significantly improve the room- and high-temperature fracture toughness. Recently, two-phase alloys with T2/Mo_{ss} eutectic microstructure showed a good balance between room temperature (RT) fracture toughness and high-temperature strength [47, 48]. However, the synthesis of eutectic microstructure is difficult due to occurrence of composition segregation in the as-cast alloy, for example, the formation of MoB and Mo_2B.

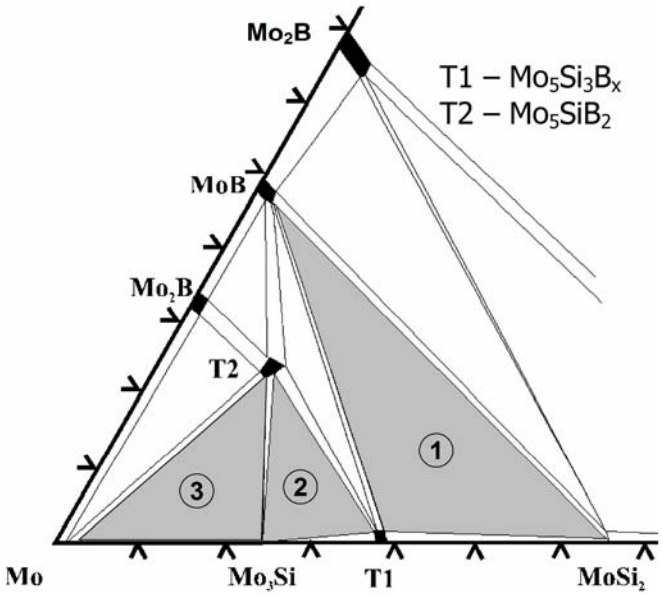

Figure 5 Mo-rich section of the ternary Mo-Si-B system at 1600°C

Mechanical properties

Molybdenum silicides such as $MoSi_2$, Mo_5Si_3, Mo_3Si and Mo_5SiB_2 possess a low room temperature fracture toughness ranged between 2 and 3 $MPa\sqrt{m}$ mainly due to low symmetry which does not allow plastic deformation through dislocation formation and

movement. The low fracture toughness of Mo_5Si_3 and Mo_5SiB_2 is also due to anisotropy in the coefficient of thermal expansion along c- and a-axes, which contributes to internal residual stress. However, the fracture toughness of multiphase Mo-Si-B composites has been significantly improved by the existence of ductile α-Mo phase.

A significant volume fraction (17-49%) of the α-Mo phase leads to toughening of molybdenum silicides. Fracture toughness of 7–15 $MPa\sqrt{m}$ has been observed at room temperature in Mo-Mo_3Si-Mo_5SiB_2 composites, as shown in Fig.6. There is a trend of increasing toughness with higher α-Mo volume fraction. The high toughness of these alloys was attributed to a combination of crack trapping at the α-Mo phase, which raised the initiation toughness, and crack bridging in the crack wake, which contributed to the rising R-curve behavior. Both mechanisms were promoted by the presence of the continuous α-Mo matrix. If the α-Mo particles are coarse and form a continuous network, a considerable improvement in fracture toughness to a range of 15–21 $MPa\sqrt{m}$ and a more prominent R-curve behavior with crack extension has been observed, as crack-trapping by the α-Mo particles leads to enhanced damage tolerance[49, 50]. It has also been observed that an alloy with 30 vol.-% of coarse α-Mo particles shows much higher fracture toughness, compared to the alloy with about 50 vol.% fine α-Mo particles, suggesting the importance of the size of the dispersed ductile phase, as shown in Fig.7.[49, 51]

In general, high fracture toughness values are achieved with a large volume fraction of a continuous, coarse α-Mo phase. Unfortunately, the high fracture toughness values afforded by high α-Mo volume fractions are at the expense of oxidation resistance. Good oxidation resistance is achieved by low volume fractions of α-Mo. The requirements for high fracture toughness thus run opposite to those for good oxidation resistance. Recently,

Schneibel et al.[52] have shown that improvement in ductility of the α-Mo particles by alloying with Zr, or addition of $MgAl_2O_4$ particles reduces the volume fraction of α-Mo required for the improvement of fracture toughness and hold promise for a combination of adequate fracture toughness and oxidation resistance.

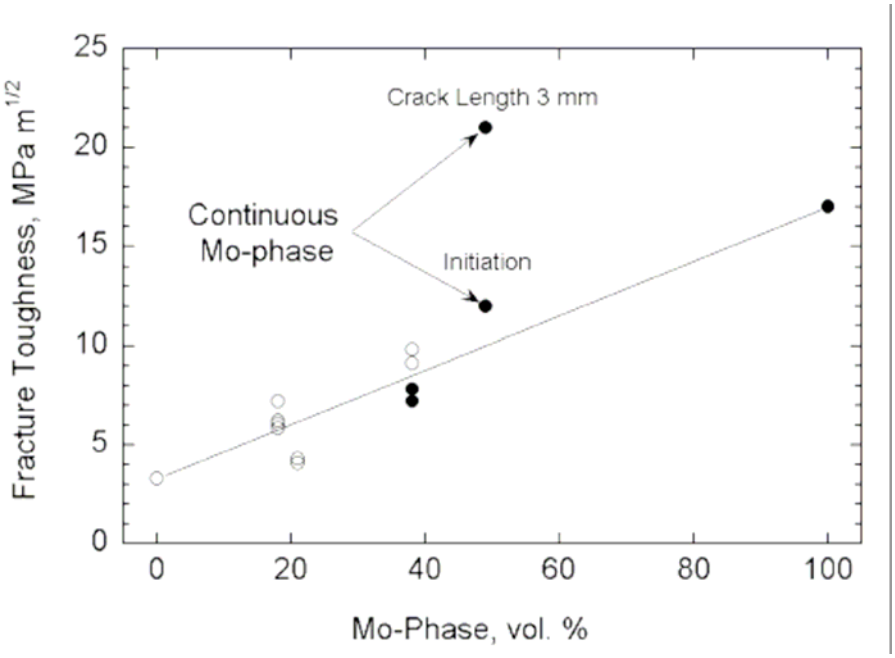

Figure 6 Room-temperature fracture toughness as a function of the α-Mo volume fraction. Solid and open symbols denote standard and nonstandard tests, respectively

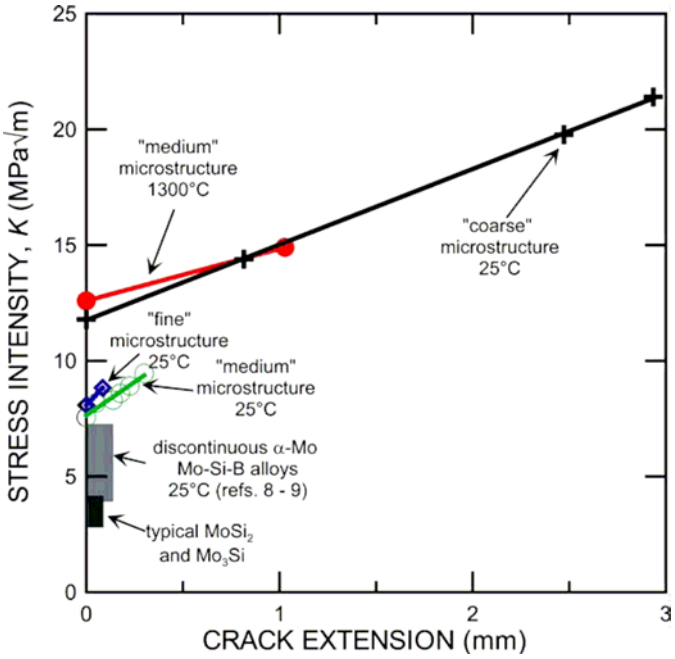

(a)

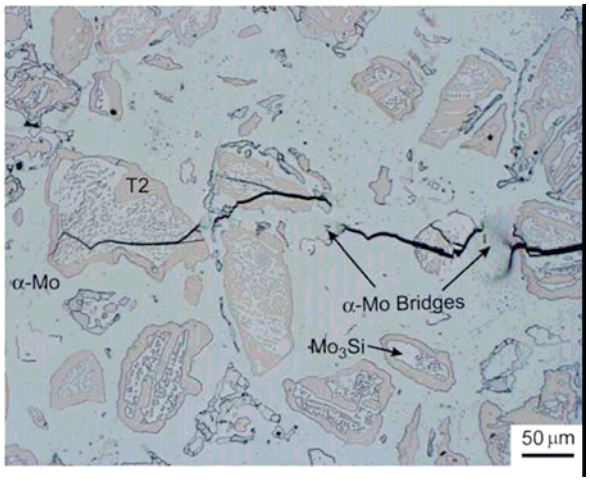

(b)

Figure 7 a) R-curves showing the fracture resistance of the continuous α-Mo matrix Mo–Si–B alloys. Additionally shown are previously reported values for unreinforced molybdenum silicides and Mo–Si–B alloys with a discontinuous α-Mo phase; b) Crack trapping and bridging at the α-Mo phase in the‘‘coarse’’ Mo–Si–B alloy. The crack locally arrests at the α-Mo phase, leaving α-Mo bridges in the crack wake

Limited information[53, 54] is available on the high-temperature yield and flow behavior of the Mo–Si–B alloys, containing Mo_5SiB_2, Mo_3Si and α-Mo phases. The Mo–Si–B alloys containing 40–50 vol.-% of the α-Mo phase have shown tensile or compressive yield strengths in the range of 480–580 MPa, when tested between 1200 and 1400ºC at strain rates of 10^{-4} or 10^{-1} s^{-1}. Apparently, the high temperature strength is sensitive to the composition and volume fraction of the constituent phases in the alloy. Tensile ductility of about 100% could be observed on testing at 1400ºC with a strain rate of 10^{-4} s^{-1}, probably because of the high volume fraction of a-Mo in the alloy with composition of Mo–9.4Si–13.8B. On the other hand, tensile ductility of the Mo–8.9Si–7.7B alloy containing approximately 55 vol.-% α-Mo has been found to be 5% at 1200ºC and almost zero at 1100°C[55]. Processing has also been found to play an important role in controlling the morphology and orientation of α-Mo particles, and therefore tensile behavior[56]. The near-continuous network of α-Mo formed in the Mo–8.9Si–7.7B alloy through extrusion has led to reduction of the BDTT by 200ºC, with respect to that of HIPed alloy of similar composition but with discontinuously distributed α-Mo.

The first report[57] on creep testing of Mo–Si–B multiphase alloys is a study on a material with B-doped Mo_5Si_3 (T1) as the matrix, and dispersion of Mo_3Si and Mo_5SiB_2 (T2) phases. For compression creep at temperatures in the range of 1220–1320ºC and stresses in the range of 140–180 MPa, the stress exponents have been found to be in the range of 3.8–5.0, and the activation energy to be around 400 kJ mol^{-1}, as shown in Fig.8. The values of stress exponent suggest a dislocation glide and climb based mechanism, which is supported by observation of a high density of dislocations in the Mo_3Si phase. However, little dislocation activity could be observed in the T1 matrix phase.

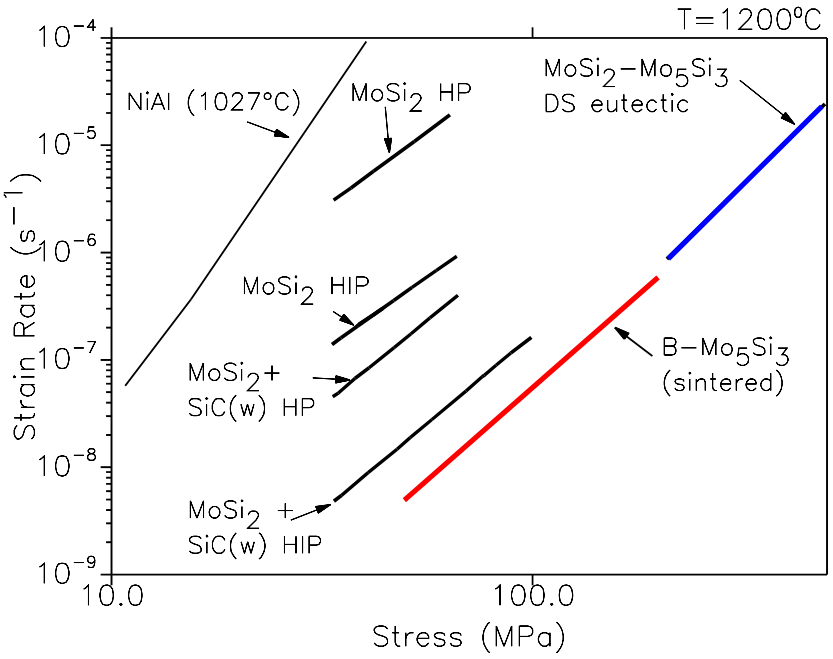

Figure 8 Creep rate at 1200°C for Mo_5Si_3-Mo_3Si-T2 composites

Schneibel et al.[54] studied the dependence of the compressive creep strength of Mo-Mo_3Si-T2 composites on the α-Mo volume fraction. The creep strengths were defined as the stress reached at 2% plastic deformation in constant displacement experiments with an initial strain rate of 10^{-5} s^{-1} (see Fig.9). For simplicity, the contribution of the Mo_3Si/T2 ratio on the creep strength has been ignored. The solid circles correspond to microstructures with individual α-Mo particles, as well as a pure Mo specimen, and have been fitted by a straight line, while the open circles correspond to a continuous α-Mo phase. The creep strength of pure Mo was extrapolated from creep experiments carried out at 1200 °C and 69 MPa, which resulted in a strain rate of 6×10^{-5} s^{-1}. As shown in Fig.9, a decrease in the α-Mo volume fraction, *i.e.*, an increase in the Mo_3Si-Mo_5SiB_2 volume fraction, gives rise to substantial

creep strengthening. If the α-Mo is present in the form of a continuous matrix, the creep strength is relatively low.

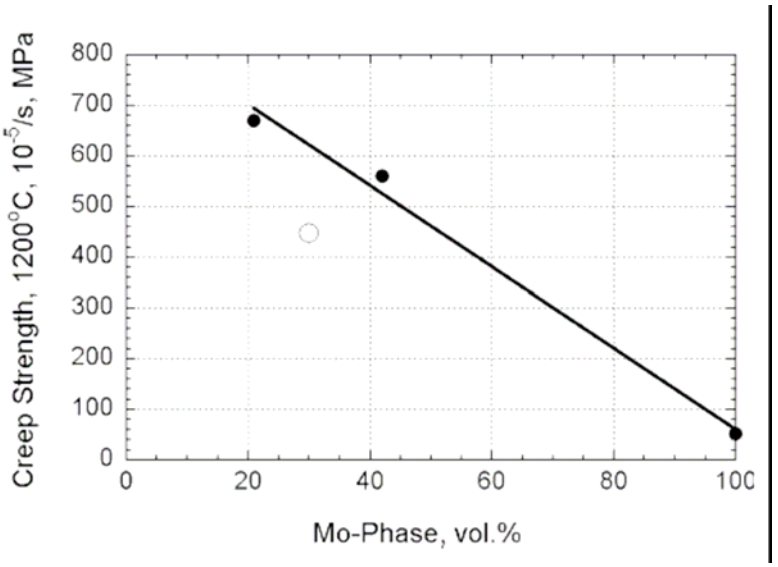

Figure 9 Creep strength of Mo-Si-B alloys at 1200°C as a function of the α-Mo volume fraction. The solid circles correspond to specimens containing individual α -Mo particles, as well as pure Mo; and the open circle to a specimen with a continuous α -Mo matrix**[54]**

It should be pointed out that alloying additions can increase the creep strength significantly. Compression tests showed that partial substitution of Mo with 19.5 at.% Nb increases the creep strength by approximately a factor of 2[54].

1.3.4 Oxidation behavior

The early studies by Meyer et al.[58] focused on the oxidation behavior of Mo_5Si_3 with and without addition of boron. As shown in Fig.10, the addition of as little as 1.2 wt.% boron significantly improved the oxidation resistance of Mo_5Si_3 over a temperature range of 800–1500°C. Common features of oxidation plots for both B-doped and pure Mo_5Si_3 samples include a small mass gain followed by an abrupt mass loss due to evaporation of volatile MoO_3 during initial heating to the test temperature. It has been proposed that the formation of

B_2O_3 and its fluidity at 800ºC enable viscous sintering of the oxide scale to close the pores, which form during the transient oxidation period due to volatilization of MoO_3.

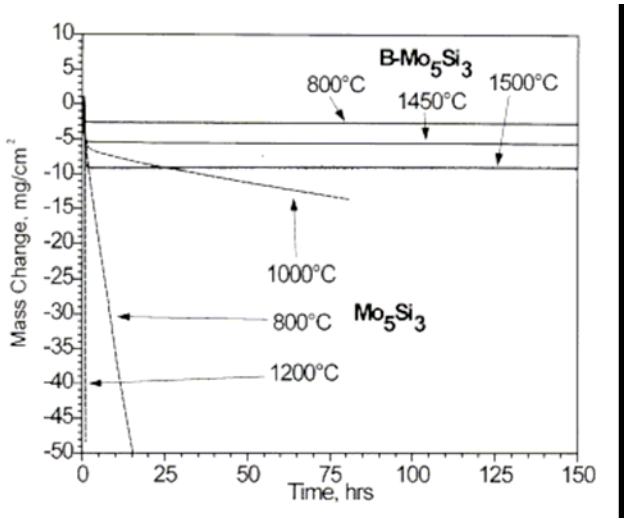

Figure 10 Isothermal oxidation of un-doped Mo_5Si_3 and boron-doped Mo_5Si_3 (Mo-16.1Si–1.2B) between 800 and 1500°C in flowing air

Mo-Si-B composites with T1 as matrix phase also show excellent oxidation resistance in a flowing air atmosphere up to 1600°C and the oxidation rates for Mo-Si-B composites are nearly identical to that of SiC and a Kanthal $MoSi_2$–based heating element sample, as shown in Fig.11, The oxidation behavior of these materials does not change significantly with processing methods (i.e. extruded/sintered, dry pressed/sintered or hot pressed). There appears to be some variation in the activation energy of oxidation ranging from 120 to 400kJ/mol, depending on the sample or processing route. However, these numbers are still within the range of activation energies reported for various silica scale-forming materials such as $MoSi_2$ and Si_3N_4. It is also quite possible that differences in compositions between the sintered and extruded materials could account for the difference in the measured activation energy values.

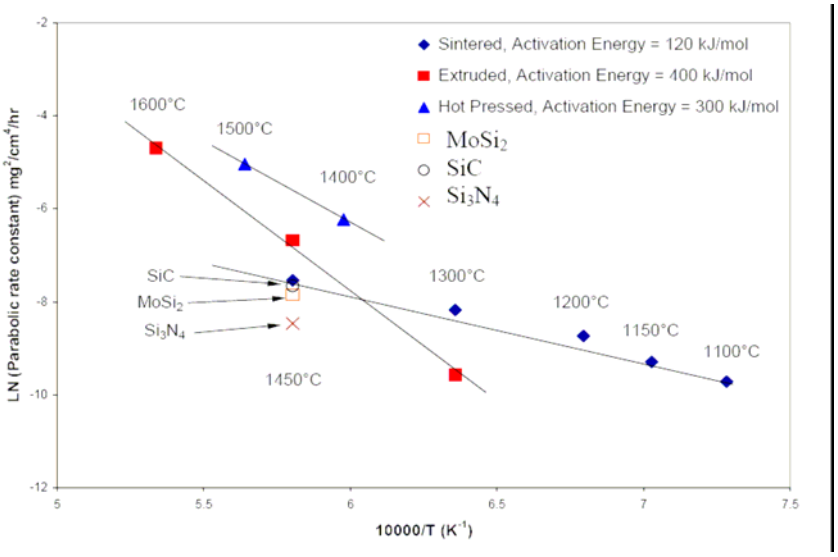

Figure 11 Comparison of the parabolic rate constants for various Mo-Si-B alloys in the T1-$MoSi_2$-MoB phase field

The oxidation behavior of the Mo–Si–B alloys containing α-Mo, Mo_3Si and Mo_5SiB_2 as constituent phases is quite different from that of alloys with T1 phase as matrix. Generally, these alloys offer oxidation resistance superior to that of traditional molybdenum-based alloys in air. A common feature of the oxidation behavior of these alloys is an initial region of rapid mass loss followed by a region of much slower mass change. The initial mass loss is due to the rapid evaporation of Mo as MoO_3. Once a sufficient quantity of MoO_3 has evaporated, the Si and B concentration on the surface becomes high enough to form a protective borosilicate film. Several factors, such as volume fraction of α-Mo and Si/B ratio have great influence on the oxidation resistance.

Schneibel et al.[59] examined oxidation behavior of two sets of Mo-Mo_3Si-Mo_5SiB_2, 25 or 50 Vol. % α-Mo with different Mo_3Si to T2 ratio, respectively. The alloys containing ~50 Vol.% α-Mo (Mo-7Si-12B, Mo-10Si-7B, Mo-12Si-6B were essentially consumed after 1

day at 1200 or 1300ºC in air. However, three alloys (Mo-10Si-18B, Mo-14Si-10B, and Mo-17Si-4B) with about 20 vol. % α-Mo survived and exhibited only modest weight losses. More detailed results about thr effect of volume fraction of α-Mo on the oxidation behavior were shown in Fig.12. As expected, the rate of the mass loss increases as the α-Mo volume fraction increases. There are other factors that can contribute to oxidation rate. For example, Menddiratta et al. [60] studied the effect of variation in Si and B contents (which results in a variation of volume fractions of the three phases) on oxidation kinetics of Mo-Mo_3Si-T2 and showed that a critical combination of both the Si and B levels is required to obtain a small initial weight loss. Supatarawanich *et al*.[61] found that the oxidation resistance at 1300 °C was improved if the Mo_3Si/T2 ratio was increased.

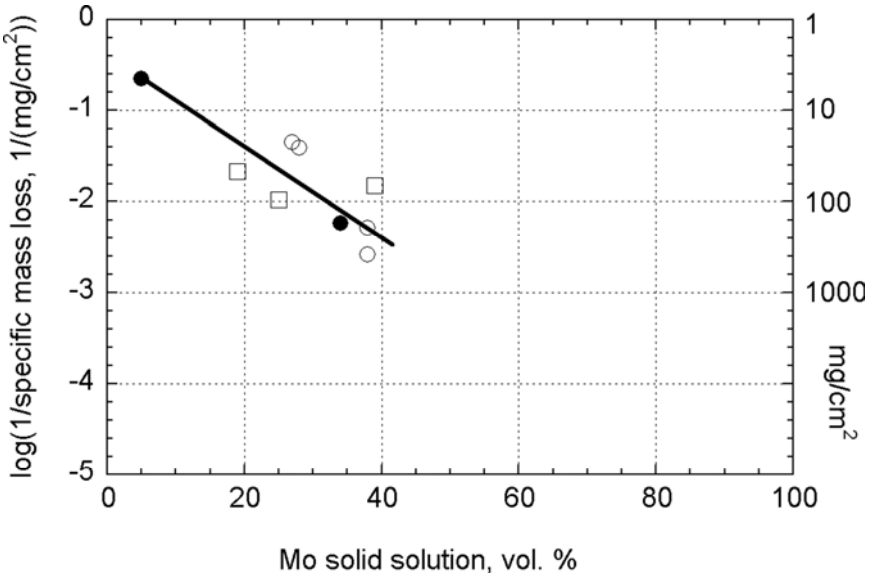

Figure 12 Specific mass loss of Mo-Si-B alloys after oxidation for 20 to 24 h at 1200 °C and 1300 °C in air, as a function of α-Mo volume fraction. The solid circles represent specimens containing individual α-Mo particles, tested at 1200 °C; the open circles represent specimens with a continuous α-Mo matrix tested at 1200 °C; and the squares correspond to cast specimens tested at 1300 °C

In summary, α-Mo based Mo-Si-B composites offer oxidation resistance superior to that of traditional molybdenum-based alloy, however, the oxidation resistance may be insufficient at temperatures above 1300ºC for structural applications. Improvements in the oxidation resistance depend on the development of coating systems or new oxidation-resistant alloys.

Summary

Nickel-based superalloy materials, currently employed in the production of aircraft and power generation turbine engines, have reached their maximum temperature with operating temperatures greater than 85% of their melting temperatures and will not be able to meet the temperatures requirements of advance turbine engines. Over the past decades, many intermetallics alloy systems have been screened for potential use above 800ºC. Of these systems, γ-TiAl is to be close to application, and several gas turbine engine component with TiAl alloys have been tested. γ -TiAl turbochargers wheel is being produced the in commercial quantities by Mitsubishi Ltd. and has been installed in the 2.5 liter engine of their latest models. The service temperature capability for γ-TiAl is less than 750ºC, and prospects for higher temperature applications are very limited. Transition-metal silicide such as Ti_5Si_3, Mo-Si-B in situ composites, and Nb-based refractory intermetallics with significant increases in temperature capability is viable for service at temperatures beyond that of nickel-based superalloys. If these systems are to be employed, a balance of properties, such as low-temperature damage tolerance, high-temperature strength and creep resistance, and superior oxidation resistance, are required. Unfortunately while Mo-based Mo-Si-B *in situ* composites exhibit an excellent combination of mechanical properties, their oxidation resistance is insufficient for elevated temperature application. For Ti_5Si_3-based alloys, the previous studies

on high-temperature oxidation behavior have showed a significant scattering, the intrinsic oxidation mechanism still remains unclear.

This study included three parts: first, investigate the effect of alloy composition, atmosphere, and addition of alloying elements on the oxidation of Ti_5Si_3, and clarify the discrepancies in the published oxidation resistance of Ti_5Si_3; second, exploiting to protect the mechanically promising Mo-Mo_3Si-T2 *in situ* composites from oxidation at elevated temperatures; Finally, reevaluate the Nb-B binary phase diagram in the vicinity of Nb_3B_2 composition.

References

[1] T. M. Pollock, S. Tin, Journal of Propulsion and Power 22 (2006) 361-374.

[2] B. Gleeson, Journal of Propulsion and Power 22 (2006) 375-383.

[3] J. R. Davis, Editor, ASM Specialty Handbook: Heat-Resistant Materials, 1997, p. 500.

[4] S. J. Balsone, B. P. Bewlay, M. R. Jackson, P. R. Subramanian, J. C. Zhao, A. Chatterjee, T. M. Heffernan, Structural Intermetallics 2001, Proceedings of the International Symposium on Structural Intermetallics, 3rd, Jackson Hole, WY, United States, Sept. 23-27, 2001 (2001) 99-108.

[5] C. T. Liu, E. P. George, International Symposium on Nickel and Iron Aluminides: Processing, Properties, and Applications, Proceedings from Materials Week'96, Cincinnati, Oct. 7-9, 1996 (1997) 21-32.

[6] E. P. George, C. T. Liu, D. P. Pope, Acta Materialia 44 (1996) 1757-1763.

[7] V. K. Sikka, S. C. Deevi, S. Viswanathan, R. W. Swindeman, M. L. Santella, Intermetallics 8 (2000) 1329-1337.

[8] V. K. Sikka, Materials Research Society Symposium Proceedings 460 (1997) 15-27.

[9] N. S. Stoloff, C. T. Liu, S. C. Deevi, Intermetallics 8 (2000) 1313-1320.

[10] R. Darolia, W. S. Walston, M. V. Nathal, Superalloys 1996, Proceedings of the International Symposium on Superalloys, 8th, Champion, Pa., Sept. 22-26, 1996 (1996) 561-570.

[11] V. I. Levit, M. J. Kaufman, Structural Intermetallics 1997, Proceedings of the International Symposium on Structural Intermetallics, 2nd, Champion, Pa., Sept. 21-25, 1997 (1997) 683-690.

[12] Y.-W. Kim, Interstitial and Substitutional Solute Effects in Intermetallics, Proceedings of the International Symposium, 2nd, Rosemont, Ill., Oct. 11-15, 1998 (1998) 189-200.

[13] S. Tsuyama, S. Mitao, K. Minakawa, Microstruct./Prop. Relat. Titanium Aluminides Alloys, Proc. Seven Sess. Symp. (1991) 213-226.

[14] Y.-W. Kim, D. M. Dimiduk, Process., Prop. Appl. Met. Ceram. Mater., Proc. Int. Conf. 2 (1992) 589-600.

[15] Y.-W. Kim, Jom 46 (1994) 30-39.

[16] Y.-W. Kim, D. M. Dimiduk, Structural Intermetallics 1997, Proceedings of the International Symposium on Structural Intermetallics, 2nd, Champion, Pa., Sept. 21-25, 1997 (1997) 531-543.

[17] H. Kestler, H. Clemens, Titanium and Titanium Alloys (2003) 351-392.

[18] W. Smarsly, H. Baur, G. Glitz, H. Clemens, T. Khan, M. Thomas, Structural Intermetallics 2001, Proceedings of the International Symposium on Structural Intermetallics, 3rd, Jackson Hole, WY, United States, Sept. 23-27, 2001 (2001) 25-34.

[19] R. Mitra, V. V. Rama Rao, Metallurgical and Materials Transactions A: Physical Metallurgy and Materials Science 29A (1998) 1665-1675.

[20] G. Frommeyer, R. Rosenkranz, C. Luedecke, Zeitschrift fuer Metallkunde 81 (1990) 307-313.

[21] J. J. Williams, Y. Y. Ye, M. J. Kramer, K. M. Ho, L. Hong, C. L. Fu, S. K. Malik, Intermetallics 8 (2000) 937-943.

[22] J. I. Goldstein, S. K. Choi, F. J. J. Van Loo, G. F. Bastin, R. Metselaar, Journal of the American Ceramic Society 78 (1995) 313-322.

[23] W. Wakelkamp, Diffusion and Phase Relationship in the SystemsTi-Si-C and Ti-Si-N, in: '(Ed.)'^'(Eds.)', vol Eindhoven University of Technology, Eindhoven, 1991, p.^pp.

[24] A. J. Thom, V. G. Young, M. Akinc, Journal of Alloys and Compounds 296 (2000) 59-66.

[25] J. D. Corbert, E. Garcia, A. M. Guloy, Chemical Materials 10 (1998) 2824-2836.

[26] R. Radhakrishnan, J. Williams, M. Kramer, M. Akinc, Ceramic Engineering and Science Proceedings 19 (1998) 381-388.

[27] A. J. Thom, M. Akinc, Ceramic Engineering and Science Proceedings 18 (1997) 57-65.

[28] J. J. Williams, M. J. Kramer, M. Akinc, Journal of Materials Research 15 (2000) 1780-1785.

[29] Y. Ikarashi, K. Ishizaki, T. Nagai, Y. Hasghizuka, Intermetallics 4 (1996) 141-145.

[30] A. J. Thom, M. Akinc, O. B. Cavin, C. R. Hubbard, Journal of Materials Science letters 13 (1994) 1657-1660.

[31] T. Nakashima, Y. Umakoshi, Philosophical Magazine Letters 66 (1992) 317-321.

[32] R. Rosenkranz, G. Frommeyer, W. Smarsly, Materials Science & Engineering, A: Structural Materials: Properties, Microstructure and Processing A152 (1992) 288-294.

[33] G. Frommeyer, R. Rosenkranz, C. Luedecke, Zeitschrift fuer Metallkunde 81 (1990) 307-313.

[34] R. Mitra, Metallurgical and Materials Transactions A: Physical Metallurgy and Materials Science 29A (1998) 1629-1641.

[35] A. J. Thom, Y. Kim, M. Akinc, Materials Research Society Symposium Proceedings 288 (1993) 1037-1042.

[36] A. J. Thom, M. K. Meyer, J. J. Williams, M. Akinc, Processing and Fabrication of Advanced Materials IV, Proceedings of a Symposium, 4th, Cleveland, Oct. 29-Nov. 2, 1995 (1996) 139-149.

[37] Y. Kim, A. J. Thom, M. Akinc, Process. Fabr. Adv. Mater. High Temp. Appl.--II, Proc. Symp. Mater Week '92 (1993) 189-208.

[38] A. Abba, A. Galerie, M. Caillet, Oxidation of Metals 17 (1982) 43-54.

[39] S. Taniguchi, T. Minamida, T. Shibata, Materials Science Forum 251-254 (1997) 227-234.

[40] J. J. Williams, M. Akinc, Oxidation of Metals 58 (2002) 57-71.

[41] A. J. Thom, M. Akinc, Advanced Ceramics for Structural and Tribological Applications, Proceedings of the International Symposium on Advanced Ceramics for Structural and Tribological Applications, Vancouver, B. C., Aug. 20-24, 1995 (1995) 619-627.

[42] D. M. Dimiduk, J. H. Perepezko, MRS Bulletin 28 (2003) 639-645.

[43] H. Nowotny, B. Lux, H. Kudielka, Monatshefte fuer Chemie 87 (1956) 447-470.

[44] J. J. Huebsch, M. J. Kramer, H. L. Zhao, M. Akinc, Intermetallics 8 (2000) 143-150.

[45] M. Akinc, M. K. Meyer, M. J. Kramer, A. J. Thom, J. J. Huebsch, B. Cook, Boron-doped molybdenum silicides for structural applications, in: '(Ed.)'^'(Eds.)', Materials Science

& Engineering, A: Structural Materials: Properties, Microstructure and Processing, vol A261, 1999, p.^pp. 16-23.

[46] D. M. Berczik, Molybdenum alloys with silicon and boron for oxidation resistance, in: '(Ed.)'^'(Eds.)', vol (United Technologies Corp., USA). Application: US US, 1997, p.^pp. 6 pp , Cont -in-part of U S Ser No 170,933, abandoned.

[47] K. Ito, M. Kumagai, T. Hayashi, M. Yamaguchi, Room temperature fracture toughness and high temperature strength of T2/Moss and (Mo,Nb)ss/T1/T2 eutectic alloys in the Mo-Si-B system, in: '(Ed.)'^'(Eds.)', Scripta Materialia, vol 49, 2003, p.^pp. 285-290.

[48] R. Sakidja, J. Myers, S. Kim, J. H. Perepezko, International Journal of Refractory Metals & Hard Materials 18 (2001) 193-204.

[49] J. J. Kruzic, J. H. Schneibel, R. O. Ritchie, Materials Research Society Symposium Proceedings 842 (2005) 303-308.

[50] J. J. Kruzic, J. H. Schneibel, R. O. Ritchie, Metallurgical and Materials Transactions A: Physical Metallurgy and Materials Science 36A (2005) 2393-2402.

[51] J. J. Kruzic, J. H. Schneibel, R. O. Ritchie, Scripta Materialia 50 (2003) 459-464.

[52] J. H. Schneibel, R. O. Ritchie, J. J. Kruzic, P. F. Tortorelli, Metallurgical and Materials Transactions A: Physical Metallurgy and Materials Science 36A (2005) 525-531.

[53] T. G. Nieh, J. G. Wang, C. T. Liu, Intermetallics 9 (2001) 73-79.

[54] J. H. Schneibel, Intermetallics 11 (2003) 625-632.

[55] P. Jehanno, M. Heilmaier, H. Kestler, Intermetallics 12 (2004) 1005-1009.

[56] P. Jehanno, M. Heilmaier, H. Kestler, M. Boening, A. Venskutonis, B. Bewlay, M. Jackson, Metallurgical and Materials Transactions A: Physical Metallurgy and Materials Science 36A (2005) 515-523.

[57] M. K. Meyer, M. J. Kramer, M. Akinca, Intermetallics 4 (1996) 273-281.

[58] M. K. Meyer, M. Akinc, Journal of the American Ceramic Society 79 (1996) 2763-2766.

[59] J. H. Schneibel, J. A. Sekhar, Materials Science & Engineering, A: Structural Materials: Properties, Microstructure and Processing A340 (2003) 204-211.

[60] M. G. Mendiratta, T. A. Parthasarathy, D. M. Dimiduk, Intermetallics 10 (2002) 225-232.

[61] V. Supatarawanich, D. R. Johnson, C. T. Liu, Intermetallics 12 (2004) 721-725.

Chapter 2. Role of Nitrogen on the Oxidative Stability of Ti_5Si_3 Based Alloys at Elevated Temperature

Zhihong Tang, Andrew J. Thom and Mufit Akinc

A paper published in *Intermetallics* in 2006

Abstract

Ti_5Si_3 has been extensively studied as a candidate material for high temperature application due to its high melting point (2130°C), low density (~4.3 g/cm^3) and excellent oxidation resistance in oxygen above 1000°C. However, stoichiometric Ti_5Si_3 alloy experiences accelerated oxidation during exposure in air above 1000°C. It was proposed that nitrogen was responsible for the increased oxidation in air. In the present study, the isothermal reaction kinetics of Ti_5Si_3 in nitrogen at 1000°C was investigated. Compared to a slow parabolic oxidation rate in oxygen, a faster linear reaction rate was observed when Ti_5Si_3 is exposed to nitrogen. Further studies on the oxidation behavior of for changing nitrogen/oxygen atmospheres showed that Ti_5Si_3 is stable for exposure up to 400 hours at 1000°C when the gas contained 50% N_2. Breakaway oxidation occurs after short exposures when the gas contained at least 75% N_2, and the reaction rate increased as the concentration of N_2 increased. Furthermore time to breakaway oxidation decreases with the increasing nitrogen partial pressure. Extensive analysis of the oxidation products with SEM and XRD revealed that the formation and fast growth of a nitride-containing subscale interferes with the establishment of the continuous protective silica scale and contributes to the breakaway oxidation.

Keywords: A. titanium silicides; B. Oxidation, diffusion; F. Corrosion behavior; G. aerospace constructional use

Introduction

Ti_5Si_3 possesses many attractive properties such as high melting point (~2130°C), low density (~4.3 g/cm^3), good creep and oxidation resistance below 850°C as a candidate material for high temperature application [1-6]. However, Ti_5Si_3 shows an insufficient air oxidation resistance at and above 1000°C. Nitrogen is thought to have a critical role on the oxidation of Ti_5Si_3. Several studies by Thom *et al*. [7-10] Kim *et al.*[11] and Abba *et al.*[12] have reported that Ti_5Si_3 experiences breakaway oxidation after a certain time with exposure to air at and above 1000°C while possessing excellent oxidation resistance in oxygen. Williams *et al*.[13] compared the oxide scale composition and structure before and after breakaway oxidation, They attributed the breakaway oxidation to the formation and growth of subscale phases such as TiN and $TiSi_2$, which causes a large volume expansion and disrupts the external oxide scale. But this hypothesis needs further evidence.

Some work has shown that the oxidation resistance of Ti_5Si_3 can be improved using alloying addition. Mitra and Rao[14] and Taniguichi *et al*.[15] have reported that non-stoichiometric Ti_5Si_3 with about 5% silicon-rich phase shows excellent oxidation resistance in air up to 1250°C. Thom *et al*.[16,17] and Williams *et al*.[13] reported alloying additions of boron and carbon can greatly reduce the oxidation rate in air by several orders of magnitude. It seems that oxidation resistance improvement for these alloys is linked with absence of nitride subscale formation.

For other Ti-based intermetallics, nitride formation is typically observed in the presence of nitrogen, which complicates the oxidation behavior of these compounds in N_2-containing atmosphere. For example, for TiAl alloys, TiN formation during the initial stages of oxidation in air has been linked with disruption of Al_2O_3 continuity and the inability of these alloys to establish a protective Al_2O_3 scale in air where continuous Al_2O_3 formation is observed in pure oxygen [18,19]. For $TiSi_2$, though excellent oxidation resistance is observed in both air and pure O_2, the structures of oxide scale are totally different. In air a two-layer scale grows between about 1000°C and 1200°C with an inward growing fine-grain mixture of SiO_2 + TiO_2 and an outer outward-growing TiO_2 discontinuous layer. In contrast a scale of a SiO_2 matrix with some Ti oxide precipitates is formed in pure oxygen or Ar-O_2. TiN formation in the transient oxidation is thought to be responsible for the inner mixed partial layer in air[20]. For Ti_3Al that is incapable of forming a protective Al_2O_3 layer even in pure oxygen, oxidation rates are generally reported to be slower in air than in oxygen, due to the formation of a continuous subscale TiN layer, which limits subsequent oxygen dissolution into the alloy and can effectively enrich the alloy locally in Al, relative to Ti[21,22].

The present work examines the nitridation behavior of Ti_5Si_3 in nitrogen and in various nitrogen/oxygen gas mixtures in order to clearly understand the relevant oxidation mechanism of Ti_5Si_3 in the presence of nitrogen.

Experimental procedures

Starting materials include sponge titanium (Timet, 99.7 wt.%) and silicon pieces (Alfa AEsar, 99.9999 wt.%). The sponge titanium was pre-melted twice to volatilize surface contamination before being used in synthesis. Sample compositions, which weighed approximately 10 g each, were synthesized via arc melting in an ultra-high purity (UHP)

argon atmosphere. Weight losses after arc melting were generally much less than 0.5 wt%. Based on x-ray diffraction measurements and lattice parameter determininations by refinement of the diffraction patterns, samples were well crystallized, homogeneous and interstitially pure. Arc-melting ingots were crushed to granule materials and then sieved to 600 μm. Based on SEM observation; these granules appear to be crack-free although some pores inside the alloy (Fig.13). All oxidation experiments were run on these arc-melted granule materials

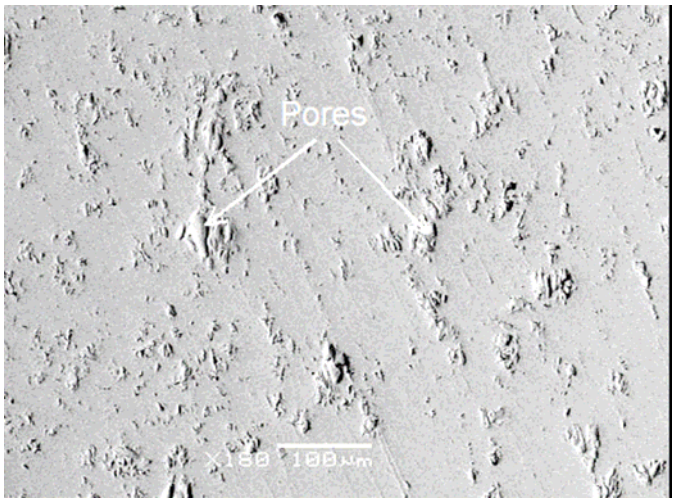

Figure 13 The microstructure (secondary electron image, SE) of cross section of as-prepared Ti_5Si_3 granule. No macrocracking is evident and only a small amount of closed pores were observed in these granules

In the analysis of oxidation data, it is customary to normalize the mass gain to the sample's initial surface area in order to compare the reaction rates at which samples oxidize. Thus the specific surface area of these granule materials must be measured. The specific surface area of the granules was measured using adsorption isotherms and applying the BET method to determine the surface area. Krypton rather than nitrogen was used as the adsorbate

gas at liquid nitrogen temperature (≈77K) because of the low surface area of the samples. The detection limit of the instrument using krypton is 5×10^{-4} m^2/g. The instrument was calibrated using both high (182 m^2/g) and low (2.09 m^2/g) alumina surface area standards, although the measured specific surface area of the samples was much closer to the lower standard. The average specific surface area of Ti_5Si_3 sample based on five measurements, was determined to be 0.023 ±0.002 m^2/g.

All isothermal oxidation and nitridation experiments were conducted on the granules using a thermogravimetric analyser (TGA). The TGA instrument, which is specially designed to accurately control the reaction. Each TGA sample, which weighed approximately 80 mg and had a surface area of about 18 cm^2, was placed in a quartz sample pan and suspended from a Cahn 2000 microbalance. The TGA apparatus was then evacuated to 60 mtorr and subsequently backfilled with argon. The evacuation-back filling sequence was repeated four times to purge the ambient air in the TGA system. The test atmosphere was then allowed to flow at 50 cm^3/min, and the sample was heated to 1000°C at a rate of 20°C/min and held for 25 to 400 hours. Gas flow was maintained at 50 cm^3/min throughout the experiment. The reaction atmospheres included pure oxygen, pure nitrogen, and the mixture of the two with preset ratios. Gas mixtures were precisely regulated using mass flow controller, which controlled the flow rate of each gas component and has a minimum detect limit of 0.2 cm^3/min. The quantitative measurements on the rate of oxidation were made for sample with protective behavior assuming that the surface area did not change too much over time. This assumption is reasonable considering the several micron thick oxide scale on the granule materials with a particle size of about 600μm However, quantitative measurements on the rate of oxidative can not be made for sample with poor oxidation resistance because the

reaction surface area becomes significantly reduced in a non-uniform manner over the course of the experiment.

The use of granular arc-melted materials in the TGA provided crack-free materials (a major problem for this alloy), good control over starting surface areas and large surface-to-volume ratio, which make analysis and characterization of oxidation more accurate. More important, the use of are-melted materials insured high purity sample in order to study the intrinsic oxidation and nitridation behavior of stoichiometric Ti_5Si_3 because it has a high affinity of such elements as C, N, O and these interstitial elements had a significant effect on the oxidation of Ti_5Si_3[13].

After the granular samples were oxidized in the TGA apparatus, they were ground to ≤ 20 μm for phase analysis using X-ray diffraction (XRD). An α-Al_2O_3 standard (NIST SRM676) was added to most samples for accurate lattice parameter refinement. Cross-sections of these oxide scales were then analyzed using scanning electron microscopy (SEM). The phases determined from XRD were correlated to the scale morphologies observed in the scanning electron microscope (SEM) and energy dispersive spectrometer (EDS).

Results

Nitridation behavior

The measured oxidation behavior of granular stoichimertic Ti_5Si_3 in air and pure O_2 at 1000°C agrees well with the studies of Abba et al.[12], Thom et al.[17,23-25] and Willams et al.[13]. As shown in Fig.14, steady state oxidation kinetics was only observed in pure O_2. However, Ti_5Si_3 was only stable up to 12 hours in air, after which accelerated oxidation was observed.

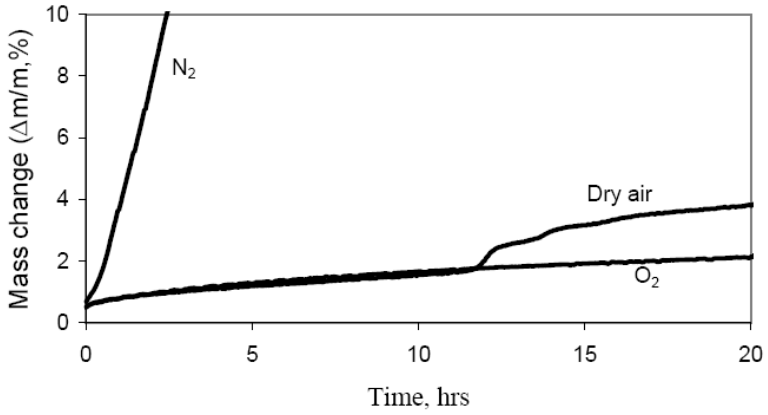

Figure 14 Relative mass changes for Ti_5Si_3 granules in nitrogen, oxygen and air at 1000°C

Fig.14 also shows the high reactivity of Ti_5Si_3 when exposed to pure nitrogen at 1000°C. Compared to the slow parabolic oxidation rate in oxygen, Ti_5Si_3 shows very fast linear reaction rate in nitrogen. Though it is difficult to calculate the reaction rate directly from the TGA curve since the surface area of sample changes significantly with time, a rough estimate can be made if one assumed that the surface area of sample remains constant with time in the very early stage. The calculated linear rate constant is about 0.17 $mg/cm^2/hr$. From X-ray diffraction pattern as shown in Fig.15, almost no any Ti_5Si_3 phase can be detected after exposure to nitrogen for 18 hours, suggesting that almost all Ti_5Si_3 is consumed. The main nitridation products are TiN, $TiSi_2$ and Si phases (Al_2O_3 is added for the standard material here). A small amount of TiO_2 phases is also found in the reaction products. It is not surprising that rutile is formed in nitrogen atmosphere because of the extremely low equilibriium partial pressure of oxygen for rutile formation (~10^{-27} atm.). Such a low level of oxygen partial pressure can not be achieved without using an equilibrium H_2/H_2O or CO/CO_2 atmosphere. According to the x-ray diffraction pattern of the scale, the nitridation reaction in equation 1 and 2 may be proposed:

$$Ti_5Si_3 + \frac{7}{4}N_2 \rightarrow \frac{7}{2}TiN + \frac{3}{2}TiSi_2 \qquad (1)$$

$$Ti_5Si_3 + \frac{5}{2}N_2 \rightarrow 5TiN + 3Si \qquad (2)$$

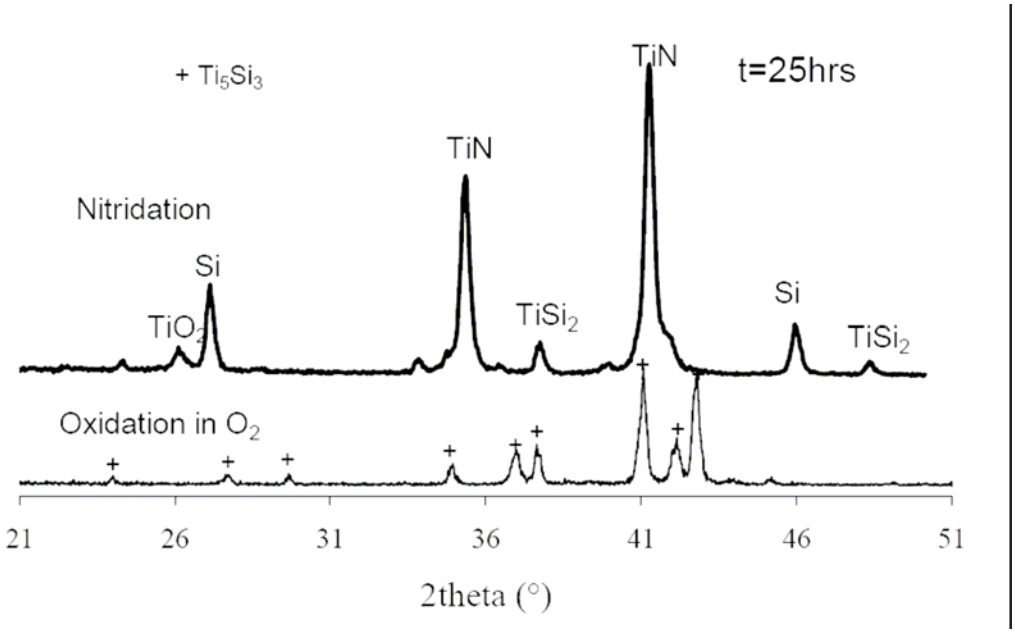

Figure 15 X-ray diffraction patterns of Ti_5Si_3 sample exposed to nitrogen and oxygen for 25 hours at 1000°C. Al_2O_3 (NIST SRM676) was used as a standard material

Fig.16 shows the microstructure of cross-section after 18 hours nitridation and compared against as prepared alloy (Fig.13), the initial coarse granule sample has fractured into small pieces. Cracks were observed at the interface between the oxide scale and nitride layer. Although the mismatch of coefficient of thermal expansion (CTE) between reaction products and silicide may cause cracking and lead to fast reaction rate during cooling, other effects other than CTE mismatch during cooling play a critical role since the oxide scale with tens of micron thickness was observed on cracking surface (Fig.16b). Although the formation and growth of subscale phases according to equation 1 and 2 causes relatively small volume

change. As shown in Table 3, a combination of the first two reactions to generate the reaction products of $TiSi_2$, TiN and Si would produce a volumetric expansion of between 5 and 24% (equation 1 predicts an 11% volume increase). Although the exact reason for the fracture is not known, it is clear that the nitridation process leads to a catastrophic, pest-like degradation of the sample.

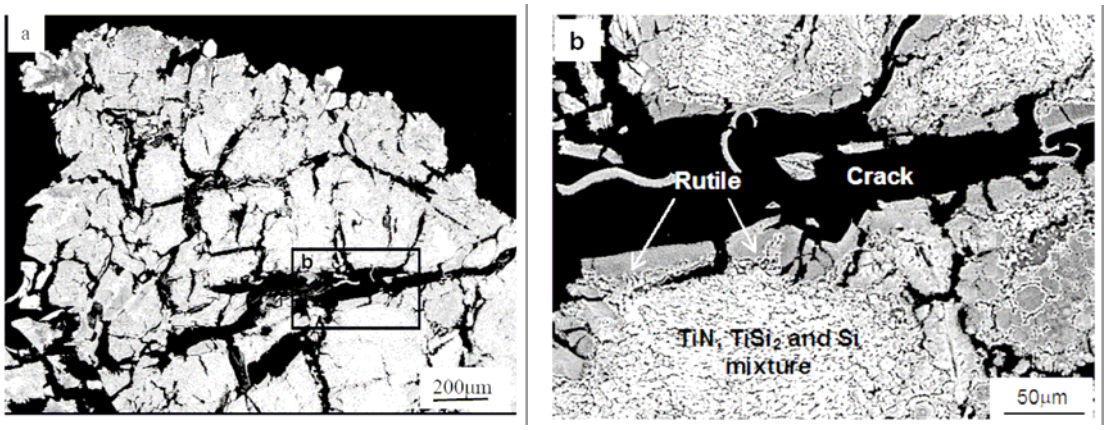

Figure 16 The cross-sectional microstructure (BSE) of: (a) Ti_5Si_3 granules after 18 hours of nitridation at 1000°C (Δm/m~26%), (b) higher magnification

Table 3 Volume change due to the formation of nitride subscale and later oxidation

Reaction	Volume change
$Ti_5Si_3+7/4N_2=3/2TiSi_2+7/2TiN$	1.05
$Ti_5Si_3+5/2N_2=3Si+5TiN$	1.24
$TiN+O_2=TiO_2+1/2N_2$	1.66
$TiSi_2+3O_2=TiO_2+2SiO_2$	2.83
$Si+O_2=SiO_2$	2.27

Note: Volume change was calculated from published densities of the reactants and products.

Oxidation behavior in the mixed N_2/O_2 atmospheres

Both the previous studies[13,26] and the present study showed that Ti_5Si_3 possess excellent oxidation resistance in pure O_2 but that accelerated oxidation occurs in air. Thus it is clear that nitrogen plays an important role in the oxidation behavior of Ti_5Si_3. The effect of changing N_2/O_2 atmosphere on oxidation behavior of Ti_5Si_3 was investigated at 1000°C. The results are shown in Fig.17. At lower nitrogen/oxygen atmospheres with addition of nitrogen less than 50%, steady-state parabolic oxidation behavior was observed up to 400 hrs, and the parabolic oxidation rate constant is about 3×10^{-4} $mg^2/(cm^4\cdot hr)$, which is comparable to the rate of Si oxidation in dry oxygen (2×10^{-4} $mg^2/cm^4/hr$)[27]. It implies that a continuous protective silica layer was established.

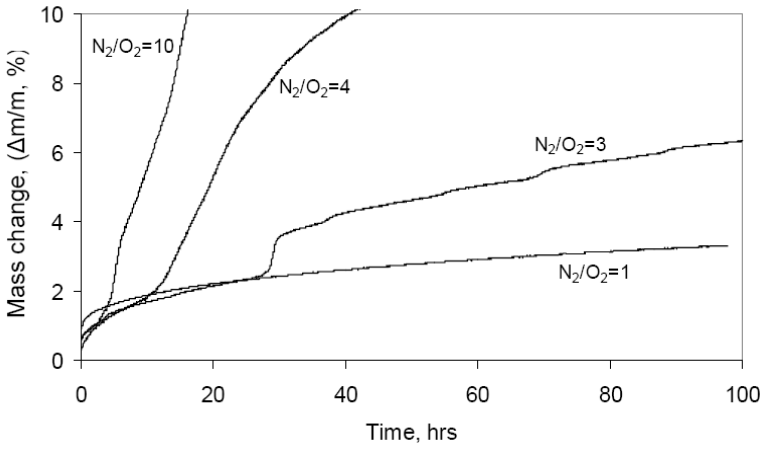

Figure 17 Relative mass changes (*Δm/m*) of Ti_5Si_3 granules with time in various N_2/O_2 atmospheres at 1000°C

At higher nitrogen/oxygen atmospheres with the addition of nitrogen more than 75%, breakaway degradation occurs with the time to breakaway decreasing as the nitrogen/oxygen ratio increases. Breakaway degradation occurs after about 28 hrs for $N_2/O_2 = 3$, while the time to breakaway decreasing to 12 and 3 hours for $N_2/O_2 = 4$ and 10, respectively.

Fig.18 shows the XRD pattern of Ti_5Si_3 after 25 hours exposure to different N_2/O_2 atmospheres. For pure O_2 and N_2/O_2 =1, very little reaction product was detected with the patterns dominated by Ti_5Si_3 peaks. Although the Si, $TiSi_2$ and TiN phases were observed in SEM, it is difficult to identify these phases for up to N_2/O_2=4 in the XRD pattern as their fraction is well below the detection limit. For N_2/O_2 = 10, TiO_2, Si, $TiSi_2$ and TiN phases were identified, and this is consistent with the nitridation products of sample exposed to pure nitrogen. However, the addition of 10% oxygen has clearly retarded the nitridation reaction since unreacted Ti_5Si_3 alloy is still present after 25 hours exposure.

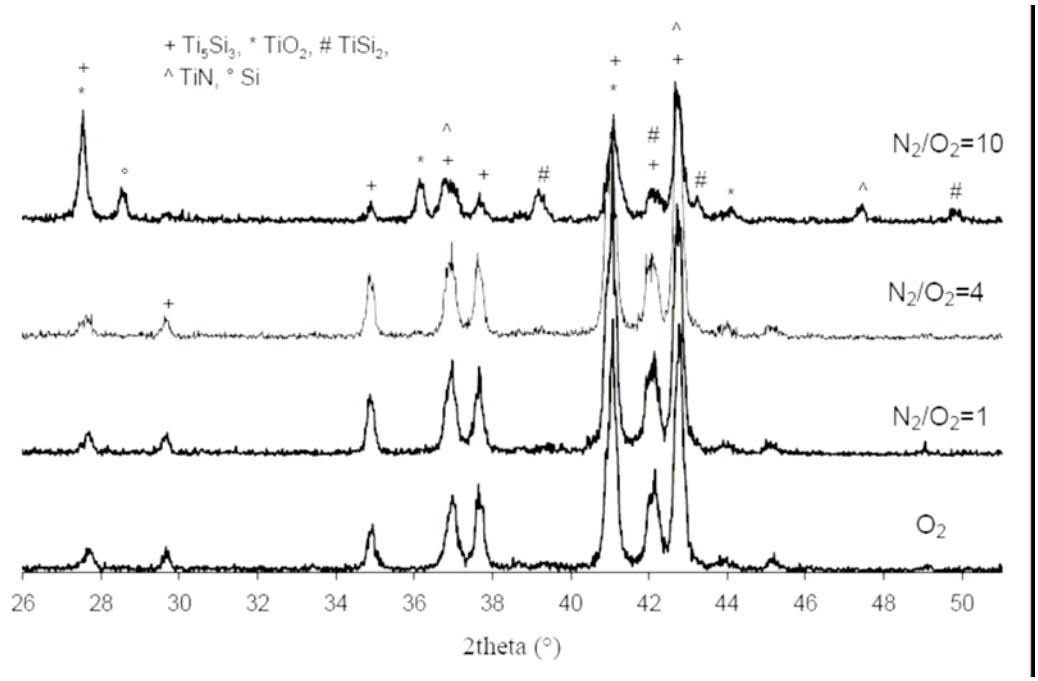

Figure 18 X-ray patterns of Ti_5Si_3 granules exposed to various N_2/O_2 atmospheres for 25 hours at 1000°C

The microstructural observations of oxide scale are consistent with the XRD results. As shown in Fig.19a, a 4 μm thick continuous inner silica layer with even thinner outer rutile layer was observed after exposure to a gas mixture with N_2/O_2=1 for 100 hours at 1000ºC. No nitride phase could be resolved by BSE imaging. For the sample oxidized in N_2/O_2=10

atmosphere about 100 μm nitride subscale layers were developed after 10 hours exposure and the initial protective oxide scale was disrupted (Fig.19b). Large cracks were observed between the oxide layer and nitride subscale.

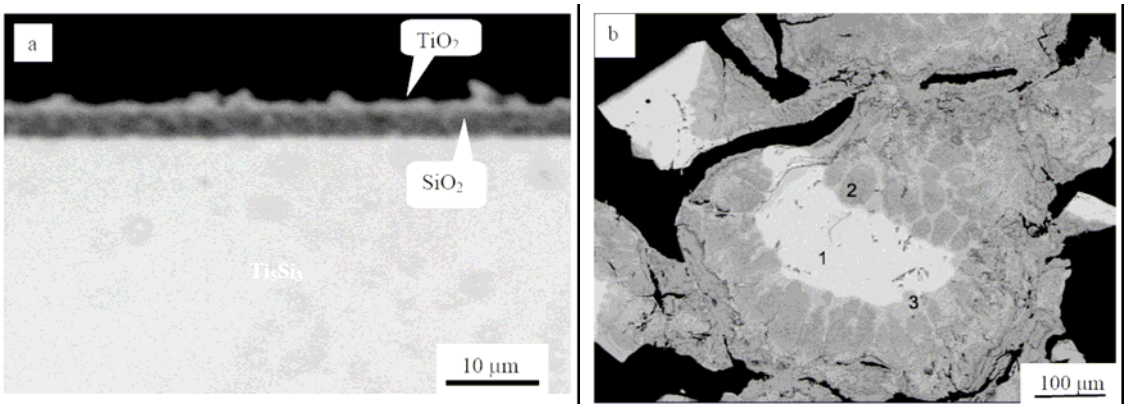

Figure 19 The cross-section of Ti_5Si_3 after exposure at 1000°C to (a) N_2/O_2=1 for 100 hours (mass change, Δm/m~3.3%), (b) N_2/O_2=10 for 10 hours (mass change, Δm/m~7%). 1: Ti_5Si_3; 2: titanium nitride and mixed oxides; 3: $TiSi_2$

For samples that experience breakaway, the mass gain curve may be shifted to coincide at the origin as the breakaway begins. As shown in Fig.20, the initial reaction rates of Ti_5Si_3 are similar to the reaction rate in pure N_2. This suggests that the accelerated oxidation rate after a certain time in a gas mixture with $N_2/O_2 \geq 3$ may result from the nucleation and rapid growth of TiN, Si and $TiSi_2$ subscale phases due to internal nitridation.

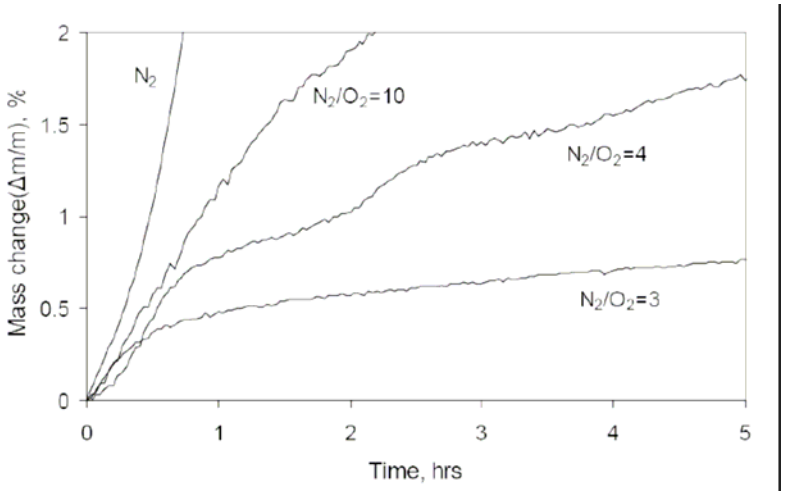

Figure 20 Relative mass changes with time for samples showing accelerated degradation. Onset of the accelerated degradation in Fig.17 was taken as the origin for these plots

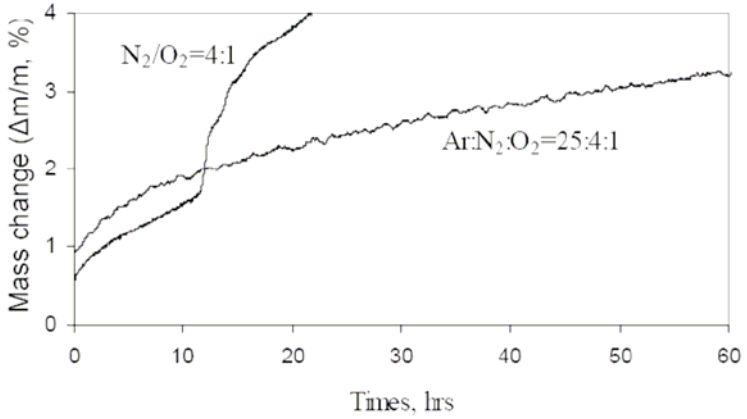

Figure 21 Oxidation behavior of Ti_5Si_3 in $Ar:N_2:O_2 = 25:4:1$ compared to $N_2:O_2 = 4:1$ atmosphere at 1000°C

Fig.21 shows the oxidation behavior of Ti_5Si_3 in a gas mixture with $Ar/N_2/O_2 =$ 25:4:1, which maintains the same nitrogen to oxygen ratio as air, but reduces the partial pressure of nitrogen by five folds. Parabolic kinetics was observed with a parabolic rate constant of 3×10^{-4} $mg^2/cm^4/hr$, which is similar with that of samples in $N_2/O_2\leq1$. Also shown in the Fig.21 is the oxidation behavior in $N_2/O_2=4$ for comparison. Though the initial behaviors are similar, accelerated oxidation occurred in the latter after 12 hours. This

observation suggests that the critical factor is the partial pressure of nitrogen in the atmosphere, not the ratio of N_2 to O_2 in the mixture.

Growth of subscale layer underneath the oxide layer

In order to study the growth characteristics of the subscale layer, Ti_5Si_3 was pre-oxidized in pure O_2, and then exposed to N_2 or gas mixture of N_2 and O_2. After pre-oxidizing in pure O_2, a thin protective silica layer was formed as studied before. But when the pre-oxidized samples were subsequently exposed to nitrogen, as shown in Fig.22, they reacted very rapidly. Even the extended pre-oxidation of 50 hours is not effective in reducing the nitridation rate. This indicates that the external silica and rutile layer formed during pre-oxidation is not an effective barrier for nitrogen, and furthermore, the diffusion rate of nitrogen through the external scale is much faster than that of oxygen through the external scale.

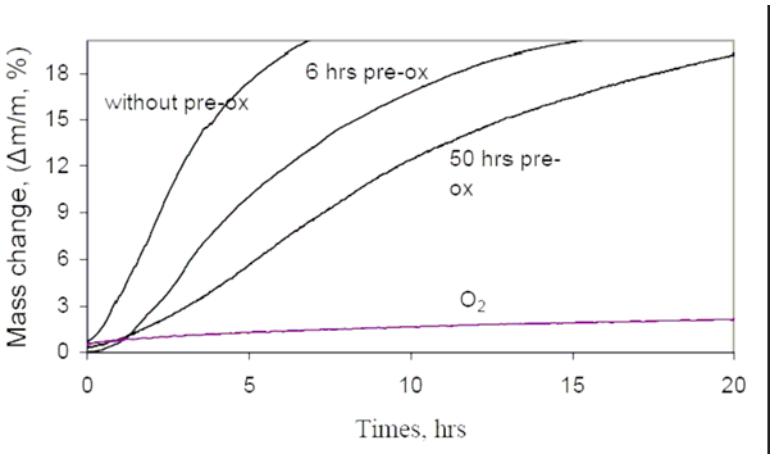

Figure 22 Effect of pre-oxidation in pure O_2 on the rate of nitridation (reaction in nitrogen and oxygen are also included for comparison purposes)

Fig.23 shows the microstructure of Ti_5Si_3 after pre-oxidation followed by nitrdation. A thin protective oxide scale formed when Ti_5Si_3 is pre-oxidized in pure oxygen. After 6

hours exposure to nitrogen, from outside to inside, a 100 μm thick nitride subscale consisting of an mixed layer of TiO_2, SiO_2, TiN and Si, an intermediate TiN layer and an inter $TiSi_2$ layer, is formed beneath the initial oxide scale. Cracks are observed and the initial protective oxide scale was disrupted.

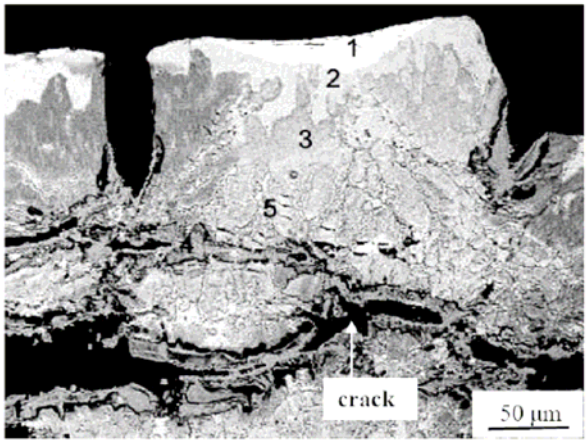

Figure 23 The microstructure of Ti_5Si_3 pre-oxidized in O_2 followed by nitridation for 6 hours (Δm/m~7%). Marked areas show: 1. Ti_5Si_3, 2. $TiSi_2$, 3. TiN, 4. TiO_2+SiO_2, 5. mixture of TiO_2, SiO_2, TiN and Si

Discussion

As a basis for understanding the nitrogen effect on the oxidation behavior it is necessary to recall why Ti_5Si_3 possesses excellent oxidation resistance at 1000°C in O_2.

The fundamental phenomenon is that SiO_2 is a slow growing protective oxide at this temperature while TiO_2 is the fast-growing non-protective oxide by its nature due to the higher degree of lattice disorder[28]. In other words, sufficient oxidation resistance is only achieved if either only silica layer is formed or at least a continuous silica layer exists in the mixture of SiO_2 and TiO_2 oxide scale.

As literature and the present study indicated, a continuous silica layer forms upon oxidation of Ti_5Si_3 alloys in pure O_2. However this silica layer exhibits a temporary stability and experiences a breakaway degradation in air or in high nitrogen/oxygen atmosphere. Fig.24 shows a stability diagram for Ti and Si, each with a unit activity in nitrogen and oxygen at 1000°C. It is evident from this diagram that the stability of Si/SiO_2 is only slightly lower than that of Ti/TiO_2 at unit activities, a slight deviation from the unit activity may affect the order of stability of the oxides form. As shown in activity diagram for the Ti-Si-O system (Fig.25) at 1100°C[29], stability of oxide changes from TiO_2 to SiO_2 when composition of Si increases from 35.7 at.% to 39 at.% across the homogeneity range of Ti_5Si_3. For the actual stoichiometric alloy, the formation of silica is favored.

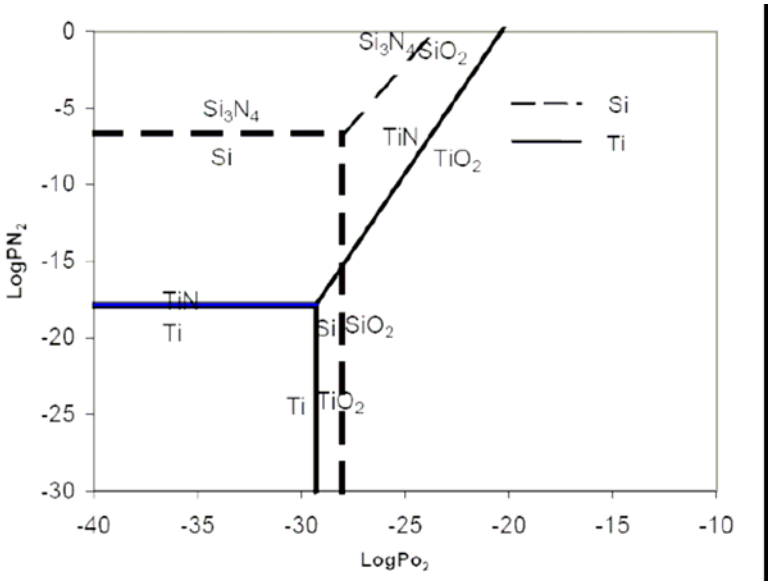

Figure 24 Stability diagram for Ti-Si-O-N system at 1000ºC with unit activity of Ti and Si

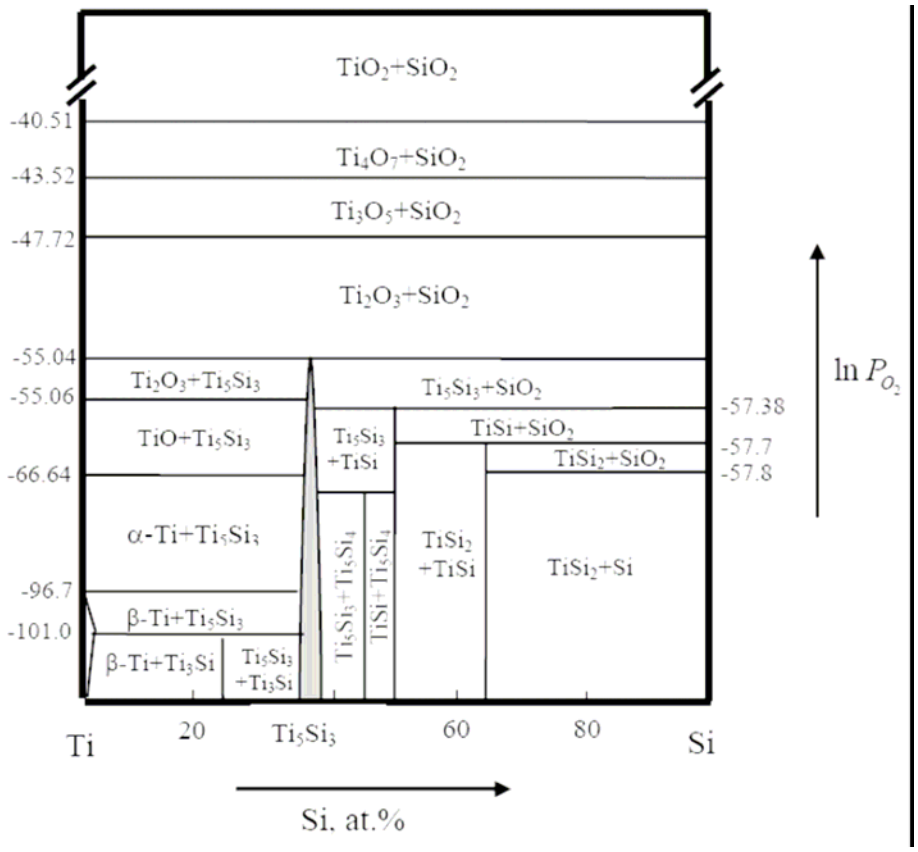

Figure 25 Activity diagram of Ti-Si-O system at 1100ºC

Nuclei of all potential corrosion products will form on alloy surface initially, for example, those that are thermodynamically favorable. For Ti_5Si_3 alloy, both TiO_2 and SiO_2 are formed in pure oxygen in the early stage. TiO_2 is a faster growing oxide compared to SiO_2. Due to the different stabilities of these two oxides, the SiO_2 nuclei are stable at low oxygen partial pressure beneath the outer, faster growing TiO_2 layer, and thus develop a thin continuous SiO_2 layer by lateral growth in the later stages. The slower growing silica partial layer can, from this stage on, act as a barrier for oxygen and titanium diffusion and thus slow down the oxidation rate. However, the formation of silica leads to Si-depletion (and Ti-enrichment), thus switching oxidation toward TiO/TiO_2 formation as the Ti activity increases

making Ti oxidation formation more favorable. The changes in activity of Ti and Si may lead to formation of alternating TiO_2 and SiO_2 or reach steady state activity for these two elements. The result usually is a scale with a complex scale structure: pure TiO_2 on the surface and silica layer with TiO_2 particles between outer scale and bulk alloy substrate. In air or other nitrogen/oxygen mixed atmosphere the scale structure is more complicated by the presence of nitrogen, which may lead to the formation of nitride subscale.

As mentioned above, nitride subscale was developed as Ti_5Si_3 was exposed to $N_2/O_2 \geq 3$ atmosphere. The TiN phase formed initially at the oxide/substrate interface is subsequently oxidized to TiO_2 preventing the formation of a continuous protective SiO_2 layer. In addition to thermodynamic and kinetic considerations, there are significant physical constraints in the nitridation/oxidation process. For instance, nitridation as well as oxidation of alloy result in non-trivial volume expansion, which leads to the disruption of initial protective oxide scale and impedes the establishment of permanent protective scale. Only if the activity of Ti is significantly lower than that of Si will the formation of a silica layer can be achieved at the scale/substrate interface. For instance, although breakaway oxidation occurs after 12 hours exposure to air for Ti_5Si_3, steady-state parabolic oxidation behavior was observed for $Ti_5Si_{3.2}$ up to 100 hours exposure in air. But one question remains unclear. Why Ti_5Si_3 is stable and nitride subscale does not form in $N_2/O_2 \leq 1$ atmosphere, even after 400 hours exposure? As we discussed before, the diffusion rate of nitrogen through oxide scale is much faster than that of oxygen. Thus the diffusing nitrogen should end up in the structure, perhaps distributed in the alloy interstitially or at the grain boundary. Additional work needs to be carried out to answer this question.

Conclusions

Reaction kinetics of Ti_5Si_3 in pure nitrogen and mixed N_2/O_2 atmosphere at 1000ºC has been studied. The influence of nitrogen on the oxidation behavior of Ti_5Si_3 has been discussed. The following conclusions can be drawn:

1. A faster linear reaction rate (about 0.17 mg/cm^2/hr) was observed when Ti_5Si_3 is exposed to nitrogen, and the nitridation process leads to a catastrophic, pest-like degradation of the sample
2. Ti_5Si_3 is stable for exposures up to 400 hours at 1000°C when the concentration of nitrogen is less than 50%. However, accelerated oxidation occurs after short exposures when concentration of nitrogen is more than 75%, and with the increasing nitrogen partial pressure time to breakaway degradation decreases
3. Though neither rutile or silica layer is an effective barrier for nitrogen penetration, a pre-formed oxide scale reduces the nitridation rate.

Acknowledgments

Ames laboratory is operated for the U.S. Department of Energy by Iowa State University under contract number W-7405-ENG-82.

References

[1] Seifert H. J., Lukas H. L., Petzow G., Z.Metallkd (1996) **87**(1):2-13.

[2] Frommeyer G., Rosenkranz R., Luedecke C., Zeitschrift fuer Metallkunde (1990) **81**(5):307-13.

[3] Schlesinger M. E., Chemical Review (1990) **90**:607-28.

[4] Williams J. J., Kramer M. J., Akinc M., Journal of Materials Research (2000) **15**(8):1773-79.

[5] Ikarashi Y., Ishizaki K., Nagai T. et al., Intermetallics (1996) **4**(1):141-45.

[6] Thom A. J., Akinc M., Cavin O. B. et al., Journal of Materials Science letters (1994) **13**:1657-60.

[7] Thom A. J., Kim Y., Akinc M., Materials Research Society Symposium Proceedings 288 (High-Temperature Ordered Intermetallic Alloys V), 1993, p.1037-42.

[8] Thom A. J., Meyer M. K., Kim Y. et al., In: Ravi V. A. et al. eds., Processing and Fabrication of Advanced Materials for High Temperature Application, 1994, p.413-38.

[9] Thom A. J., Akinc M., Advanced Ceramic for Structure and Tribological Applications (1995):619-27.

[10] Thom A. J., Meyer M. K., Williams J. J. et al., Processing and Fabrication of Advanced Materials for High Temperature Application (1995) **4**:139-42.

[11] Kim Y., Thom A. J., Akinc M., Processing and Fabrication of Advanced Materials for High Temperature Application (1993) **2**:189-208.

[12] Abba A., Galerie A., Caillet M., Oxidation of Metals (1982) **17**(1):43-54.

[13] Williams J. J., Akinc M., Oxidation of Metals (2002) **58**(1/2):57-71.

[14] Mitra R., Rama Rao V. V., Metallurgical and Materials Transactions A: Physical Metallurgy and Materials Science (1998) **29A**(6):1665-75.

[15] Taniguchi S., Minamida T., Shibata T., Materials Science Forum (1997) **251-254**:227-34.

[16] Thom A. J., Akinc M. US Patent # 5,580,518.

[17] Thom A. J., Meyer M. K., Williams J. J. et al., In: Srivatsan T. S., Moore J. J. eds., Processing and Fabrication of Advanced Materials IV, Cleveland, 1995, p.139-49.

[18] Rakowski J. M., Pettit F. S., Meier G. H. et al., Scripta Metallurgica et Materialia (1995) **33**(6):997-1003.

[19] Quadakkers W. J., Schaaf P., Zheng N. et al., Materials and Corrosion (1997) **48**(1):28-34.

[20] Melsheimer S., Fietzek M., Kolarik V. et al., Oxidation of Metals (1997) **47**(1/2):139-203.

[21] Wallace T. A., Clark R. K., Wiedemann K. E., Oxidation of Metals (1994) **42**(5/6):451-64.

[22] Rakowski J. M., D.; Pettit, F. S.; Meier, G. H.; Perkins, R. A. In: Newcomb S. B., Bennett M. J. eds., Microsc. Oxid. 2, 1993, p.476-87.

[23] Thom A. J., Kim Y., Akinc M., Materials Research Society Symposium Proceedings 288 (High-Temperature Ordered Intermetallic Alloys V), 1993, p.1037-42.

[24] Thom A. J., Meyer M. K., Kim Y. et al., In: Ravi V. A. et al. eds., Process Fabr. Adv. Mater. III, Proc. Symp., 3rd, 1994, p.413-38.

[25] Thom A. J., Akinc M., In: Hawthorne H. M., Troczynski T. eds., Proceedings of the International Symposium on Advanced Ceramics for Structural and Tribological Applications, 1995, p.619-27.

[26] Murata Y., Morinaga M., Shimamura Y. et al., In: Darolia R. eds., Struct. Intermet., 1st , 1993, p.247-56.

[27] Kofstad P., Anderson P. B., Krutaa O. J., Journal of Less Common Metals (1961):89.

[28] West A. R. Solid State Chemistry and Its Application, John Wiley & Sons, Singapore, 1989.

[29] Goldstein J. I., Choi S. K., Loo F. J. J. V. et al., Journal of American Ceramic Society (1995) **78**(2):313-22.

Chapter 3. Mechanism of High Temperature Oxidation of Ti_5Si_3-based Alloys

Zhihong Tang, Jason J, Williams, Andrew J. Thom and Mufit Akinc

A paper to be submitted to *Intermetallics*

Abstract

The isothermal oxidation behavior of binary and ternary Ti_5Si_3 alloy was investigated at 1000ºC in pure oxygen and nitrogen-containing atmosphere. Several critical issues regarding oxidation of Ti_5Si_3 at elevated temperatures were examined experimentally and theoretically. Although binary Ti_5Si_3 alloy within the homogeneity range can form silica-containing scale in pure oxygen atmosphere upon high temperature exposure, only the Si-rich binary alloy is oxidatively stable in air. Presence of nitrogen alters the oxidation behavior of Ti_5Si_3 at elevated temperature by nucleation and growth of a nitride subscale, which prevents the formation of protective silica-enrichment layer by embritlement of the alloy via nitrogen dissolution in the structure and leads to the accelerated degradation. The initial formation of silica, by either pre-oxidation or employing Si-rich alloy (i.e. $Ti_5Si_{3.2}$), inhibits the nucleation and growth of nitride subscale and enhance the oxidation resistance of Ti_5Si_3 in nitrogen containing atmosphere at elevated temperatures. C-doped alloys (i.e $Ti_5Si_3C_{0.5}$ and $Ti_5Si_{2.8}C_{0.5}$) possess excellent oxidation resistance in both pure oxygen and in nitrogen-containing atmospheres due to increased activity of Si relative to Ti which favors the formation of SiO_2 and inhibits of nitride formation beneath the oxide scale. In addition,

carbon doping may reduce the oxygen and/or nitrogen dissolution into the alloy thus reducing the degradation of the alloy.

Keywords: A. Titanium silicide; F. Corrosion behavior; B. Oxidation; B. alloy design

Introduction

Ti_5Si_3 has been extensively studied over the past decades as a candidate material for high temperature application due to its high melting point (2130ºC), low density (~4.26 g/cm^3), capacity to retain high strength up to 1200ºC, and good oxidation and creep resistance at and below 850ºC[1-7]. However, published studies on the oxidation resistance of Ti_5Si_3 above 850ºC are inconsistent, as shown in Table 4. Studies by Thom et al.[8, 9], Kim et al.[10] and Abba et al.[11] have reported poor oxidation resistance in air above 850 ºC, while studies by Mitra et al. [2] and Taniguchi et al. [12] reported excellent oxidation resistance in air up to 1250 ºC. One of the explanations for the discrepancies of oxidation behavior of Ti_5Si_3 is the slight variation in alloy composition and alloy synthesis methods employed in those studies. The samples in the studies by Thom et al.[8, 9], Kim et al.[10] and Abba et al. [11] were all reported to be a single phase and assumed to be stoichiometric Ti_5Si_3. Their samples formed a mixed rutile-silica scale in contact with the base alloy, upon exposure to air and poor oxidation resistance was reported. The studies that reported excellent oxidation resistance for Ti_5Si_3 at 1200 ºC reported that their samples contained a small amount of silicon-rich phases (Ti_5Si_4 or $TiSi_2$). These silicon-rich samples had exhibited excellent oxidation resistance in air due to the formation of a continuous protective SiO_2 scale.

Though there are some discrepancies, most studies reported totally different oxidation resistance behavior in air, versus in pure oxygen or Ar-21% O_2. For example, Williams et al.

[13] reported that Ti_5Si_3 shows slow parabolic oxidation kinetics in pure oxygen at 1000ºC while a "breakaway oxidation" is observed after 12 hours exposure to air. This, so called "nitrogen effect" is well established, the underlying mechanism still remains unknown.

Table 4 Scattering oxidation behavior of Ti_5Si_3-based alloys at high temperature

Composition	Processing Method	Oxidation Temp., ºC	Atmosphere	Oxidation behavior		Ref.
				Model	K[1]	
Ti_5Si_3	HIP	1000	Air	Cracking		[8]
Ti_5Si_3 coating on Ti	Deposition of Si	950	Air	Breakaway oxidation		[11]
Ti_5Si_3 with Ti_5Si_4 & TiSi	E-beam melting	1200	Air	Cubic	8×10^{-11}	[12]
Ti_5Si_3 with ~5% TiSi	Hot pressing of TiH_2/Si powder	1200	Air	Parabolic	5×10^{-3}	[2]
Ti_5Si_3	Arc-melting	1000	Ar-21%O_2	Parabolic	2×10^{-3}	[13]
Ti_5Si_3	Arc-melting	1000	Air	Breakaway oxidation after 12 hours		[13]
$Ti_5Si_{3.2}$	Arc-melting	1000	Air	Parabolic	5×10^{-5}	[13]
$Ti_5Si_3C_{0.5}$	Arc-melting	1000	Air	Parabolic	5×10^{-5}	[13]

[1]rate constant, for a parabolic model, $mg^2/cm^4/hr$; for a cubic model, $mg^3/cm^6/hr$.

Another factor that complicated the oxidation behavior of Ti_5Si_3 is that the samples used in most studies were assumed to be contaminated with interstitial impurity atoms because of the open Mn_5Si_3 prototype structure of Ti_5Si_3. Two recent studies by Radhakrishnan et al. [14] and Thom et al.[15] highlighted the difficulty of synthesizing and consolidating Ti_5Si_3 without contamination by carbon, nitrogen and/or oxygen by powder metallurgy. In particular, studies that use metal powder as a staring material are highly likely to contain an oxygen impurity of at least one or two weight percent. Furthermore, studies [13,

16] on the oxidation behavior of Ti_5Si_3 with interstitial oxygen or carbon intentionally added suggested that the addition of oxygen or carbon promote the formation of thin silica layer in the early stage of oxidation. However, only alloying with carbon showed dramatic improvement in the long-term oxidation resistance. Though the underlying mechanism of the improvement in oxidation resistance due to carbon addition remains largely unknown, preferential bonding of carbon to titanium, which decreases the activity of Ti while increasing the activity of Si in the alloy, was offered as a plausible mechanism. Unfortunately, most previous studies on the oxidation behavior of Ti_5Si_3 also suffered from interstitial impurities. Thus intrinsic oxidation behavior of stoichiometric Ti_5Si_3, the effects of ternary addition on the oxidation mechanism and influence of gas composition on the oxidation rate and oxide scale formation remain unclear.

The primary purpose of the present work is to study the oxidation behavior of pure Ti_5Si_3 to eliminate (at least minimize) the combinational effects of interstitial elements, and study the oxidation behavior of binary Ti_5Si_3 alloy in pure oxygen and nitrogen containing atmosphere at elevated temperatures. The possible mechanism of carbon addition for improving the oxidation resistance of Ti_5Si_3 alloy is also discussed.

Experimental procedure

$Ti_5Si_{3\pm x}$ (x=0, 0.2) and $Ti_5Si_3Z_{0.5}$ (Z=C, N and O) alloys were arc-melted in an ultra-high purity argon atmosphere from sponge titanium (Timet, 99.7 wt.%), silicon pieces (Alfa Aesar, 99.9999 wt.%) and spectrographic-grade graphite electrodes for carbon. The sponge titanium was pre-melted twice to volatilize surface contamination before being used in the synthesis. Each sample was remelted at least three times to insure homogenization. The total weight losses after arc-melting were generally much less than 0.5 wt.%. The arc-melted

samples were examined by X-ray diffraction (XRD) and metallography to confirm that they were single phase and well crystallized. In addition, chemical analysis indicated that total content of nitrogen and/or oxygen impurities was less than 0.09 wt.% for all samples.

All oxidation experiments were run on arc-melted materials. Obtaining high purity sample is crucial to study the intrinsic oxidation behavior of Ti_5Si_3-based materials. Because the as-arc-melted ingots contain macrocracks, they were crushed to granule materials and sieved through 600 μm. These granular materials appear to be crack-free based on the SEM observation.

All isothermal oxidation experiments were conducted on granule materials using a specially designed thermogravimetric analyzer (TGA). Each sample, which weighed approximately 80 mg and had a surface area of about 18 cm^2, was placed in a quartz sample pan and suspended from a Cahn 2000 microbalance using a sapphire wire. The TGA apparatus was then evacuated to about 8 Pa and subsequently backfilled with argon. The evacuation-back filling sequence was repeated four times to purge the ambient air in the TGA system. Oxidizing atmosphere included oxygen, 79% argon-21% O_2, zero-grade air, or the mixture of nitrogen and oxygen with preset ratios. The gas mixtures were precisely regulated using mass flow controllers. The oxidizing gas was flowed for 2 hours at 50 cm^3/min with the sample at 250ºC. This process established a pure atmosphere as well as volatilized the possible surface contaminations from the sample. Finally, the sample was heated to 1000°C at 20°C/min and held for 25 to 400 hours. The gas flow was maintained at 50 cm^3/min throughout the experiment. To compare the data obtained from these experiments, the rate constants were calculated from the measured weight grain as a function of exposure time.

After isothermal oxidation, the granule samples were ground to ≤ 20 μm for phase analysis using XRD. An α-Al_2O_3 standard (NIST SRM676) was added to most samples for accurate lattice parameter refinement and phase composition determination. Rietveld analysis software (GSAS, Los Alamos National Laboratory 1985) was used to determine the phase fractions and lattice parameters. Cross-section of these oxide scales were then characterized by scanning electron microscopy (SEM) equipped with an energy dispersion spectrometer (EDS). The phases determined from XRD were correlated to the scale morphologies observed by SEM/EDS.

Results

Oxidation behavior in pure oxygen

Fig.26 shows the results of thermogravimetric analyses (TGA) during isothermal oxidation of three single phase Ti_5Si_3-based alloy at 1000ºC in pure oxygen. In all three cases, the mass change vs. time curves follow a parabolic law ($\Delta m^2=K_p t$), which is consistent with the previous studies by Abba et al. [11] and Taniguchi et al. [12]. It is obvious that the rate of weight gain decreases with increasing silicon content for binary Ti_5Si_3 alloy. The mass gain for $Ti_5Si_{3.2}$ is two and three times lower than that for Ti_5Si_3 and $Ti_5Si_{2.8}$, respectively, for 100 hours exposure. The isothermal oxidation was also conducted in Ar-21%O_2 for stochiometric Ti_5Si_3 alloy for comparison, it is clear that the mass gain in Ar-21%O_2 is 15% less than that in pure oxygen. It should be noted that the oxidation of binary Ti_5Si_3 alloy results in a simultaneous oxygen dissolution ($K_{p,od}$) and oxide scale ($K_{p,os}$) formation:

$$\frac{\Delta m}{m} = \left\{K_{p,os} + K_{p,od}\right\}\sqrt{t} = K_p\sqrt{t}$$

The influence of oxygen on oxidation behavior will be discussed later.

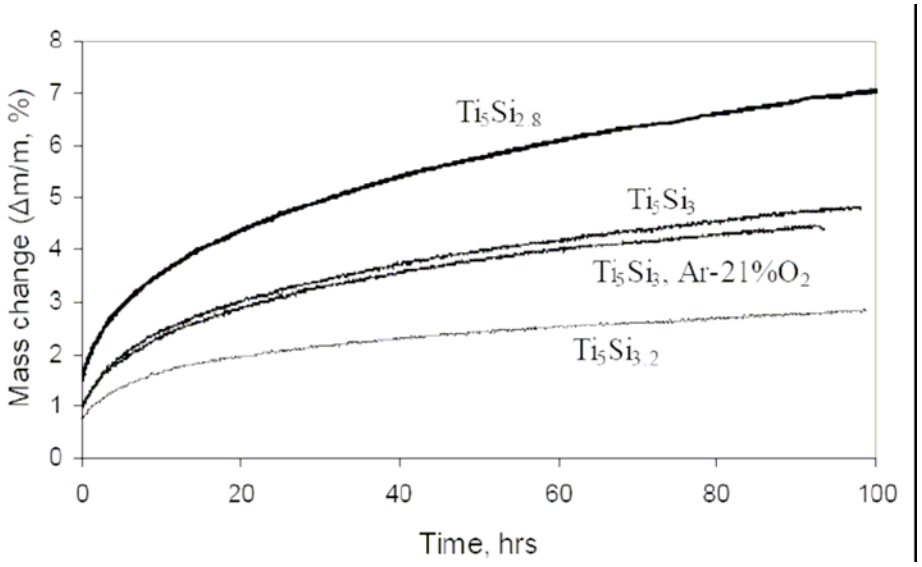

Figure 26 Oxidation isotherms at 1000ºC of three binary Ti_5Si_3-based alloys in flowing pure oxygen and Ar-21% O_2

The oxide scale formed during the oxidation of binary Ti_5Si_3 alloy in pure oxygen generally possesses common characteristics: double oxide layer formed on alloy as shown in Fig.27. The outer layer consists of rather pure TiO_2, while the inner layer is continuous layer of silica with interspersed TiO_2 grains. Similar double oxide layer microstructure was reported on oxidation of Ti_5Si_3 coating on Ti substrate above 900ºC (Abba et al. [11]), and oxidation of $TiSi_2$ at 1100 ºC (Melsheimer et al. [17]). The thickness of outer rutile layer and inner mixed layer clearly differ with increasing Si content in binary alloy.

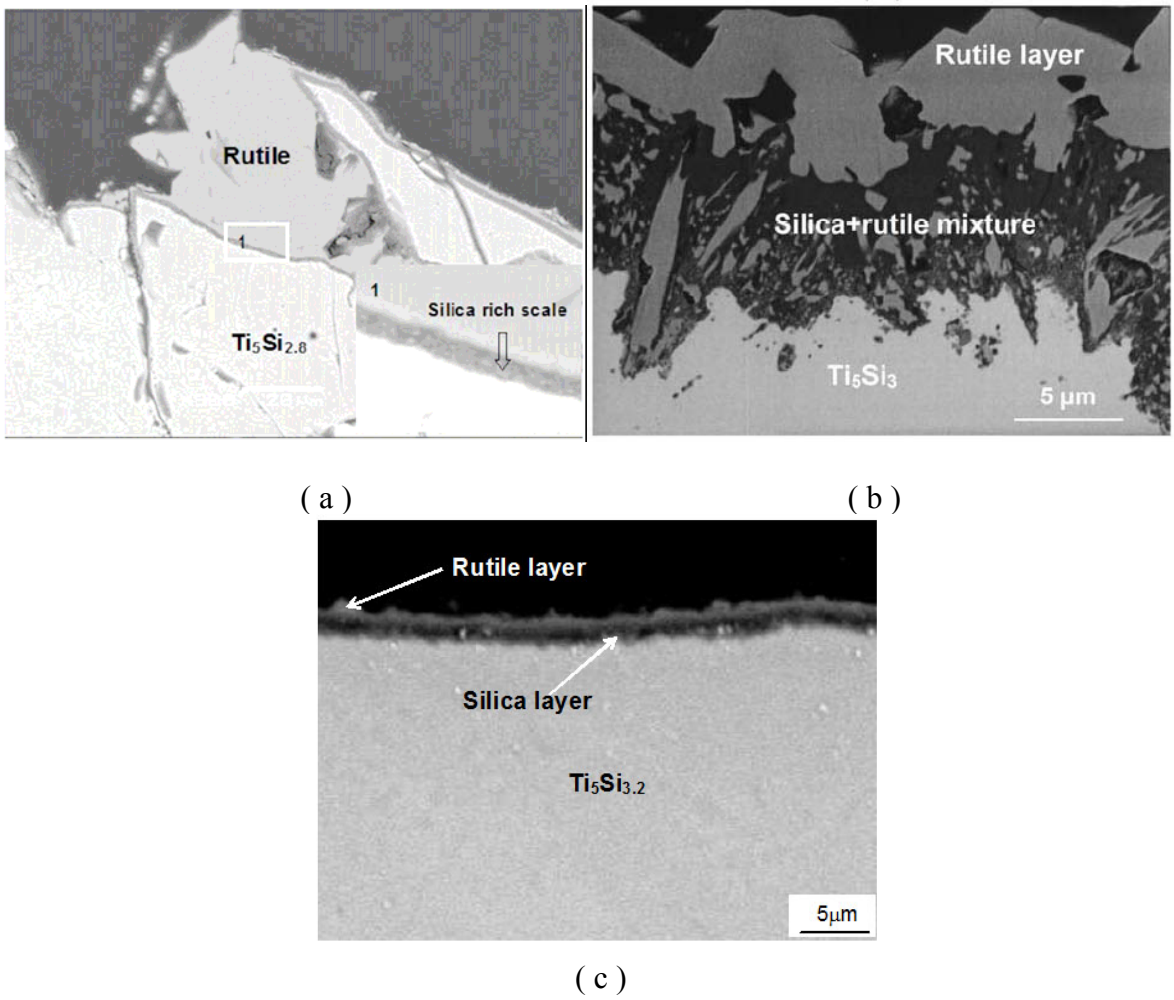

Figure 27 SEM micrographs showing the cross-section of oxide scale: a) $Ti_5Si_{2.8}$, b) Ti_5Si_3, and c) $Ti_5Si_{3.2}$ after 100 hours exposure to flowing pure oxygen at 1000ºC

For Ti_5Si_3, the scale consists of a 5 µm thick outer TiO_2 layer and a 5 µm thick inner mixed (SiO_2 + TiO_2) layer. Silica content is higher adjacent to outer TiO_2 layer. For $Ti_5Si_{2.8}$ large rutile nodules (tens of microns) on the surface formed due to increasing titanium activity. Beneath the rutile nodules 2 µm thick continuous silica layer is observed. For silica rich composition, $Ti_5Si_{3.2}$, an inner 2 µm thick continuous silica layer was observed, while the thickness of surface rutile layer reduced to about 1 µm, suggesting the oxidation of titanium was suppressed with increasing silicon content in the alloy.

Effect of nitrogen

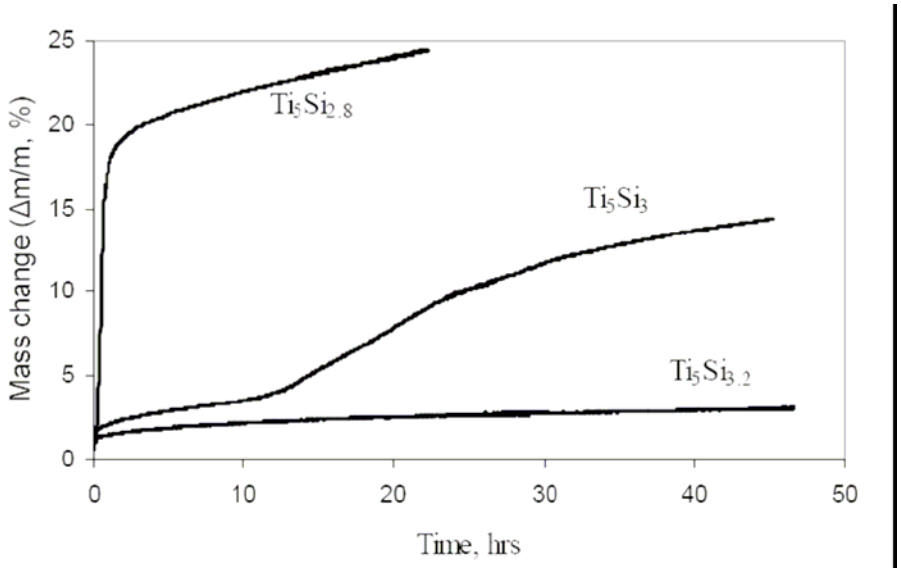

Figure 28 Oxidation isotherms at 1000ºC of three binary Ti_5Si_3-based alloys in flowing air

Fig.28 shows TGA results during isothermal oxidation of three binary Ti_5Si_3 alloy in air at 1000ºC. Unlike in pure oxygen in which all three alloys exhibited parabolic oxidation behavior with protective silica layer on the surface, the oxidation kinetics in air are totally different for Ti_5Si_3 and $Ti_5Si_{2.8}$ alloys. Only for Si-rich $Ti_5Si_{3.2}$ alloy does the mass gain obey a parabolic time dependence, and a thin protective silica layer formed even after 300 hours of exposure (Fig.29a). For Si-deficient $Ti_5Si_{2.8}$ alloy, a rapid linear oxidation rate was observed at the early stages and the sample was almost completely consumed after 20 hours. The metallographic examination of a cross-section shows fragmentation of granules and disruption of continuous silica-rich layer (Fig.29c). X-Ray diffraction pattern of the oxidized surface revealed TiN and Si peaks in addition to expected TiO_2. Presence of TiN is attributed to nitridation by N_2 in the reaction atmosphere. For Ti_5Si_3, TGA curve is more complex than that in pure O_2 or Ar-21%O_2. In the short time, steady-state parabolic oxidation behavior

with parabolic rate constant of approximately 3×10^{-4} $mg^2/cm^4/hr$ was observed. A thin protective silica layer formed in the early stage. However, the mass gain accelerates after 12 hours of exposure, indicating partial loss of protective scale. The accelerated oxidation is apparently related to the growth of subscale phases, such as $TiSi_2$ and TiN, as shown in Fig.29.b. The growth of subscale phases beneath the oxide scale and later oxidation causes a large volume expansion. The stress developed due to this volume expansion apparently disrupts the external oxide scale resulting in cracking of the oxide scale. The XRD analysis was performed on oxidized sample before and after accelerated oxidation and supports this argument. Only TiO_2 and Ti_5Si_3 peaks were observed before accelerated oxidation, while TiN and $TiSi_2$ phases appear after breakaway point and amount of TiN and $TiSi_2$ increases with increasing exposure time. Thus it is clear that nitrogen plays an important role in the oxidation behavior of Ti_5Si_3 alloy.

The reaction kinetics of Ti_5Si_3 in pure nitrogen was plotted in Fig.30. Ti_5Si_3 shows high reactivity and fast linear reaction rate when exposed to pure nitrogen at 1000°C. A rough estimate of the rate constant at an early stage is about 0.17 $mg/cm^2/h$. XRD analysis revealed that almost all Ti_5Si_3 is consumed after 18 hours exposure and the main nitridation products are TiN, $TiSi_2$ and Si. A small amount of TiO_2 is also found in the reaction product due to extremely low oxygen equilibrium partial pressure for rutile formation ($\sim10^{-27}$ atm). Cross-sectioning of the nitrided sample revealed that initial coarse granule fractured into small pieces with cracks between the oxide and nitride scales. Based on the experimental evidence, the following set of reactions are proposed for nitridation:

$$Ti_5Si_3 + 1.75N_2 \rightarrow 3.5TiN + 1.5TiSi_2$$

$$Ti_5Si_3 + 2.5N_2 \rightarrow 5TiN + 3Si$$

Nitridation experiments were also performed on other binary alloys ($Ti_5Si_{3.2}$ and $Ti_5Si_{2.8}$) and a ternary ($Ti_5Si_3C_{0.5}$) alloy, and similar reaction rates were observed. Initial coarse granule always fractured into smaller pieces and none formed a protective layer. It is clear that nitridation process leads to a catastrophic, pest-like degradation of the alloys.

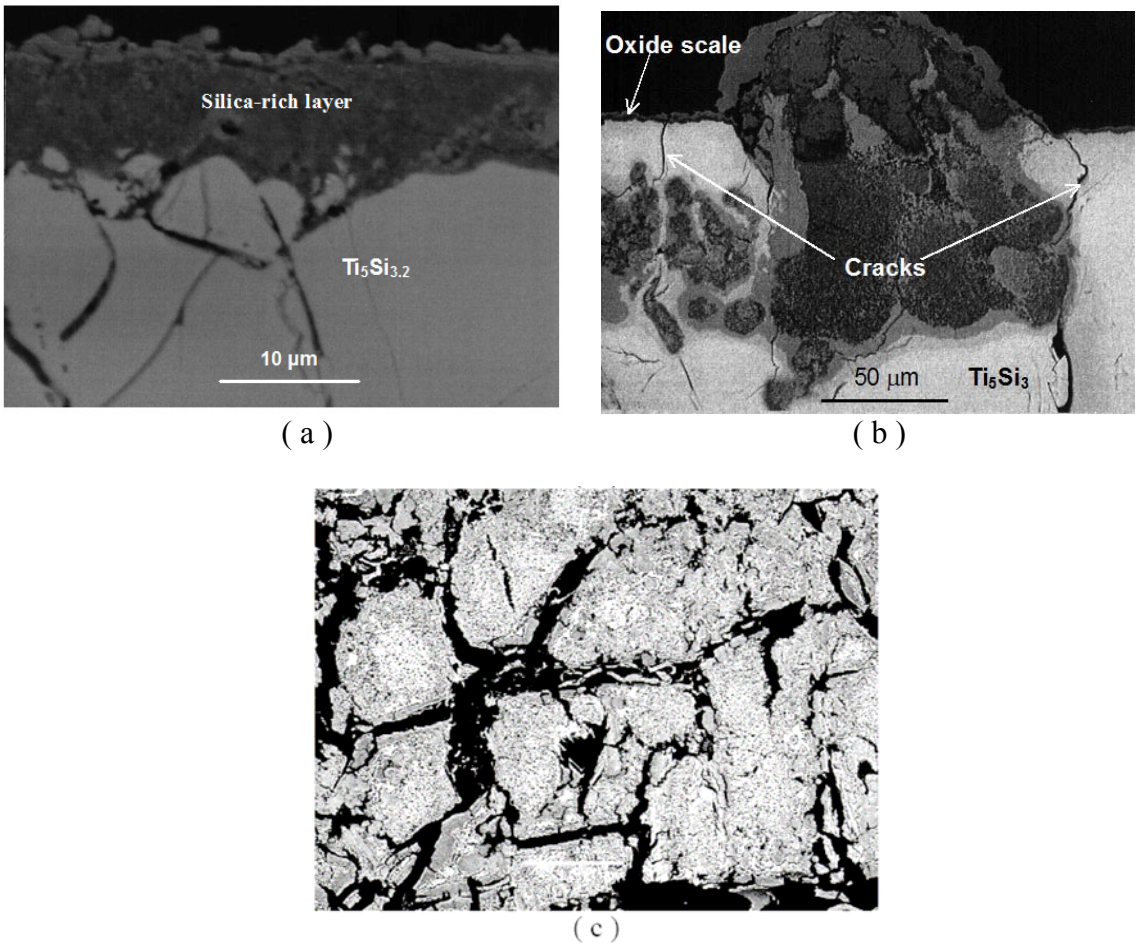

Figure 29 SEM micrographs showing the cross section of oxide scale after exposure in air at 1000ºC: a) $Ti_5Si_{3.2}$ after 300 hours, b) Ti_5Si_3 after 25 hours and c) $Ti_5Si_{2.8}$ after 25hrs

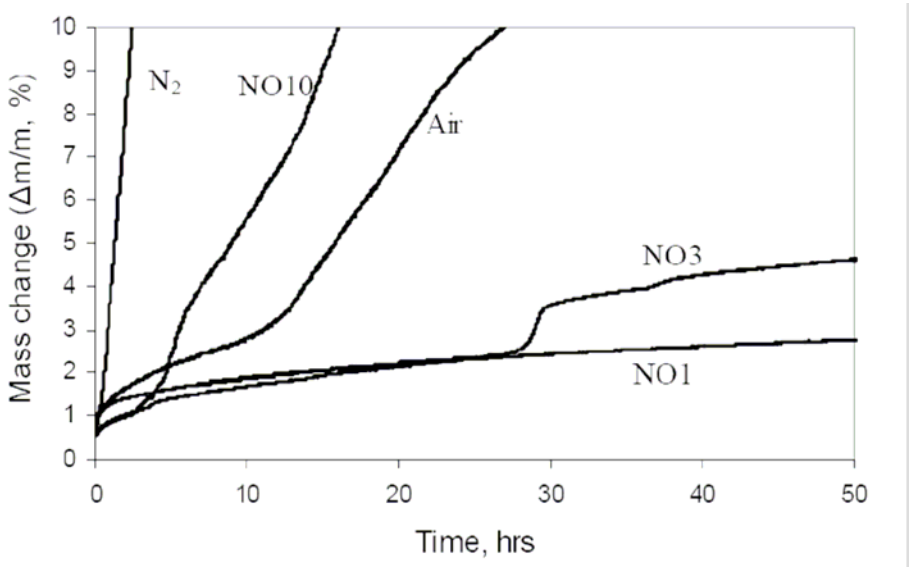

Figure 30 Oxidation isotherms at 1000ºC of Ti_5Si_3 in N_2+O_2 atmospheres. The reaction kinetics in pure nitrogen is also plotted for comparison. The designation NO10 refers to N_2/O_2=10 in the gas mixture. The reaction gas is air if not noted on the isotherm

The nitrogen effect on oxidation behavior of Ti_5Si_3 at 1000°C was further examined by varying N_2/O_2 ratio. The TGA results are shown in Fig.30. At $N_2/O_2 \leq 1$, a steady-state parabolic oxidation behavior with an oxidation rate constant of about 3×10^{-4} $mg^2/cm^4/hr$ was observed up to 400 hrs, which is comparable to the rate of Si oxidation in dry oxygen (2×10^{-4} $mg^2/cm^4/hr$). It indicates that a continuous protective silica layer was established. At higher nitrogen/oxygen atmospheres ($N_2/O_2\geq3$), a breakaway oxidation occurs with the time to breakaway decreasing as the nitrogen/oxygen ratio increases. Breakaway oxidation occurs after about 28 hrs for $N_2/O_2 = 3$, while the time to breakaway decreases to 12 and 3 hours for $N_2/O_2 = 4$ and 10, respectively. Prior to breakaway, samples show parabolic oxidation behavior, and the rate constant converges to about 4×10^{-4} $mg^2/cm^4/hr$. In fact, the rate constant of sample prior to breakaway is similar to those of samples with no breakaway and

to the oxidation of Si in dry oxygen (2×10^{-4} $mg^2/cm^4/hr$). This suggests that a thin protective silica layer was established prior to breakaway.

The XRD pattern of an oxidized sample showed the presence of Si, $TiSi_2$ and TiN along with TiO_2, and is consistent with the nitridation reactions discussed above. However, addition of 10% oxygen has retarded the nitridation reaction since unreacted Ti_5Si_3 is still present after 25 hours exposure.

Effects of ternary alloying elements

The effects of ternary addition of carbon, nitrogen and oxygen on the oxidation behavior of Ti_5Si_3 in air at 1000ºC are shown in Fig.31. At the initial stage, all ternary alloys show smaller mass gains than stochimetric Ti_5Si_3 due to reduced dissolution of oxygen or nitrogen. Thermodynamic calculations by Wakelkamp [18] and Goldstein [19] showed that addition of carbon, nitrogen and oxygen increase the activity ratio of Si to Ti in the alloy and will be expected to favor the formation of SiO_2 in the early stage. This is confirmed by microstructural observations, which revealed that a thin silica layer formed on all ternary alloys, as shown in Fig.32a. However, only $Ti_5Si_3C_{0.5}$ shows a long-time oxidative stability. Accelerated oxidation occurred on both $Ti_5Si_3O_{0.5}$ and $Ti_5Si_3N_{0.5}$ alloy after several hours. Carbon containing alloy $Ti_5Si_3C_{0.5}$ exhibited an excellent oxidation resistance even in N_2/O_2=10 atmosphere though total weight gain was higher than that was observed in air.

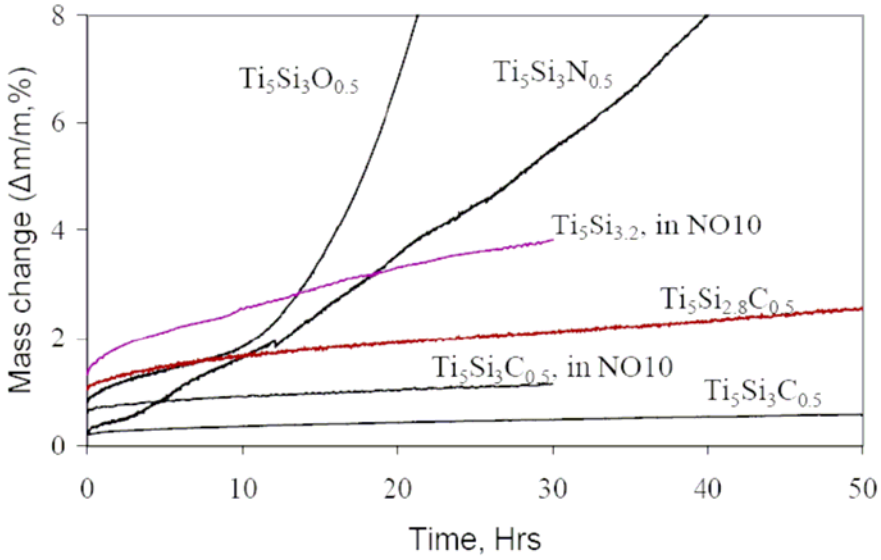

Figure 31 Oxidation isotherms of selected binary and ternary Ti_5Si_3-based alloys in N_2+O_2 atmospheres

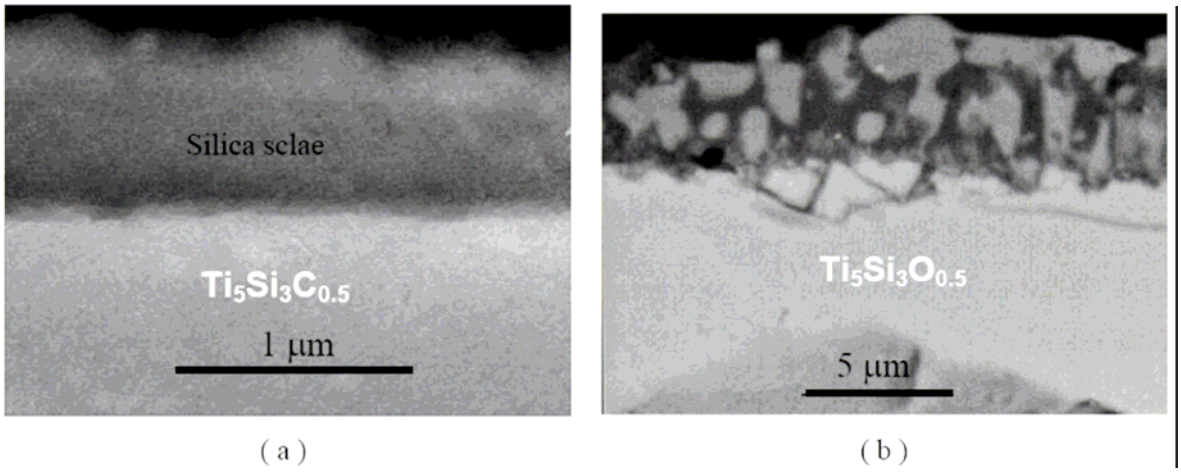

Figure 32 SEM micrographs showing the cross section of oxide scale for: a) $Ti_5Si_3C_{0.5}$ after one hour exposure at 1000°C. Similar scale morphology was also observed in $Ti_5Si_3O_{0.5}$ and $Ti_5Si_3O_{0.5}$ alloys, b) $Ti_5Si_3O_{0.5}$ after 10 hours exposure at 1000°C

More interestingly, Si-deficient $Ti_5Si_{2.8}C_{0.5}$ alloy also revealed excellent oxidation resistance. This suggests that underlying mechanism for improved oxidation resistance is more than just the activity ratio of Si to Ti for ternary alloys. It appears that adding carbon

has a profound effect on the oxidation resistance, even for hypo-stoichiometric binary Ti_5Si_3. The XRD results showed that the lattice parameters in two C-doped alloys remain unchanged, suggesting negligible dissolution of nitrogen or oxygen into interstitial site of C-doped alloy and may be responsible for improvement of oxidation resistance. $Ti_5Si_3N_{0.5}$ and $Ti_5Si_3O_{0.5}$ began to show a greater enrichment of TiO_2 in the scale after four and ten hours, respectively. Additionally, $Ti_5Si_3N_{0.25}$ showed isolated regions of internal nitridation after 10 hours, similar to nodules observed during the oxidation of Ti_5Si_3 in air. Clearly, the saturation or dissolution of oxygen or nitrogen in Ti_5Si_3 alloy has a critical role in the elevated temperature oxidation behavior of Ti_5Si_3.

Discussion

Thermodynamic stability

The oxidation resistance of alloys depends on the formation of a continuous protective oxide scale, in which the diffusion rate of oxygen and metal are sufficiently low that they grow at an acceptable slow rate. Al_2O_3, Cr_2O_3 and SiO_2 are primary oxides used for protection. Thus, if a continuous layer of the protective oxide is established, the oxygen partial pressure at the alloy/oxide interface is reduced below the critical level, at which the growth of less-protective oxide is prevented. For the Ti-Si system, rutile thermodynamically is slightly more stable than SiO_2 at unit activity, thus only slight difference in the activity of Ti and/or Si may reverse the stability of the oxide forms. Fig.33 shows the Ti-Si binary phase diagram and estimated titanium and silicon activity as a function of composition at 1100ºC. The activities of Si (a_{Si})and Ti (a_{Ti}) are much lower than unity for the compounds of interest, namely Ti_3Si, Ti_5Si_3, TiSi and $TiSi_2$. In particular, a_{Si}/ a_{Ti} increases by more than twelve

orders of magnitude when composition of silicon increases from 35.7 at.% ($Ti_5Si_{2.77}$) to 39.0 at.% ($Ti_5Si_{3.20}$) across the homogeneity range of Ti_5Si_3.

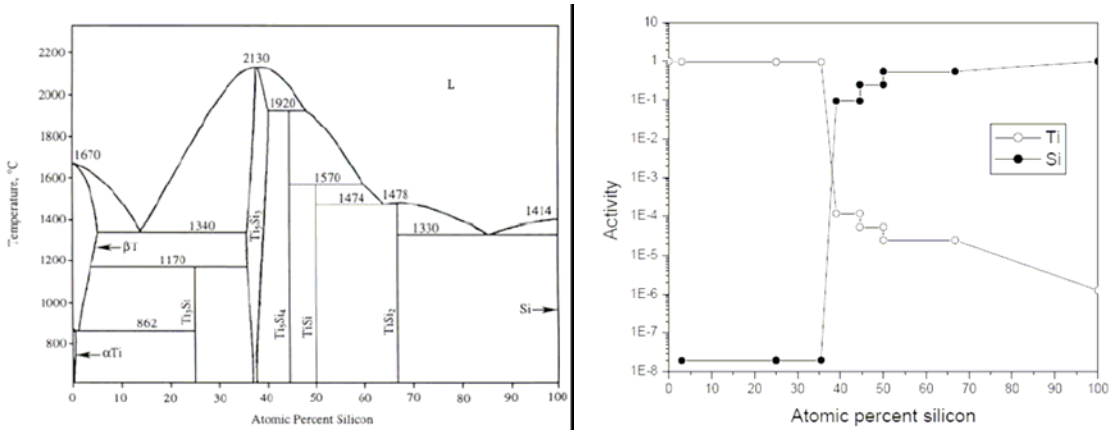

Figure 33 Binary phase diagram for the Ti-Si system and estimated activities of Si and Ti at 1300K based on the data in ref.[18]. The activities remain constant in two-phase regions. Greater changes occur in the stability range of various single phases

Fig.34 shows the stability diagram for Ti_5Si_3 in $O_2 + N_2$ atmosphere at 1100ºC, at $a_{Ti} = 5.6\times10^{-3}$ and $a_{Si} = 1.29\times10^{-4}$ [19]. The shift of these line due to change in activities by Si-depletion and Ti-enrichment is indicated in Fig.34a. Thus, for Ti_5Si_3 alloy, the formation of TiO_2 is favored upon oxidation in pure oxygen as the oxygen partial pressure of Si/SiO_2 system is greater that of Ti/TiO_2 system. Nevertheless, the formation of SiO_2 enrichment layer is often observed in the experiment. This is because it leaves a Si-rich layer beneath with a higher a_{Si} once Ti on the surface is oxidized, switching to Si/SiO_2 formation a_{Si} increases. On the other hand, from purely kinetics considerations, since the SiO_2 growth rate is much lower than TiO_2, Ti ions at the metal/oxide interface diffuse through the SiO_2 layer and form TiO_2. As a result, this leads to a scale with a graded structure. The fraction of TiO_2 grains increase going from surface to oxide/alloy interface. Platinum marker experiments by Abba et al. [11] confirmed that inner mixed layer grew inwards and while TiO_2 layer grew

outwards. For Si-depleted $Ti_5Si_{2.8}$ alloy, the initiation of SiO_2 formation is more difficult due to low a_{Si}, therefore more TiO_2 grows on the surface as shown in Fig.27a. For Si-rich $Ti_5Si_{3.2}$ alloy, SiO_2 is more stable than TiO_2, thus formation of SiO_2 is favored.

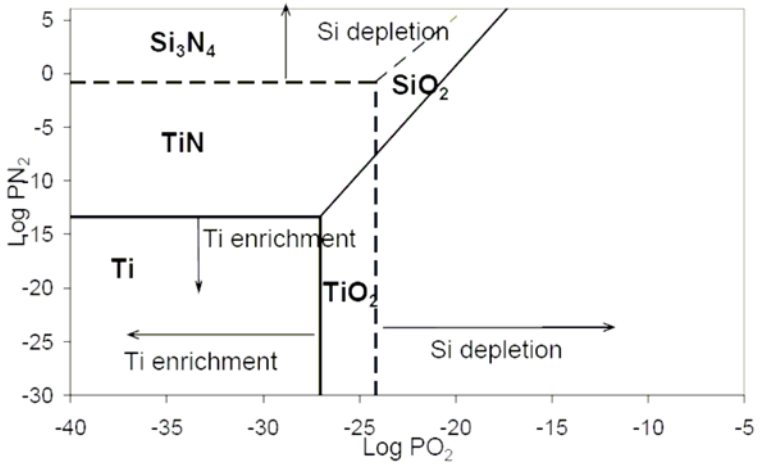

(a)

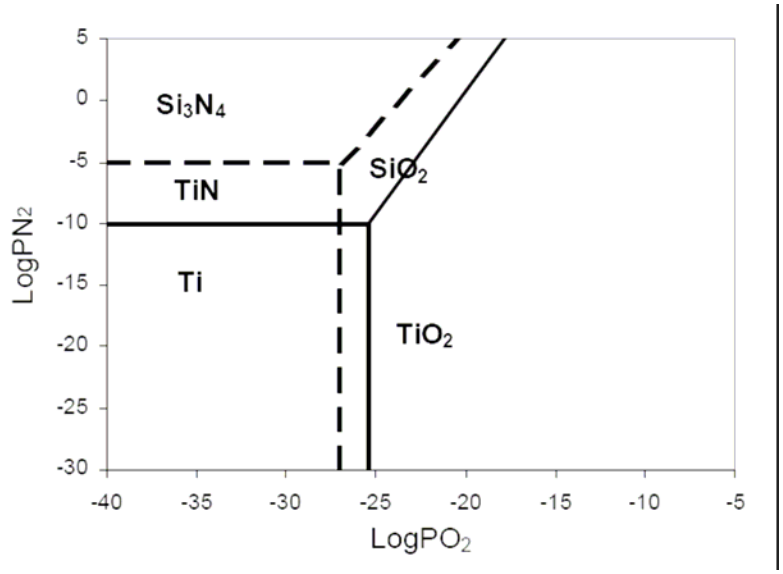

(b)

Figure 34 Stability diagrams for oxides and nitrides starting form pure Ti and Si in a) Ti_5Si_3 with $a_{Ti} = 5.6\times10^{-3}$; $a_{Si} = 1.29\times10^{-4}$ and, b) $Ti_5Si_{3.2}$ with $a_{Ti} = 2.2\times10^{-4}$; $a_{Si} = 0.04$

Nitrogen

In N_2-containing atmosphere, formation of silica layer is complicated by the formation of nitride at the scale/alloy interface and nitride is later oxidized to form the respective oxides. At equivalent activities, oxides are always thermodynamically favored over nitrides. However, as the oxide scales develop, oxygen partial pressure is reduced to the equilibrium value of metal/oxide, making nitride subscale formation thermodynamically favorable provided that a transport mechanism is available for nitrogen to diffuse through the oxide scale. In Ti-Si binary system, the dissociation pressure of Si_3N_4 is quite high at 1000ºC, while TiN is thermodynamically more stable. Indeed, TiN was the only nitride observed during the oxidation of Ti_5Si_3 in N_2+O_2 atmosphere. Nitridation experiments reveal that all Ti_5Si_3-based alloys exhibit a catastrophic, pest-like degradation, even for $Ti_5Si_{3.2}$ and $Ti_5Si_3C_{0.5}$ alloys which can form protective silica scale after long time exposure at 1000ºC in N_2+O_2 atmosphere.

For Ti_5Si_3 alloy, after a short exposure to N_2+O_2, a thin SiO_2 layer intermixed with TiO_2 grains forms. The oxygen partial pressure was cut down to equilibrium pressure of Si/SiO_2 as is the case in the case when alloy is exposed to oxygen atmosphere. Formation of TiN at the oxide/alloy interface depends on the nitrogen diffusion through the oxide layer. In fact, macro- or micro-cracking caused by growth stress or embitterment by dissolution of nitrogen (and/or oxygen) provides an easy path for nitrogen transport. As shown in Fig.29b, extensive internal nitridation leads to the formation of nodules consisting of TiO_2, TiN and $TiSi_2$. As oxygen continues diffuse inward, the TiN particles formed at the scale/alloy interface become unstable and oxidize to TiO_2. The released nitrogen diffuses into the alloy replenishing TiN phase. The net result being TiN forms by nitrogen and is consumed by

oxygen. The scale/alloy interface moves into the bulk alloy. The formation of nitride subscale clearly plays a critical role in the formation of mixed TiO_2+SiO_2 scale and disruption the continuous protective SiO_2 layer.

For $Ti_5Si_{3.2}$ alloy, lower a_{Ti} leads to higher dissociation pressure of TiN, requiring a higher P_{N2} to form a TiN scale at the scale/alloy interface. In addition, the higher a_{Si} shifts the stability of the oxide from TiO_2 to SiO_2, leading to formation of a dense SiO_2 layer. The transport of nitrogen through the oxide scale becomes negligible. This model is substantiated by experiments that when Ti_5Si_3 is pre-oxidized in pure oxygen followed by oxidation in air, no accelerated oxidation was observed, and no nitride could be found at the Ti_5Si_3/alloy interface.

Solubility of small atoms in the structure

Ti_5Si_3 has the hexagonal Mn_5Si_3 type (space group $P6_3/mcm$). The structure consists of essentially two chains of atoms: one being a linear chain of titanium atoms, the other being a chain of face-shared octahedral formed by six titanium atoms, as shown in Fig.35 [20, 21]. The interstitial site at the center of the octahedra has a diameter of approximately 1.34Å, which is large enough to accommodate second period elements. Studies by Wakelkamp [18] and Goldstein et al. [19] revealed that up to 11 at.% nitrogen or oxygen can be dissolved in Ti_5Si_3 alloy. The dissolution of oxygen or nitrogen in Ti_5Si_3 is thermodynamically favorable as shown in Table 5.

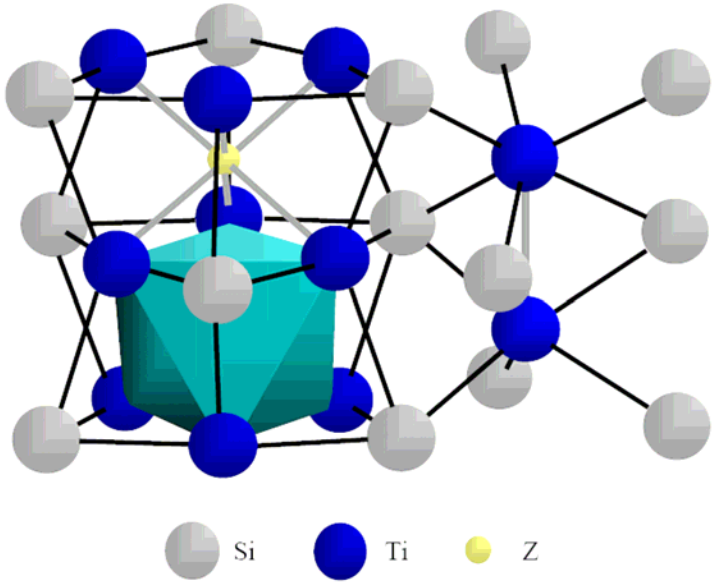

Figure 35 Partial crystal structure of $Ti_5Si_3Z_x$. Interstitial atom (Z) sits at the center of the irregular, face-sharing octahdra of Ti atoms

Table 5 Assessed Gibbs free energy of formation, ΔG_f^o * ,for Ti_5Si_3 and Ti_5Si_3Z (Z=C, N and O)

Ti_5Si_3	Ti_5Si_3C	Ti_5Si_3N	Ti_5Si_3O
-73.7	-77.2	-82	-104

*Values are in kJ/g·at.

Williams et al. found that lattice parameter of Ti_5Si_3 along the **a** and **c** axes decreases linearly with the occupancy of the interstitial site. Thus, dissolution of oxygen and nitrogen during oxidation can be estimated from the lattice parameter measurements. Fig.36 shows variation of lattice parameters along the **a** and **c** axes as a function of exposure time during oxidation of Ti_5Si_3 and $Ti_5Si_3C_{0.5}$ in pure oxygen and air at 1000ºC. For Ti_5Si_3, both **a** and **c** lattice parameters decrease sharply in the first few hours in pure oxygen or air indicating rapid dissolution of oxygen or nitrogen into the alloy and contribute to mass gain, after this

initial period the lattice parameter remain more or less constant. The final concentration of interstitial oxygen in Ti_5Si_3 was estimated to be approximately 6 at.% in pure oxygen. The rate of change in lattice parameter in air is faster than that in pure oxygen because nitrogen contracts the lattice more than oxygen does. It should be noted that there is an inflection point in lattice parameter vs. time curve at about 15 hours. This may be associated with breakaway oxidation of Ti_5Si_3 in air (after 12 hours) as a result of nucleation and growth of nitride subscale at the scale/alloy interface. This leads to an argument that the dissolution of nitrogen increases the nitrogen gradient at the scale alloy interface and facilitates the formation of nitride subscale. This argument is supported by the oxidation behavior of $Ti_5Si_{3.2}$ and $Ti_5Si_3C_{0.5}$ in which dissolution of nitrogen rarely occurs due to saturated structure and no nitride subscale formed beneath the oxide scale. Alternatively, one can make an argument that dissolution of nitrogen may result in embrittlement during elevated temperature oxidation in air and promote nitride formation by providing an easy transport path for nitrogen, as observed in higher N_2 containing atmosphere.

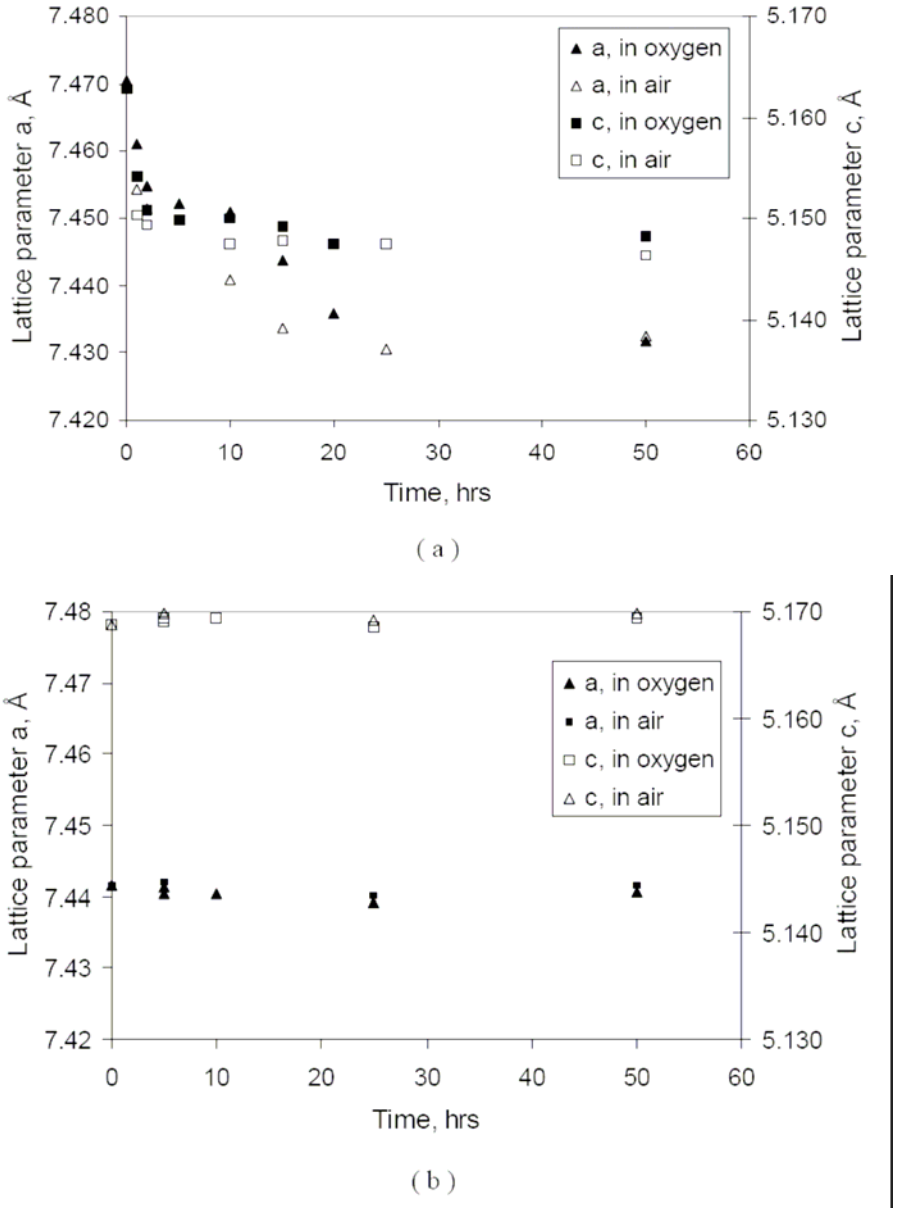

Figure 36 Change Lattice parameter of a) Ti_5Si_3 and b) $Ti_5Si_3C_{0.5}$ as a function of exposure time after oxidation in pure oxygen and in air

The oxidation of Ti_5Si_3 is a complex process that involves simultaneous oxygen dissolution and oxide scale formation and the oxygen/nitrogen gradient in the alloy beneath the scale leading to a crossover from protective to non-protective scale evolution. Therefore

the dissolution of oxygen or nitrogen in the alloy may have profound effect in the overall oxidation reaction.

Conclusions

Binary Ti_5Si_3 alloys show slow parabolic oxidation kinetics in pure oxygen or Ar-21% O_2 over the whole homogeneity range (from $Ti_5Si_{2.8}$ to $Ti_5Si_{3.2}$), while only $Ti_5Si_{3.2}$ alloy remains oxidatively stable in nitrogen containing atmosphere. The accelerated oxidation occurs for stoichiometric Ti_5Si_3 alloy after a short period in air or in nitrogen rich atmosphere. The breakaway oxidation in air is linked to nucleation and growth of subscale TiN beneath the oxide scale and inability to establish a continuous silica layer. Formation of nitride subscale may be avoided when the concentration of N_2 is less than 50% .

$Ti_5Si_{3.2}$ and $Ti_5Si_3C_{0.5}$ alloys exhibited an excellent oxidation resistance in nitrogen containing atmosphere. Two possible mechanisms may contribute to this: i) increasing a_{Si}/a_{Ti} favors the formation of SiO_2 over TiO_2; ii) limited dissolution of nitrogen into interstitial site of Ti_5Si_3 structure inhibits the formation of the nitride subscale.

Acknowledgements

"This manuscript has been authored, in whole or in part, under Contract No. DE-AC02-07CH11358 with the U.S. Department of Energy. The United States Government retains and the publisher, by accepting the article for publication, acknowledges that the United States Government retains a non-exclusive, paid-up, irrevocable, world-wide license to publish or reproduce the published form of this manuscript, or allow others to do so, for United States Government purposes."

References

[1] Meschter PJ, Schwartz DS. Silicide-matrix materials for high-temperature applications. JOM 41 (1989) 52.

[2] Mitra R, Rama Rao VV. Elevated-temperature oxidation behavior of titanium silicide and titanium silicide-based alloy and composite. Metallurgical and Materials Transactions A: Physical Metallurgy and Materials Science 29A (1998) 1665.

[3] Mitra R. Mechanical behaviour and oxidation resistance of structural silicides. International Materials Reviews 51 (2006) 13.

[4] Mitra R. Microstructure and mechanical behavior of reaction hot-pressed titanium silicide and titanium silicide-based alloys and composites. Metallurgical and Materials Transactions A: Physical Metallurgy and Materials Science 29A (1998) 1629.

[5] Seifert HJ, Lukas HL, Petzow G. Thermodynamic optimization of the Ti-Si system. Zeitschrift fuer Metallkunde 87 (1996) 2.

[6] Rosenkranz R, Frommeyer G, Smarsly W. Microstructures and properties of high melting point intermetallic titanium-silicon (Ti5Si3 and TiSi2) compounds. Materials Science & Engineering, A: Structural Materials: Properties, Microstructure and Processing A152 (1992) 288.

[7] Frommeyer G, Rosenkranz R, Luedecke C. Microstructure and properties of the refractory intermetallic titanium-silicon (Ti5Si3) compound and the unidirectionally solidified eutectic titanium - titanium silicide (Ti5Si3) alloy. Zeitschrift fuer Metallkunde 81 (1990) 307.

[8] Thom AJ, Kim Y, Akinc M. Effect of processing on oxidation of titanium silicide (Ti5Si3). Materials Research Society Symposium Proceedings 288 (1993) 1037.

[9] Thom AJ, Meyer MK, Williams JJ, et al. Improved oxidation resistance of A5Si3 (A=transition metal) silicides by small atom doping. Processing and Fabrication of Advanced Materials IV, Proceedings of a Symposium, 4th, Cleveland, Oct. 29-Nov. 2, 1995 (1996) 139.

[10] Kim Y, Thom AJ, Akinc M. Synthesis, processing and properties of titanium silicide (Ti5Si3). Process. Fabr. Adv. Mater. High Temp. Appl.--II, Proc. Symp. Mater Week '92 (1993) 189.

[11] Abba A, Galerie A, Caillet M. High-temperature oxidation of titanium silicide coatings on titanium. Oxidation of Metals 17 (1982) 43.

[12] Taniguchi S, Minamida T, Shibata T. Oxidation behavior of Ti5Si3 at temperatures between 1400 and 1700 K. Materials Science Forum 251-254 (1997) 227.

[13] Williams JJ, Akinc M. Oxidation Resistance of Ti5Si3 and Ti5Si3Zx at 1000 DegC (Z = C, N, or O). Oxidation of Metals 58 (2002) 57.

[14] Radhakrishnan R, Williams J, Kramer M, et al. Comparison of the sintering behavior of SHS and arc melted Ti5Si3. Ceramic Engineering and Science Proceedings 19 (1998) 381.

[15] Thom AJ, Akinc M. Interstitial chemistry effects on sintering of Ti5Si3. Ceramic Engineering and Science Proceedings 18 (1997) 57.

[16] Thom AJ, Akinc M. Effect of ternary additions on the oxidation resistance of Ti5Si3. Advanced Ceramics for Structural and Tribological Applications, Proceedings of the International Symposium on Advanced Ceramics for Structural and Tribological Applications, Vancouver, B. C., Aug. 20-24, 1995 (1995) 619.

[17] Melsheimer S, Fietzek M, Kolarik V, et al. Oxidation of the intermetallics MoSi2 and TiSi2-a comparison. Oxidation of Metals 47 (1997) 139.

[18] Wakelkamp W. Diffusion and Phase Relationship in the SystemsTi-Si-C and Ti-Si-N. Eindhoven: Eindhoven University of Technology, 1991.

[19] Goldstein JI, Choi SK, Van Loo FJJ, et al. Solid-state reactions and phase relations in the Ti-Si-O system at 1373 K. Journal of the American Ceramic Society 78 (1995) 313.

[20] Williams JJ, Kramer MJ, Akinc M, et al. Effects of interstitial additions on the structure of Ti5Si3. Journal of Materials Research 15 (2000) 1773.

[21] Thom AJ, Young VG, Akinc M. Lattice trends in Ti5Si3Zx (Z = B, C, N, O and $0 < x < 1$). Journal of Alloys and Compounds 296 (2000) 59.

Chapter 4. Characterization and Oxidation Behavior of Silicide Coating on Multiphase Mo-Si-B Composites

Zhihong Tang, Andrew J. Thom, Matthew J. Kramer and Mufit Akinc

A paper to be submitted to *Intermetallics*

Abstract

Mo_{ss}-based Mo-Si-B multiphase alloys possess improved fracture toughness compared to its single-phase silicide counterparts ($MoSi_2$, Mo_5Si_3 or T2) without sacrificing high temperature strength, but they degrade rapidly in an oxidizing environment at elevated temperature. In the present study, $MoSi_2$ coating was applied to protect Mo_{ss}-based alloy from high temperature oxidation via pack cementation. Boron-modified $MoSi_2$ coating was also produced in an attempt to enhance the oxidation resistance of $MoSi_2$ coating via co-deposition of B and Si, using a two-step process. Isothermal and cyclic oxidation tests on coated Mo-4.3Si-1.1B alloy were performed at 1100ºC and 1600ºC, respectively up to 200 hours. The $MoSi_2$ coating provide enough protection from oxidation in both static and cyclic condition at 1100ºC, while it degraded after ten hours by forming T1 ($Mo_5Si_3B_x$) phase at 1600ºC via inter-diffusion between coating and substrate. The coating lifetime of $MoSi_2$ was limited by the Si depletion by diffusing into substrate. The Additions of boron into $MoSi_2$ did not enhance the oxidation resistance as boride phases (MoB or Mo_2B_5) do not slow the diffusion of Si to substrate to stabilize $MoSi_2$ or Mo_5Si_3.

Keyword: A. Molybdenum silicides; A. multiphase intermetallics; B. oxidation; B. diffusion; C. Coating; E. phase stability

Introduction

Nickel and cobalt-based superalloy materials, currently employed in the production of military and industrial jet engine, have reach their maximum temperature limitation with operating temperatures greater than 90% of their melting temperature and will not be able to meet the temperature requirement of advance turbine engines. Over the past decade, considerable research has been focused on developing materials that can withstand oxidizing environments for potential service at temperature above 1000ºC. Among these alloys, Ni_3Al and γ-TiAl are two intermetallics showing promise for industry-scale success as they exhibited significant room temperature ductility compared to other intermetallics. Although the properties of alloys based on Ni_3Al approach those of established superalloys, the Ni_3Al alloys are unlikely to displace superalloys in aircraft engine applications [1]. Several γ-TiAl alloys are advancing toward a broad spectrum of applications in advanced aircraft turbine engine because of their low density yet their current temperature capability is less than 700ºC while prospects for 900ºC operating temperatures are doubtful [2, 3]. Refractory metallic systems based on molybdenum and niobium are attractive in terms of strength and melting temperatures, but a major barrier to use Mo and Nb-based alloys for high temperature application is their catastrophic degradation in oxidizing environments. Refractory silicides have the potential of meeting high temperature requirements such as creep strength, cyclic fatigue, toughness and ultimate tensile strength [4-6]. For instance, $MoSi_2$ is widely used as heating elements in electrical furnace up to 1800ºC due to its excellent oxidation resistance at elevated temperature by forming a protective silica glass layer. However, low creep strength at T > 1000ºC, pest oxidation at moderate temperatures (below 900ºC), and poor room temperature fracture toughness on the order of 3 MPa $m^{1/2}$ are severe limitations and are

subject to significant research efforts to overcome these limitations [7, 8]. Multiphase intermetallics based on Mo-Si-B compositions may present unique opportunities to overcome limitations of other materials mentioned above.

As shown in the schematic Mo-Si-B phase diagram [9](Fig.37), two specific alloy systems have received considerable interests from the scientific community for high temperature applications. The first one, which was pioneered by Akinc and his co-workers [10-14], consists of three intermetallics alloys, Mo_5Si_3, the T2 phase Mo_5SiB_2 and the A15 phase Mo_3Si. They exhibit excellent oxidation resistance and creep strength up to 1600ºC. The boron addition is critical for providing the observed oxidation resistance due to formation of low viscosity borosilicate glass layer that flows and seals the porous scale. However, these alloys also have low fracture toughness, and the thermal expansion anisotropy of the T1 phase make these alloys susceptible to thermal stress induced microcracking[15]. These deficiencies in mechanical behavior can be improved by moving towards the Mo-rich portion of the system[16-24]. The second alloys, incorporates the bcc-Mo phase to impart some ductility and fracture toughness to a three-phase microstructure containing Mo_3Si and Mo_5SiB_2 (T2) along with Mo_{ss}. The Mo_{ss} phase can improve the room and high temperature fracture toughness significantly depending on its volume fraction and its distribution [9, 18]. However it presents a challenge in achieving adequate oxidation resistance as $Mo_5Si_3B_x$–based alloys do. The oxidation resistant phase of these alloys is believed to be T2 phase (Mo_5SiB_2) yet, its high boron content results in a borosilicate glass with a much low viscosity than that formed with the T1 phase ($Mo_5Si_3B_x$) leading to excessive volatility of MoO_3 through the scale, contributing to unacceptable metal recession rates above about 1300°C [25, 26]. Schneibel et al. [27] explored designing a bcc-Mo

containing composite to balance acceptable oxidation resistance with adequate mechanical behavior with limited success.

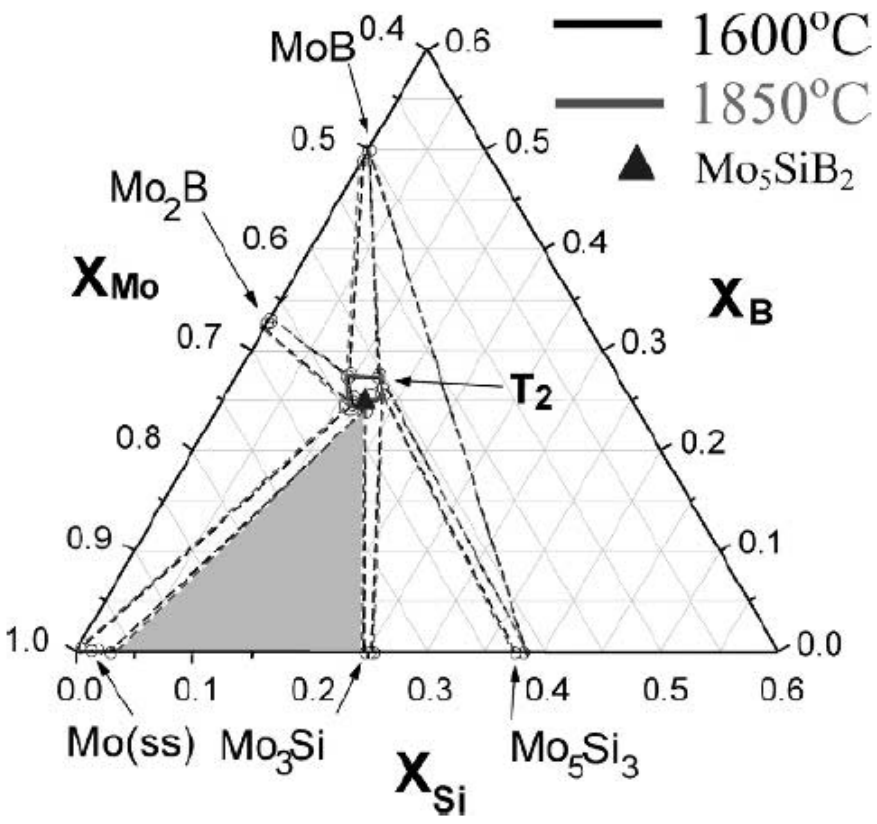

Figure 37 Schematic illustration of the Mo-rich section of the ternary Mo-Si-B phase diagram (~1600-1800ºC).

An emerging consensus is to protect the Mo_{ss}-based alloys with an oxidation resistant coating [28, 29]. One approach for developing an oxidation resistant coating is to deposit a silicon-rich phase, such as the $MoSi_2$ or T1-based alloy, onto the surface of the component. The halide activated pack cementation (HAPC) process has been successfully employed to deposit $MoSi_2$ onto a two-phase T2/Mo(ss) eutectic alloy by Ito et al.[29], and Mo-3Si-1B alloy by Sakidja et al. [30]. Although the steady-state oxidation rate of the coated alloy was nearly equal to that of $MoSi_2$ for up to 50 hours at 1300°-1500°C, the $MoSi_2$ layer was

partially transformed to T1 phase, and the long term effect of this microstructural change on the oxidation resistance of the coating was not investigated.

The present work investigates the feasibility of using the HAPC process to form oxidation resistant diffusion coatings on the Mo_{ss}-based Mo-4.3Si-1.1B (wt.%) alloy. Coating process development, oxidation performance and interdiffusion behavior of the coated alloy will be discussed.

Experimental procedure

Alloy Preparation

The nominal composition of the substrate alloy selected for this study is Mo-4.3 wt.%Si-1.1wt.%B (all compositions are in weight percent unless stated otherwise). These ternary alloys contain Mo_3Si, Mo_5SiB_2 (T2) and α-Mo (Mo solid solution), and were fabricated by either drop-casting or sintering powder compacts. The starting materials for drop-cast alloys included 99.7 % molybdenum pellets, 99.5 % Boron pieces (both from Alfa AESAR, Ward Hill, MA), and 99.99 % silicon lump (Alpha Chemicals, Danvers, MA). The alloy was produced in the form of rod by arc-melting the starting materials on a copper hearth with a tungsten electrode. To ensure homogenization, the alloy was remelted at least three times and then annealed at 1900ºC for 2 hours in a flowing argon atmosphere.

The Mo-4.3%Si-1.1%B alloy powder from Exotherm Corp (Camden, NJ) was used to produce sintered alloy. Powder was milled and sieved through a 635-mesh screen with a nominal opening of 20μm, and uniaxially pressed into a 9.5mm diameter pellet using stearic acid as a lubricant. The pellets were heated in Ar in a tube furnace to 1000ºC to remove the stearic acid before sintering at 1900ºC for 2 hrs in flowing Ar atmosphere. Both drop-cast and sintered alloys were cut into small coupons and polished with 600-grit SiC paper, then

ultrasonically cleaned in acetone and ethanol. The edges were rounded in order to minimize the cracking.

Pack cementation process

The halide-activated pack cementation process was employed to deposit silicon and/or boron onto the substrate samples. The components in pack cementation include: the masteralloy (i.e. a powder of the element or elements to be deposited on the surface of the parts, such as Si and/or B), a halide activator (e.g. NaF), and an inert filler powder (e.g. Al_2O_3). Three kinds of pack cementation processes were employed in this study: i) Si deposition only, ii) co-deposition of Si and B, and iii) two-step boronizing and siliconizing. The pack components and process parameters are shown in Table 6. The coupons to be coated were measured, weighed and loaded into an Al_2O_3 crucible with pack mixture. The crucible was sealed with an Al_2O_3 lid using an Al_2O_3-based cement. The sealed crucible was then inserted into an alumina tube in a horizontal tube furnace with a flowing argon atmosphere (80 mL/min). After the inert atmosphere had been established, the packs were preheated to 250ºC for two hours to remove any residual moisture. The deposition process was carried out at 900ºC or 1000ºC for various times. After pack cementation, the sample was cooled to room temperature at 2ºC/min and the coupons removed from the pack, washed in hot water and ultrasonically cleaned in acetone to remove any salt condensate or loosely embedded pack powder. Pack-cemented samples were annealed in flowing Ar atmosphere at 1600ºC to test the thermal stability of the coating.

Oxidation test

Isothermal oxidation tests on coated samples were conducted in a tube furnace in flowing dry air at 1100ºC or 1600ºC up to 400 hours. Thermal cycling exposure was also

carried out in air at 1100ºC. The thermal cycle consists of heating to 1100ºC at 20ºC/min, holding for 24 hours and cooling in 5 min to room temperature. Mass change was continuously recorded after every cycle

Table 6 Compositions of pack mixture (wt.%) and processing conditions

No.	Pack mixture			Temperature, ºC	Time, hrs
	Master alloy	NaF Activator	Al_2O_3 Filler		
1	10% Si	2%	Balance	1000	48
2	10% B	2%	Balance	900	100
3	9%Si, 1%B	2%	balance	1000	48
4	10%Si, 2%B	2%	balance	1000	48
5	5%Si, 5%B	2%	balance	1000	48

Characterization

The as-deposited, annealed and oxidized samples were examined by X-ray diffraction (XRD, Scintag XDS 2000, Cupertino, CA) to identify the phases formed. Microstructural features of the surface and cross-section of the samples were examined by scanning electron microscopy using backscattered electron imaging (SEM/BSE, JEOL, JSM 6100, Peabody, MA) and energy dispersive spectroscopy (EDS, Oxford Instruments, Valley, CA).

Results and Discussion

Silicide coating

Fig.38a shows a typical cross-section of the silicide coating formed on sintered alloy 3 (Mo-4.3Si-1.1B) coupon after 48 hours pack cementation at 1000ºC in an Si pack (#1 in Table 6). The EDS and XRD analysis confirmed that the coating was $MoSi_2$ with the $C11_b$

structure. A uniform coating layer about 40μm in thickness formed on the substrate. At least 10 measurements were taken and the average thickness of $MoSi_2$ layer was determined. Growth of $MoSi_2$ layer was found to be parabolic with respect to deposition time with a corresponding rate constant of $8\times10^{-11}cm^2/s$ at 1000ºC. This value compares very well with the intrinsic parabolic growth rate constant of $MoSi_2$ obtained from Si/Mo diffusion couple (3.91×10^{-10} cm^2/s) [31]. The inward-diffusion of silicon is thought to be the rate-controlling step. None of the Mo_5Si_3, Mo_3Si or T2 (Mo_5SiB_2) phases were detected between the $MoSi_2$ layer and the substrate. This result is in agreement with the kinetic studies of Mo/Si diffusion couple as well, [31] that the intrinsic growth rates of Mo_5Si_3 and Mo_3Si are slower than that of $MoSi_2$ about two or three orders of magnitude at 1000ºC. It should be noted the $MoSi_2$ coating of the as-deposited alloy was always cracked at the corners and edges of the substrate, and the perpendicular microcracks were extending to the surface were also observed (see Fig38a).

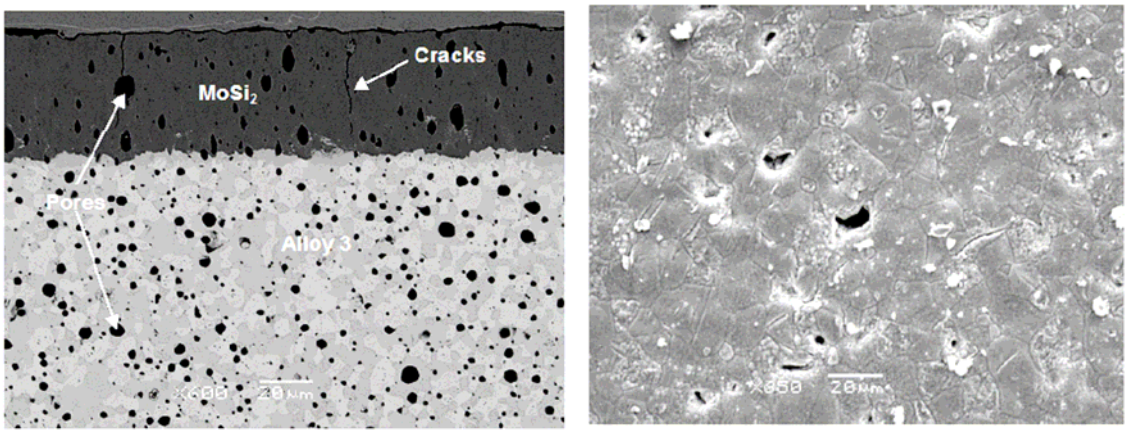

Figure 38 Micrographs of silicide coating growing on sintered Mo-4.3Si-1.1B alloy by a NaF activated pack (#1 in table 6): (a) cross-sectional image, (b) surface morphology

Fig.38b shows the surface morphology of a $MoSi_2$ coating grown on a sintered alloy 3. The grain size in the coating ranged from several microns to about 30 microns. Pores are visible on the surface of the coating, and the small surface protrusions are Al_2O_3 and salt particles as evidenced by EDS analysis. These particles were adherent to coating, and could not be removed by either rinsing in hot water or ultrasonic cleaning in acetone and ethanol. It is worth noting that these particles were not observed below the surface or at the interface between coating and substrate.

The oxidation behavior of the coating was assessed by measuring the weight change as a function of exposure time. Fig.39 show that the weight gain data at 1100ºC for pack cemented alloy. Only a slight weight loss of about 0.2 mg/cm^2 was observed after oxidation at 1100ºC for 200 hrs. Even after 8 cycles (total 192 hours), weight loss was less than 0.5 mg/cm^2, suggesting that the micorcracks formed by pack cementation process was sealed by silica glass and had no obvious detrimental effect on the oxidation behavior of $MoSi_2$ coating during exposure to air at 1100ºC. For comparison, Mandal et. al.[32] reported the uncoated Mo-4.3%Si-1.1%B alloy suffered a significant weight loss of more than –60 mg/cm^2 at 1100ºC for 200 hrs, suggesting a loss of volatile MoO_3. Clearly, $MoSi_2$ coating significantly suppressed the rapid oxidation of alloy 3. The cross-section of oxidized alloy is shown in Fig.40a. No significant oxidation was observed in the coating or substrate. Only a thin silica glass formed at the surface. A very thin Mo_5Si_3 layer was observed between the silica scale and $MoSi_2$ coating due to selective oxidation of Si. In addition, a Mo_5Si_3 layer below the $MoSi_2$ coating less than 20μm thick was observed as a result of interdiffusion between coating and substrate.

Oxidation in air at 1600ºC for two hours results in a small weight loss of about -0.1 mg/cm^2, but significant changes in the microstructure (see Fig.40b). The microstructure of the coating depicts three layers: i) an outer layer about 25µm in thickness comprising mixed $MoSi_2$/T1 phases, ii) an intermediate layer about 50µm in thickness containing single T1 phase, and iii) a 10µm thick interlayer consisting of MoB and T2 phases. The cracks that penetrated through the outer $MoSi_2$ layer were arrested at the intermediate T1 layer and sealed by the silica glass.

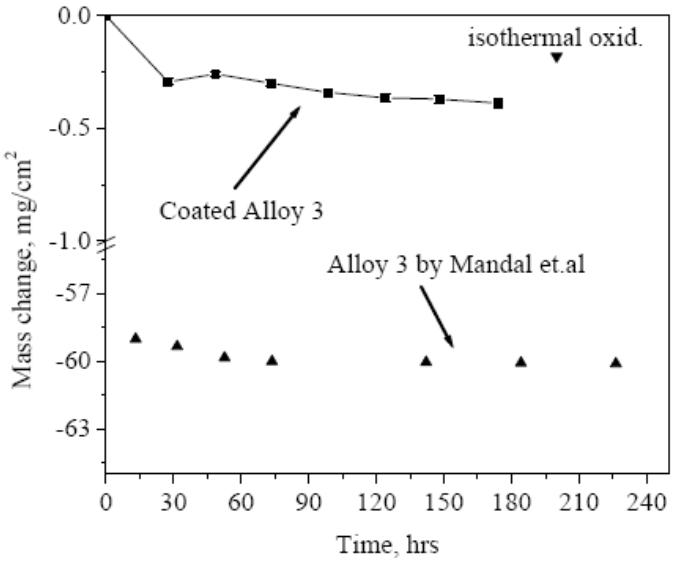

Figure 39 Mass change of a pack cemented Mo-4.3Si-1.1B alloy after isothermal and cyclic oxidation at 1100ºC in dry air. For comparison, the mass change of uncoated Mo-4.3Si-1.1B alloy reported by Mandal et. Al [32] at 1100ºC was also included in this plot.

Although the transformation rate from $MoSi_2$ to T1 layer was not experimentally determined, annealing of the sample in Ar confirmed that the transformation of a $MoSi_2$ coating, like that shown in Fig.37a, is less than 12hrs at 1600ºC. Once $MoSi_2$ layer is

completely transformed to T1, the coating oxidized rapidly since the T1 and MoB/T2 multilayer structure do not form a protective silica layer. In fact, the coated alloy was completely oxidized after exposure to air at 1600ºC for 50 hours.

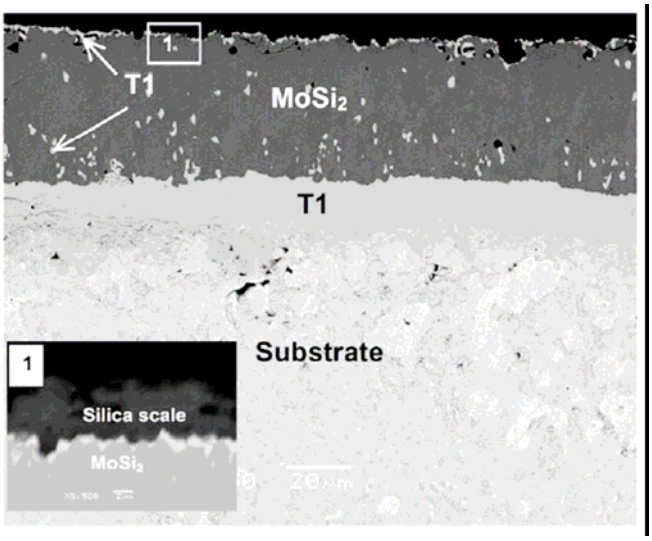

(a)

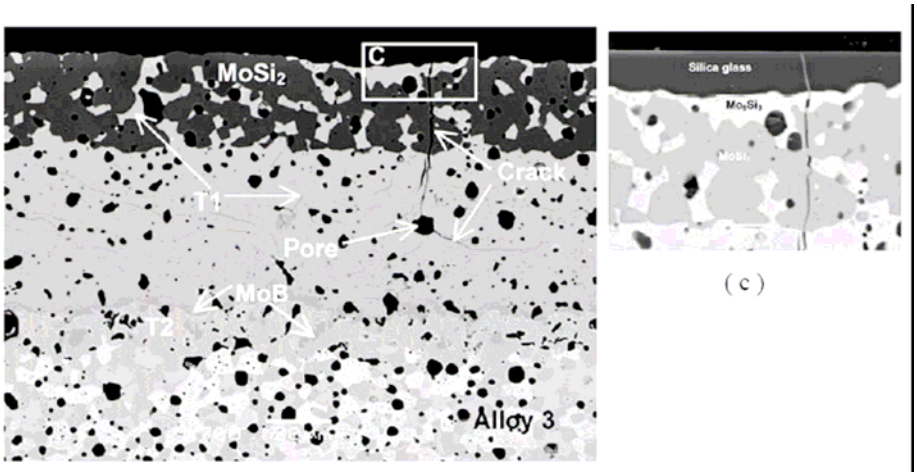

(c)

(b)

Figure 40 Micrographs showing cross-section of silicide coating growing on sintered Mo-4.3Si-1.1B alloy by a NaF-activated pack (#1 in table 6) after isothermal oxidization in dry air: (a) at 1100ºC for 200hrs, (b) at 1600ºC for 2 hours.

Borosilicide coating

The rapid loss of the $MoSi_2$ coating is a result of preferential silicon diffusion into substrate which leads to the growth of T1 layer. Since the oxidation behavior of T1-based phase is strongly dependent on boron content, undoped T1 (i.e., Mo_5Si_3) exhibits catastrophic mass loss above 1000ºC due to formation of a porous oxide scale. A small amount of boron added to Mo_5Si_3 results in a non-porous, protective scale. The B addition allows viscous flow to close submicron scale porosity. Meyer and Akinc [14] studied the isothermal oxidation of several B-doped Mo_5Si_3 alloys around Mo_5Si_3 phase field at 1450ºC and concluded that a minimum boron content is somewhere between 0.14 wt.% and 0.91 wt.% required in order to form a protective scale on Mo_5Si_3-based materials. This boron level is definitely exceeds the solubility of B in Mo_5Si_3. Indeed, the oxidation resistant Mo_5Si_3-based alloys studied to date were always multiphase containing at least a small amount of $MoSi_2$, T2 or MoB phases. Therefore, the boron-modified silicide diffusion coatings were developed via pack cementation in order to address the poor oxidation behavior of T1 interlayer. Two approaches were employed: co-deposition of B and Si onto alloy 3 and sequential deposition of B followed by Si.

Co-deposition of B and Si

The SEM micrograph in Fig.41a shows the cross-section of a multilayered borosilicide coating formed on sintered Mo-4.3Si-1.1B alloy after 48 hours co-deposition of Si and B in a pack with Si/B=9 (#3) at 1000ºC. Instead of single $MoSi_2$ layer observed in silicon only coating, the co-deposited coating consists of three layers: i) an 20μm thick $MoSi_2$ outer layer, ii) a 30μm thick intermediate layer consisting of MoB needles and

particles in a $MoSi_2$ matrix. The presence of MoB was confirmed by XRD by carefully polishing away the top $MoSi_2$ layer, iii) a 10μm thick inner layer containing mostly T2 (Mo_5SiB_2) phase with dispersed MoB particles. Thus, MoB phase was successfully incorporated into the coating by incorporating B in the pack mixture. The distribution of boron in the coating suggested that diffusion of B in $MoSi_2$ layer is much faster than Si.

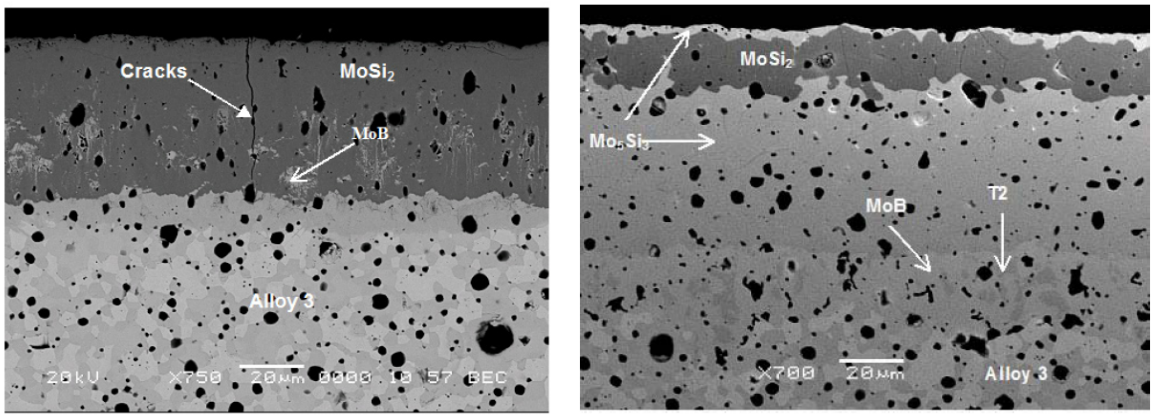

(a) (b)

Figure 41 SEM micrographs of B-modified silicide coating on sintered Mo-4.3Si-1.1B alloy produced by co-deposition of B and Si (#3 in table 6): (a) as-deposited, (b) after isothermal oxidation in dry air at 1600ºC for 2 hours.

The amount of boride in the coating can be controlled via changing the B/Si ratio in the pack mixture. Fig.42 shows that co-deposited coating on drop-cast Mo-4.3Si-1.1B by pack cementation with various B/Si ratios (#3-5). With the increasing B/Si ratio in the pack mixture, both the amount of MoB phase in the $MoSi_2$ layer and thickness of $MoSi_2$/MoB inner layer increase. Mo_2B_5 begins to appear with increasing boron content. For example, the XRD phase showed Mo_2B_5 phase in the B/Si = 1 pack. It should be noted that in addition to the boride phases, pores were formed with porosity increasing with the increasing B/Si ratio in the pack. The increase in the porosity can be explained by the following displace reaction:

$$MoSi_2 + B \rightarrow MoB + 2Si \qquad (1)$$

The $MoSi_2$ phase is reduced to MoB due to boron's higher diffusivity. This, in turn, releases silicon atoms, which diffuse into the substrate. The reaction is accompanied by a substantial volume reduction because the molar volume of the $MoSi_2$ phase (24.1cm^3/mol) is nearly twice than that of the MoB phase (12.3cm^3/mol).

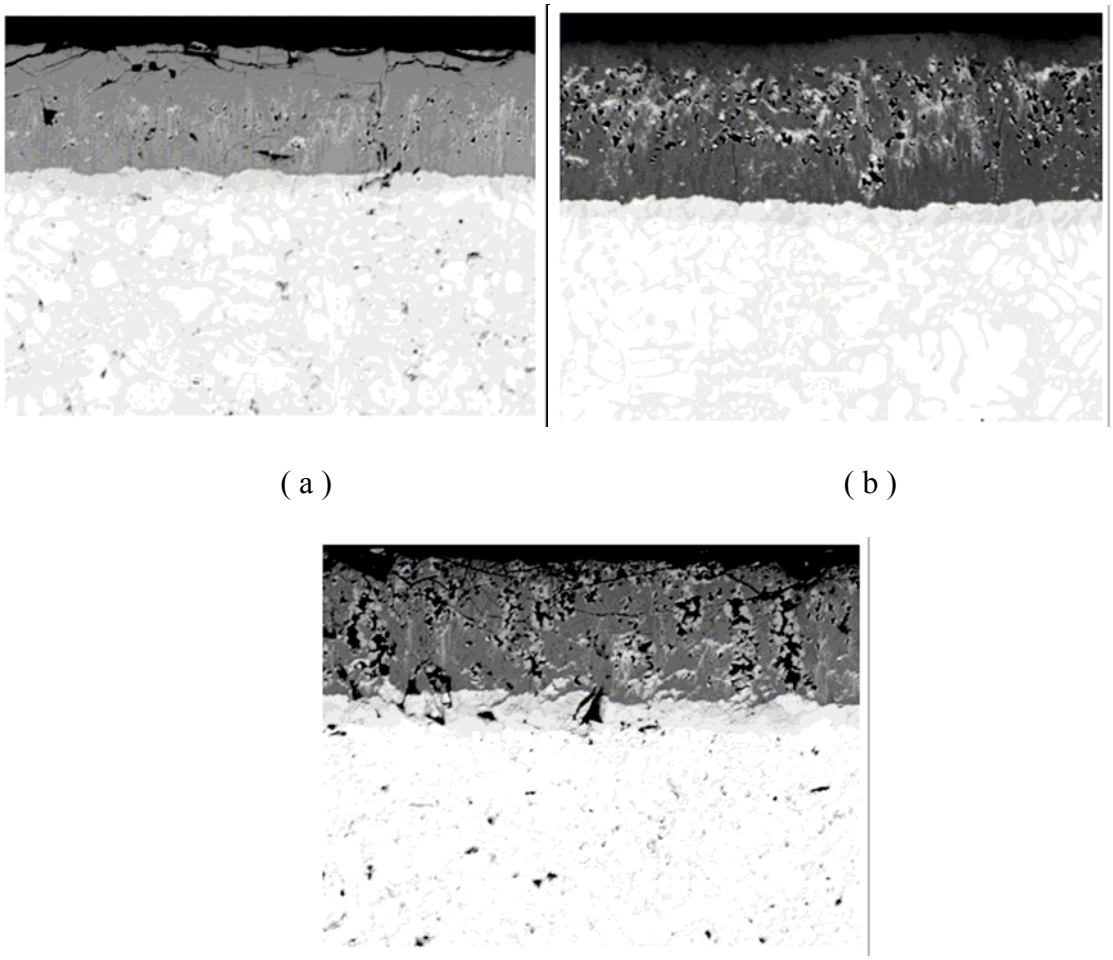

(a) (b)

(c)

Figure 42 SEM micrographs of cast Mo-4.3Si-1.1B alloy pack cemented in pack mixture with Si/B ratio of: (a). 9/1(pack #3 in table 6), b). 5/1 (pack #4), c). 1/1(pack #5).

Both short-time and long-time isothermal oxidation tests were run on the co-deposited samples. A weight loss of less than –0.1 mg/cm^2 was observed after oxidation at 1600ºC for two hours in air, while the sample is totally oxidized after 50 hrs exposure. Fig.41.b shows back-scattered electron (BSE) images of co-deposited alloy after short-time oxidation. No obvious oxygen attack into substrate through cracks was observed, which indicated that cracks were sealed by borosilicate glass and were not the cause of the long-time oxidation failure. The $MoSi_2$ coating was partially transformed into T1 phase and an interlayer consisting of MoB particles-dispersed T2 matrix with was observed. The interlayer has the same phase constitutions (T2+MoB) as that in Si only coating. It is thicker (25μm vs. 15μm) perhaps in part due to the incorporation of boride phases into $MoSi_2$ coating. According the Mo-Si-B ternary phase diagram, MoB is can co-exist with $MoSi_2$ and Mo_5Si_3 phases. However, careful XRD and SEM analysis after removing the top layer showed no evidence of MoB phase in either $MoSi_2$ or Mo_5Si_3 phases, suggesting that MoB must have reacted with Si to form T1 as silicon diffuses into the substrate, as will be discussed later. The $MoSi_2$ layer was completely transformed into T1 phase after annealing at 1600ºC for twelve hours. It is presumed that poor oxidation resistance of Mo_5Si_3 layer formed by interdiffusion between the coating and substrate is responsible for the degradation.

Two-step B+Si coating

Fig.43 shows the micrographs of Mo-4.3Si-1.1B cast alloy after boronizing (pack #2). A complex two-layer diffusion microstructure was developed: a ~10μm thick outer Mo_2B_5 layer with dispersed MoB particles, a ~30μm thick network of T2 and MoB mixed inner layer, Apparently, MoB in T2/MoB inner layer formed from reaction of B with Mo phase in the substrate, and T2 evolved from reaction of B with Mo_3Si. Closer examination of the

interface between the coating/substrate by SEM/EDS revealed fine T2 particles, which were formed within the $MoSi_3$ phase near the interface. Dark spots observed in the inner T2 layer were identified as $MoSi_2$ phase by EDS. The formation of $MoSi_2$ could occur if Si concentration exceeds the solubility limit in T2 phases as B reacts with Mo_3Si to form T2 (Mo_5SiB_2).

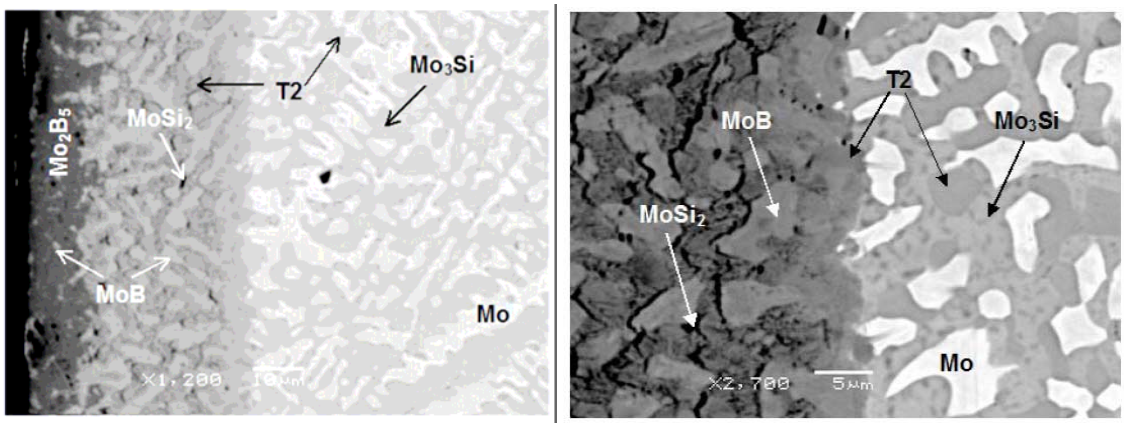

(a) (b)

Figure 43 SEM micrographs of cast Mo-4.3Si-1.1B alloy pack cemented in a B pack (#2): a). low magnification, b) high magnification at the interface

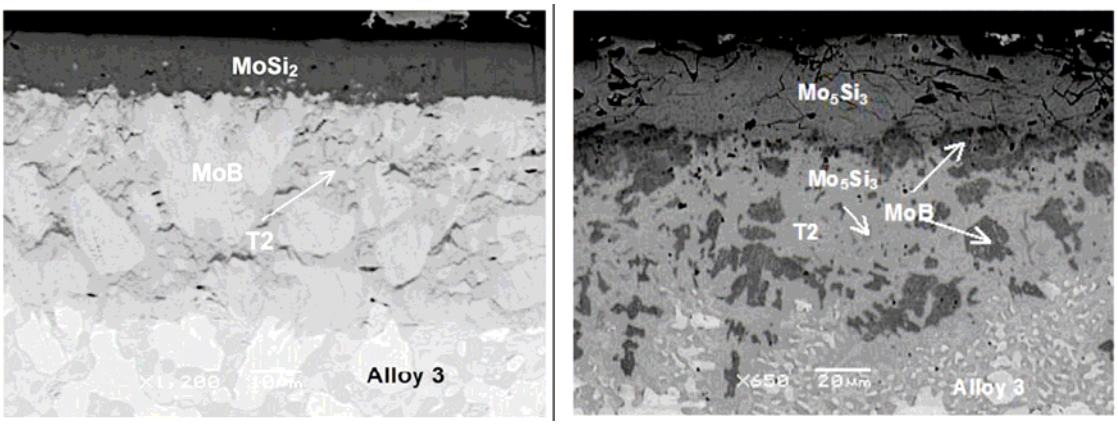

(a) (b)

Figure 44 SEM micrographs of cast Mo-4.3Si-1.1B alloy by boronizing in a B pack (#2) followed by siliconizing in a Si pack(#1): (a) as packed coating, (b) annealed at 1400ºC for 24 hours

Fig.44a shows the cross-sectional microstructure of as-prepared and annealed two-step coating (B+Si). After two step pack cementation (boronizing and siliconizing), Mo_2B_5 top layer formed is totally converted into $MoSi_2$ and a ~12μm thick $MoSi_2$ layer is formed. A 40μm thick T2+MoB intermediate layer is observed between $MoSi_2$ and substrate. The thickness of this intermediate layer is similar to that of B-packed alloy 3 (Fig.43). It implies that when Mo_2B_5/MoB transformed into $MoSi_2$ by Si cementation followed by B diffuse through $MoSi_2$ since the solubility of boron in $MoSi_2$ is negligible.

After annealing at 1400ºC for 24 hours, the $MoSi_2$ phase is completely transformed into T1, and the T2 fraction in the T2/MoB layer increased. Unlike the as-packed coating in which the T2/MoB interlayer consists of MoB matrix with interconnected T2 phase, the interlayer in the annealed coating consists of T2 matrix with isolated MoB grains. Some Mo_5Si_3 particles were also observed in the T2 phases.

Evaluation of silicide and borosilicide coating

The excellent high temperature strength and oxidation resistance qualify $MoSi_2$ as protective coating for Mo-based alloys. Similar studies by Ito et al.[29, 33] on Mo-9Si-18B (at.%) alloy and Sakidja et al.[30] on Mo-14.2Si-9.6B at.% alloy revealed. Two significant challenges for future high temperature application still remain: i) thermal stresses generated by coefficient of thermal expansion (CTE) mismatch at the coating-substrate or coating-oxide interface, and the large CTE anisotropy of T1 may induce cracks during process. Although these cracks may be sealed by silica (or borosilicate) glass at high temperature, it may still cause degradation of coating under thermal cycling, ii) the rapid diffusion of Si

from $MoSi_2$ coating results in the formation of the T1 phase which does not provide oxidation protection for the substrate.

Thermal stress

$MoSi_2$ is goes through ductile-to-brittle transition at approximately 1000ºC. Thermal stress resulting from the CTE mismatch between the $MoSi_2$ coating and substrate can cause cracks in the coating if they reach or exceed a critical value, i.e., the strength of $MoSi_2$. Since the tensile strength of $MoSi_2$ is much lower than its compressive strength (275 MPa vs. more than 1378 MPa)[34], tensile stresses are particularly damaging and will promote transverse microcracking in the coating, as observed in this study.

The thermally induced stresses on cooling can be approximated calculated using the following equation[35]:

$$\sigma_{therm} = \frac{E_c \Delta T(\alpha_s - \alpha_c)}{\frac{E_c}{E_s}\frac{d_c}{d_s}(1-\upsilon_s)+(1-\upsilon_c)} \qquad (2)$$

Where α is (CTE), v is Poisson's ratio, ΔT is the temperature difference, d is the thickness, and subscripts c and s refer to coating and substrate, respectively. Since $d_c << d_s$, the above equation can be simplified as:

$$\sigma_{therm} = \frac{E_c \Delta T(\alpha_s - \alpha_c)}{(1-\upsilon_c)} \qquad (3)$$

Using the bulk CTE as listed in Table 7 and ΔT=975ºC (cooling the sample to room temperature from 1000ºC), the thermal stresses developed in the $MoSi_2$ coating are 1041, 709 and 520MPa with substrates Mo, Mo_3Si and Mo_5SiB_2, respectively. These stresses definitely exceed the tensile strength of $MoSi_2$ (275MPa). As shown Fig.38a and Fig.41a, the transverse microcracking was observed in the as-packed $MoSi_2$ coating no matter how slowly

they were cooled. Fortunately, the present oxidation experiments showed that no significant oxidation through cracks (Δm<-1mg/cm^2) occurred since the silicate glass formed by oxidation may have sealed them. Similar results were also reported by Ito et.al.[29]. They indicated the presence of microcracks in the as-deposited $MoSi_2$ coating on T2/Mo_{ss} substrate; however, steady-state weight gain with mass gain of less than 2mg/cm^2 was observed after 50 hours oxidation at 1500ºC. It should be noted that the $MoSi_2$ were not completely transformed into T1 phases after 50 hours exposure in Ito's experiments, which provide the reservoir of Si for the formation of continuous silicate glass.

Table 7 Calculated thermal stress of $MoSi_2$ coating on various substrates

Materials	CTE, 10^{-6}/K			E, GPa	ν	σ_{therm}, MPa	Ref.
	α_a	α_c	Bulk				
$MoSi_2$	7.99	9.69	8.56	432	0.15	-	[15, 36, 37]
Mo_5SiB_2	7.72	7.20	7.55	383	0.24	520	[36, 38]
Mo_3Si	7.17	-	7.17	732	0.02	709	[15, 39]
Mo_5Si_3	5.2	11.5	7.3	323	0.278	644	[40]
MoB	8.38	6.38	7.71	-	-	441	[15]
Mo	6.5	-	6.5	323	0.293	1041	[40]

Note: CTE-coefficient of thermal expansion;
E-Young's modulus; ν- Poisson ratio;
σ_{therm}-calculated value thermal stress for an $MoSi_2$ coating on various substrates
$\alpha_{CTE}=(2\alpha_a+\alpha_c)/3$ based on the Reuss approximation of the bulk elastic modulus

Theoretically, the thermal stress caused by CTE mismatch can be reduced by addition of alloying elements to strengthen $MoSi_2$ coating. For example, Yoon et.al. [41] reported that tungsten-alloyed $MoSi_2$ coating exhibited 30% lower crack density. However, in practice,

specific dopants will need to be identified for the current Mo-Si-B system. Another method is to incorporate either low expansion second phases into the coating. Maloney et al. [42] reported that both SiC and Si_3N_4 phases were especially desirable as modifier for the reduction of CTE of $MoSi_2$ since both materials are chemically compatible with $MoSi_2$ and do not deteriorate the oxidation resistance of $MoSi_2$ coating. In present study, the crack density obviously decreased by forming a T2/MoB interlayer between $MoSi_2$ and substrate in two-step B-modified silicide coating (Fig.44a).

Thermodynamic stability

From the microstructural features, the diffusion paths for silicide and boron-modified silicide coatings on multiphase alloy 3 can be drawn on Mo-Si-B ternary phase diagram (Fig.45). A diffusion zone with Mo_5Si_3 (T1) and MoB+T1 two-phase layer was observed in both cases whether the coating contains boride phases or not. In order to understand the microstructural evolution of $MoSi_2$-based coating on three-phase substrate, the behavior of diffusion reactions in a simpler system like $MoSi_2$ vs. Mo, $MoSi_2$ vs. T2 were also evaluated. Several studies[43-46] on $MoSi_2$/Mo diffusion couple have been conducted by several groups, and it was generally concluded that the Mo_5Si_3 (T1) and Mo_3Si layers grew simultaneously with a parabolic rate law at the early annealing stage. The Mo_5Si_3 layer grows by decomposition reaction of Equation (4) and the diffusion reaction of Equation (5), and Si is the dominant diffusing element in Mo_5Si_3.

$$5MoSi_2 \rightarrow Mo_5Si_3 + 7Si_{Mo_5Si_3} \qquad (4)$$

$$12Mo + 7Si_{Mo_5Si_3} \rightarrow \frac{1}{4}Mo_3Si + \frac{9}{4}Mo_5Si_3 \qquad (5)$$

The apparent growth rate of Mo_3Si in $MoSi_2$/Mo diffusion couple does not represent the intrinsic growth rate since Mo_3Si is also consumed by the growth of Mo_5Si_3 layer. Yoon et al.[43] studied the intrinsic growth rate of Mo_3Si in the Mo_5Si_3/Mo diffusion couple, in which Mo_3Si is the only growing phase. The growth rate of Mo_5Si_3 layer is about two orders of magnitude higher than that of Mo_3Si at the temperature range of 1000 -1700ºC.

Hayashi et al.[47] studied the $MoSi_2$/Mo_5SiB_2 diffusion couple. Mo_5Si_3 (T1) and MoB+T1 two-phase layer formed in the diffusion zone. According to the ternary phase diagram, one may expect the formation of a single Mo_5Si_3 layer in the $MoSi_2$/T2 diffusion couple. However, if the amount of B atoms expelled, as T2 transformed to T1 ($Mo_5Si_3B_x$), exceeds the solubility of B in T2, then the MoB+T1 two-phase layer may form by the following reaction:

$$4Si + 5Mo_5SiB_2 \rightarrow 3Mo_5Si_3 + 10MoB \qquad (6)$$

In both $MoSi_2$/T2 and $MoSi_2$/Mo diffusion couples, the dominant diffusing element is Si.

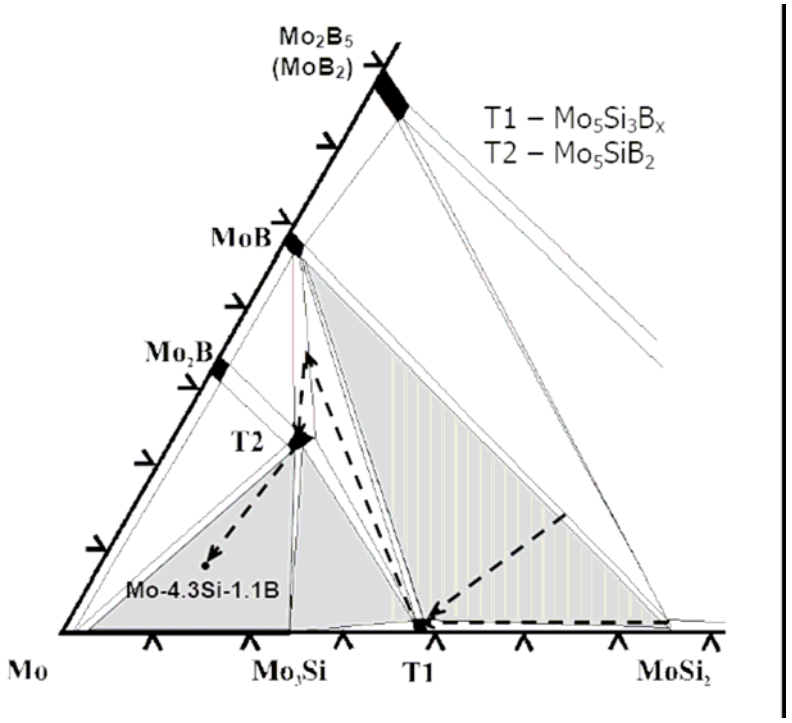

Figure 45 Schematic description of diffusion paths for both silicide coating and boron-modified silicide coating on Mo-4.3Si-1.1B alloy, indicated as dash line.

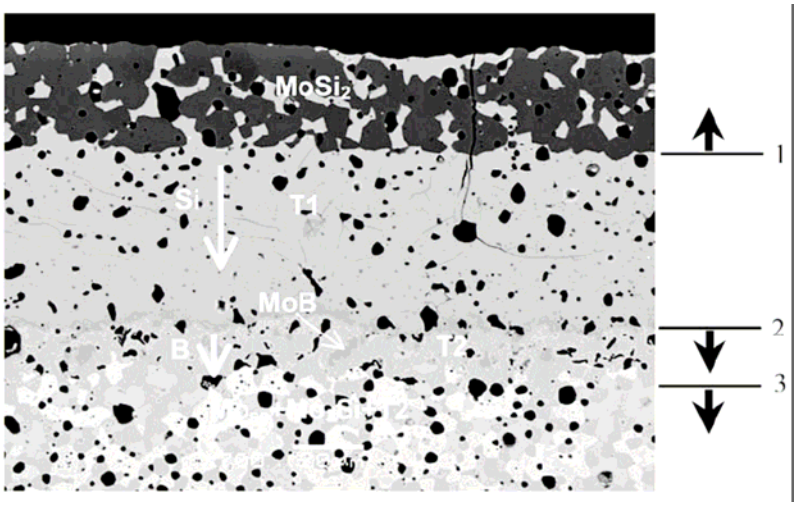

Figure 46 SEM micrograph and representation of diffusion path showing reaction between $MoSi_2$ coating and three-phase ($Mo+Mo_3Si+T2$) substrate. The diffusion direction of Si and B atoms and growth direction of interlayer were indicated by arrows.

For $MoSi_2$ coating on three-phase Mo-4.3Si-1.1B (Mo_{ss}+T2+Mo_3Si) alloy, the diffusion reaction is represented in Fig.46. $MoSi_2$ decomposes into T1 ($Mo_5Si_3B_x$) and Si by Equation (4) at interface 1 as in $MoSi_2$/Mo and $MoSi_2$/T2 diffusion couple. The interface 1 shifts toward $MoSi_2$ phase and the Si atoms diffuse through T1 to interface 2, at which additional T1 phase is formed by the following reactions:

$$3Si + 5MoB \rightarrow Mo_5Si_3B_x + (5-x)B \qquad (7)$$

$$2Si + Mo_5SiB_2 \rightarrow Mo_5Si_3B_x + (2-x)B \qquad (8)$$

Since solubility of boron in T1 phase is negligible, the excess boron atoms must diffuse toward interface 3 to form boron-rich phases such as: T2 and MoB since B has limited solubility in T2 phase. Therefore, the lifetime of silicide coating is limited by the growth rate of T1 layer, i.e. conversion of $MoSi_2$ into T1.

In B/Si co-deposition coating, the diffusion path did not change even though the composition of the coating moved up to the B-rich side along the tie line between MoB and $MoSi_2$ in the ternary Mo-Si-B phase diagram. MoB did not stabilize the $MoSi_2$ phase; rather it reacted with Si to form T1 phase and release B atoms. The excess B diffuses to coating/substrate interface to form borides by reacting with Mo and Mo_3Si.

For the $MoSi_2$-based coating, the lifetime is limited by the growth rate of T1 layer. Fig.47 shows the apparent growth rate of Mo_5Si_3 layer for $MoSi_2$/Mo diffusion couple. The data represents the intrinsic growth rate of Mo_5Si_3 layer. Although there is some scatter in the data in part due to difference in sample preparation, the values are on the same order magnitude. The apparent growth rates of Mo_5Si_3 layer in the $MoSi_2$/T2 diffusion couple and $MoSi_2$ coating on T2+Mo_{ss} are also included. The growth rates of Mo_5Si_3 in ternary Mo-Si-B

system are slightly lower than that of $MoSi_2$/Mo diffusion couple presumably due to the existence of T1+MoB two-phase layer.

The lifetime of $MoSi_2$ coating on three-phase Mo-Si-B alloy can be estimated by considering conversion rate of $MoSi_2$ to T1. Fig.48 shows that estimated lifetime as a function of exposure temperature assuming that the initial thickness of $MoSi_2$ layer is 100μm. The maximum and minimum lifetimes are calculated based highest and lowest data in growth rate of Mo_5Si_3 layer in Fig.47a. The coating can last more than 1000 hours with service temperature below 1300ºC, while it will lose protection less than hundred hours above 1500ºC due to rapid interdiffusion.

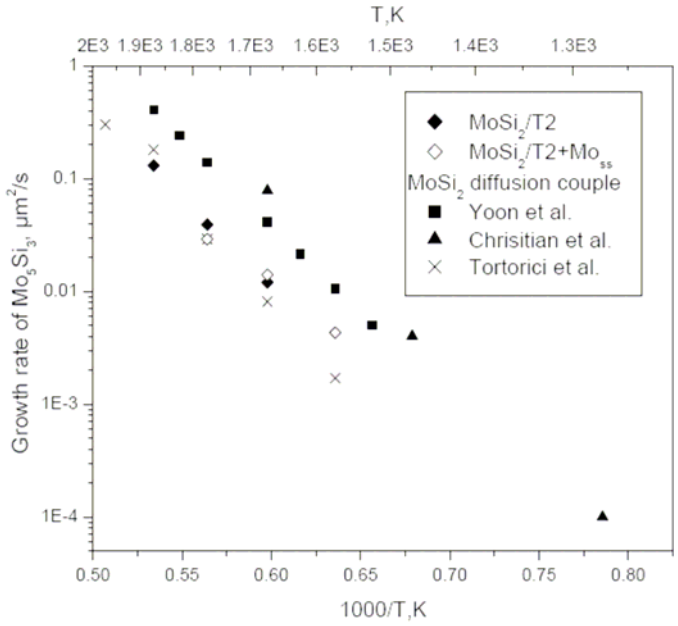

(a)

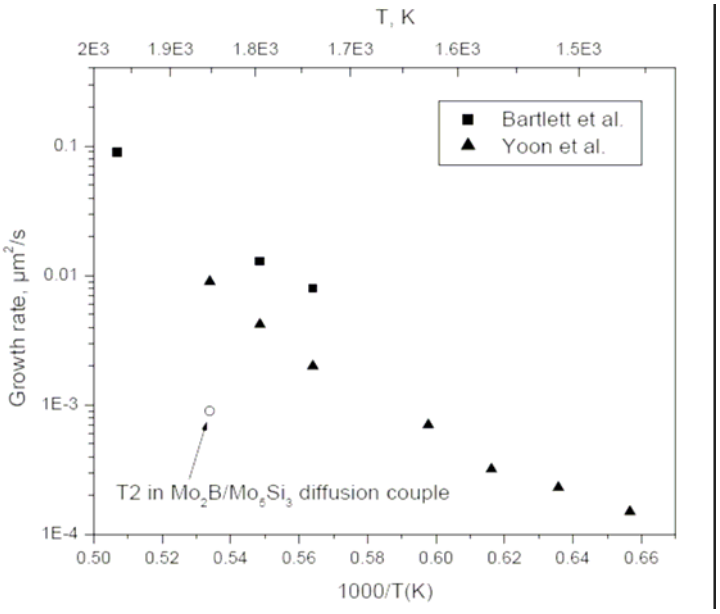

(b)

Figure 47 Arrhenius plot of parabolic growth rate as a function of the reciprocal temperature for a) Mo_5Si_3 and b) Mo_3Si.

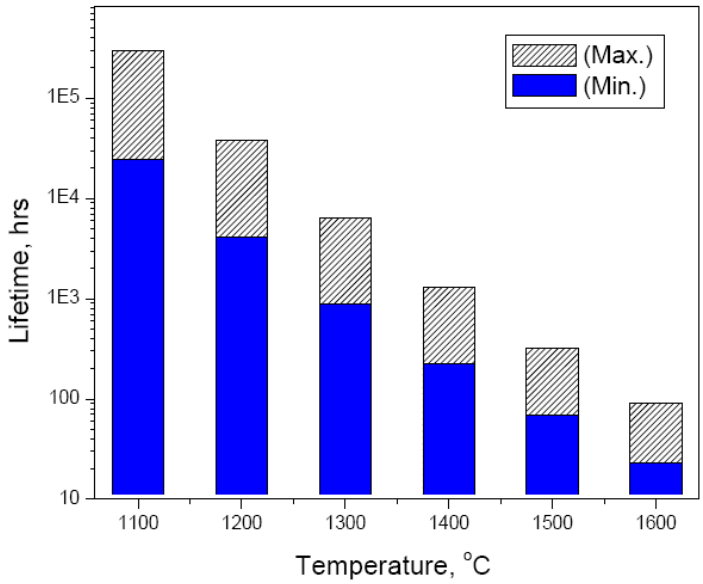

Figure 48 Estimated lifetime of $MoSi_2$-based coating on three-phase (Mo_{ss}+Mo_3Si+T2) alloy.

Strategies of extending lifetime coating

$MoSi_2$-based coating was impaired above 1300ºC by the formation of poor oxidation resistant Mo_5Si_3 interlayer due to rapid interdiffusion. No alloy has been identified as a diffusion barrier for $MoSi_2$/Mo couple. Addition of refractory alloying elements such as W and Nb can slow the growth rate of $(Mo,M)_5Si_3$ significantly[48], but not enough to last for several hundred hours above 1500ºC. Thus new coating design strategy needs to be considered.

Thom et al.[49, 50] reported that Mo-13.4Si-2.6B (T1+MoB+$MoSi_2$) and Mo-9.9Si-1.4B (T1+T2+Mo_3Si) alloys possess excellent oxidation resistance up to 1600ºC. Thus, if the coating composition was shifted to Mo-rich regions, such as T1+T2+Mo_3Si three phase region, the Si diffusion inward will result in the formation of Mo_3Si or T2 interlayer instead of T1 according to Mo-Si-B ternary phase diagram. The intrinsic growth rate of Mo_3Si phase

is about at least one order of magnitude lower than that of Mo_5Si_3 at the temperature of 1000-1700ºC as shown in Fig.47, And This can reduce the depletion rate of Si from silicide coating, therefore extend the lifttime of coating.

Conclusions

$MoSi_2$-based slilicide diffusion coating was successfully deposited onto Mo_{ss}-based multiphase Mo-Si-B alloy via pack cementation, the coating process, oxidation behavior and interdiffusion behavior were investigated, and the results obtained are summarized as follows:

1. In the pack siliconizing coating, a $MoSi_2$ layer was developed on the three phase substrate ($Mo+Mo_3Si+Mo_5SiB_2$). After annealing or exposure to air at high temperature, $MoSi_2$ was transformed to T1 phase, which possesses poor oxidation resistance at elevated temperature.
2. Boride phases (MoB and Mo_2B_5) were successfully added to $MoSi_2$ coating either by co-deposition of B and Si or by a two-step process, and the concentrations of boride phases can be controlled by adjusting the Si/B ratio in the pack mixture. However, those boride phases cannot be stabilized with either $MoSi_2$ or Mo_5Si_3 phases after exposure to high temperature. MoB phase was consumed by the formation of Mo_5Si_3 as silicon diffuse downward and the expelled boron diffused downward into substrate to form new borides. As a result, a diffusion zone with Mo_5Si_3/(T2+MoB) layers formed.
3. Both silicide and boron-silicide coating can prevent the oxidation of Mo-4.3Si-1.1B alloy at 1100ºC in both static and cyclic conditions and estimated to be lasted for thousand of hours, while the coating lost their protection at 1600ºC due

to rapid interdiffusion between $MoSi_2$ and substrate, which leads to formation of poorly oxidation resistant T1 phase. The lifetime of $MoSi_2$-based coating is limited by Si depletion through the formation of T1 phase.

4. New coating design approach was proposed based on the diffusion data. T1-based Mo-Si-B coating will reduce the Si depletion rate from the surface by formation of slow growing Mo_3Si or T2 layer without sacrificing the oxidation resistance of the coating, therefore extending the coating lifetime above 1500ºC.

Acknowledgements

"This manuscript has been authored, in whole or in part, under Contract No. DE-AC02-07CH11358 with the U.S. Department of Energy. The United States Government retains and the publisher, by accepting the article for publication, acknowledges that the United States Government retains a non-exclusive, paid-up, irrevocable, world-wide license to publish or reproduce the published form of this manuscript, or allow others to do so, for United States Government purposes."

References

[1] Davis JR, Editor. ASM Specialty Handbook: Heat-Resistant Materials, 1997.

[2] Subramanian PR, Mendiratta MG, Dimiduk DM, Stucke MA. Advanced intermetallic alloys - beyond gamma titanium aluminides. Materials Science & Engineering, A: Structural Materials: Properties, Microstructure and Processing, vol. A239-240, 1997. p.1.

[3] Yamaguchi M, Inui H, Ito K. High-temperature structural intermetallics. Acta Materialia 2000;48:307.

[4] Schneibel JH, Easton DS, Choe H, Ritchie RO. Fracture toughness, creep strength and oxidation resistance of Mo-Mo3Si-Mo5SiB2 molybdenum silicides. Structural Intermetallics 2001, Proceedings of the International Symposium on Structural Intermetallics, 3rd, Jackson Hole, WY, United States, Sept. 23-27, 2001 2001:801.

[5] Dimiduk DM, Perepezko JH. Mo-Si-B alloys: developing a revolutionary turbine-engine material. MRS Bulletin 2003;28:639.

[6] Rosales I, Schneibel JH. Stoichiometry and mechanical properties of Mo3Si. Intermetallics 2000;8:885.

[7] Petrovic JJ, Vasudevan AK. Key developments in high temperature structural silicides. Materials Science & Engineering, A: Structural Materials: Properties, Microstructure and Processing 1999;A261:1.

[8] Petrovic JJ, Vasudevan AK. Overview of high temperature structural silicides. Materials Research Society Symposium Proceedings 1994;322:3.

[9] Schneibel JH, Ritchie RO, Kruzic JJ, Tortorelli PF. Optimizaton of Mo-Si-B intermetallic alloys. Metallurgical and Materials Transactions A: Physical Metallurgy and Materials Science 2005;36A:525.

[10] Meyer MK, Akinc M. Boron-modified molybdenum silicide for sintered articles resistant to creep and oxidation. United States: (Iowa State University Research Foundation, Inc., USA). 1999. p.13 pp

[11] Meyer MK, Akinc M, Kramer MJ. Oxidation resistance and compressive creep behaviors of boron-doped Mo5Si3. Advanced Ceramics for Structural and Tribological Applications, Proceedings of the International Symposium on Advanced Ceramics for Structural and Tribological Applications, Vancouver, B. C., Aug. 20-24, 1995 1995:637.

[12] Meyer M, Kramer M, Akinc M. Boron-doped molybdenum silicides. Advanced Materials (Weinheim, Germany) 1996;8:85.

[13] Akinc M, Meyer MK, Kramer MJ, Thom AJ, Huebsch JJ, Cook B. Boron-doped molybdenum silicides for structural applications. Materials Science & Engineering, A: Structural Materials: Properties, Microstructure and Processing 1999;A261:16.

[14] Meyer MK, Akinc M. Isothermal oxidation behavior of Mo-Si-B intermetallics at 1450 DegC. Journal of the American Ceramic Society 1996;79:2763.

[15] Zhao HL, Kramer MJ, Akinc M. Thermal expansion behavior of intermetallic compounds in the Mo-Si-B system. Intermetallics 2004;12:493.

[16] Schneibel JH, Liu CT, Easton DS, Carmichael CA. Microstructure and mechanical properties of Mo-Mo3Si-Mo5SiB2 silicides. Materials Science & Engineering, A: Structural Materials: Properties, Microstructure and Processing 1999;A261:78.

[17] Schneibel JH, Liu CT, Heatherly L, Kramer MJ. Assessment of processing routes and strength of a 3-phase molybdenum boron silicide (Mo5Si3-Mo5SiB2-Mo3Si). Scripta Materialia 1998;38:1169.

[18] Schneibel JH, Tortorelli PF, Kramer MJ, Thom AJ, Kruzic JJ, Ritchie RO.

Optimization of Mo-Si-B intermetallics. Materials Research Society Symposium Proceedings 2003;753:53.

[19] Sakidja R, Perepezko JH. Phase stability and alloying behavior in the Mo-Si-B system. Metallurgical and Materials Transactions A: Physical Metallurgy and Materials Science 2005;36A:507.

[20] Perepezko JH, Sakidja R, Kim S, Dong Z, Park JS. Multiphase microstructures and stability in high-temperature Mo-Si-B alloys. Structural Intermetallics 2001, Proceedings of the International Symposium on Structural Intermetallics, 3rd, Jackson Hole, WY, United States, Sept. 23-27, 2001 2001:505.

[21] Perepezko JH, Sakidja R, Kumar KS. Mo-Si-B alloys for ultrahigh temperature applications. Advanced Structural Materials 2006:437.

[22] Ito K, Kumagai M, Hayashi T, Yamaguchi M. Room temperature fracture toughness and high temperature strength of T2/Moss and (Mo,Nb)ss/T1/T2 eutectic alloys in the Mo-Si-B system. Scripta Materialia, vol. 49, 2003. p.285.

[23] Berczik DM. Molybdenum alloys with silicon and boron for oxidation resistance. Application: US

US: (United Technologies Corp., USA). 1997. p.6 pp

[24] Schneibel JH, Kramer MJ, Unal O, Wright RN. Processing and mechanical properties of a molybdenum silicide with the composition Mo-12Si-8..5B (at.%). Intermetallics 2001;9:25.

[25] Mendiratta MG, Parthasarathy TA, Dimiduk DM. Oxidation behavior of a Mo-Mo3Si-Mo5SiB2 (T2) three phase system. Intermetallics 2002;10:225.

[26] Parthasarathy TA, Mendiratta MG, Dimiduk DM. Oxidation mechanisms in Mo-

reinforced Mo5SiB2(T2)-Mo3Si alloys. Acta Materialia 2002;50:1857.

[27] Kruzic JJ, Schneibel JH, Ritchie RO. Fracture and fatigue resistance of Mo-Si-B alloys for ultrahigh-temperature structural applications. Scripta Materialia 2003;50:459.

[28] Sakidja R, Park JS, Hamann J, Perepezko JH. Synthesis of oxidation resistant silicide coatings on Mo-Si-B alloys. Scripta Materialia 2005;53:723.

[29] Ito K, Murakami T, Adachi K, Yamaguchi M. Oxidation behavior of Mo-9Si-18B alloy pack-cemented in a Si-base pack mixture. Intermetallics 2003;11:763.

[30] Sakidja R, Park JS, Hamann J, Perepezko JH. Synthesis of oxidation resistant silicide coatings on Mo-Si-B alloys. Scripta Materialia, vol. 53, 2005. p.723.

[31] Yoon J-K, Byun J-Y, Kim G-H, Kim J-S, Choi C-S. Multilayer diffusion growth in silicon-molybdenum interactions. Thin solid films 2002;405:170.

[32] Mandal P, Thom AJ, Kramer MJ, Behrani V, Akinc M. Oxidation behavior of Mo-Si-B alloys in wet air. Materials Science & Engineering, A: Structural Materials: Properties, Microstructure and Processing, vol. A371, 2004. p.335.

[33] Ito K, Hayashi T, Yokobayashi M, Murakami T, Numakura H. Oxidation protective silicide coating on Mo-Si-B alloys. Metallurgical and Materials Transactions A: Physical Metallurgy and Materials Science 2005;36A:627.

[34] Kircher TA, Courtright EL. Engineering limitation of MoSi2 coating. Materials Science & Engineering, A: Structural Materials: Properties, Microstructure and Processing 1992;155:67.

[35] Schutze M. Fundamentals of high temperature corrosion. Materials Science and Technology 2000;19:67.

[36] Ihara K, Ito K, Tanaka K, Yamaguchi M. Mechanical properties of Mo5SiB2 single

crystals. Materials Science & Engineering, A: Structural Materials: Properties, Microstructure and Processing 2002;A329-A331:222.

[37] Nakamura M, Matsumoto S, Hirano T. Elastic constants of $MoSi_2$ and WSi_2 single crystals. Journal of Materials Science 1990;25:3309.

[38] Ito K, Ihara K, Tanaka K, Fujikura M, Yamaguchi M. Physical and mechanical properties of single crystals of the T2 phase in the Mo-Si-B system. Intermetallics 2001;9:591.

[39] Baskes MI. Atomistic potentials for the molybdenum-silicon system. Materials Science & Engineering, A: Structural Materials: Properties, Microstructure and Processing 1999;A261:165.

[40] Chu F, Thoma DJ, McClellan KJ, Peralta P. Mo5Si3 single crystals: physical properties and mechanical behavior. Materials Science & Engineering, A: Structural Materials: Properties, Microstructure and Processing 1999;A261:44.

[41] Yoon JK, Byun JY, Kim JS, Choi CS. Effect of Mn alloying on the growth rate and oxidation resistance of MoSi2 coatings. Taehan Kumsok Hakhoechi 1998;36:2143.

[42] Maloney MJ, Hecht RJ. Refractory additions for improving molybdenum disilicide composites reinforced with ceramic fibers. Application: US
US: (United Technologies Corp., USA). 1994. p.6 pp.

[43] Yoon J-K, Lee J-K, Lee K-H, Byun J-Y, Kim G-H, Hong K-T. Microstructure and growth kinetics of the Mo5Si3 and Mo3Si layers in MoSi2/Mo diffusion couple. Intermetallics 2003;11:687.

[44] Yoon J-K, Kim G-H, Byun J-Y, Kim J-S, Choi C-S. Simultaneous growth mechanism of intermediate silicides in MoSi2/Mo system. Surface and Coatings Technology

2001;148:129.

[45] Christensen AN. Preparation and characterization of molybdenum silicides (Mo3Si and Mo5Si3). Acta Chemica Scandinavica, Series A: Physical and Inorganic Chemistry 1983;A37:519.

[46] Tortorici PC. Diffusion and phase formation in selected refractory metal silicides. 1997. p.209 pp.

[47] Hayashi T, Ito K, Numakura H. Reaction diffusion of MoSi2 and Mo5SiB2. Intermetallics 2004;13:93.

[48] Glushko PI, Zmii VI, Semenov NA, Shirokov BM. Stability and heat resistance of silicide coatings on refractory metals. Part 3. Stability of silicide coatings on niobium heated in air at 1500-1800 DegC. Powder Metallurgy and Metal Ceramics (Translation of Poroshkovaya Metallurgiya (Kiev)) 2003;42:154.

[49] Thom AJ, Summers E, Akinc M. Oxidation behavior of extruded Mo5Si3Bx-MoSi2-MoB intermetallics from 600 Deg-1600 DegC. Intermetallics, vol. 10, 2002. p.555.

[50] Thom AJ, Kramer MJ, Mandal P, Akinc M. Wet air and simulated combustion gas exposures of Mo-Si-B alloys. Scripta Materialia, vol. 53, 2005. p.915.

Chapter 5. Evaluation of Phase Equilibria in the Nb-rich Portion of Nb-B System

Zhihong Tang, Matthew J. Kramer and Mufit Akinc

A paper to be submitted to *Intermetallics*

Abstract

The phase equilibria in the Nb-rich portion of Nb-B system has been evaluated experimentally using metallographic analysis, differential thermal analyzer (DTA) and X-ray diffraction. It showed that Nb_{ss} (solid solution) and NbB are the only two primary phases in the 0-40 at.% B composition range, and the eutectic reaction $L \leftrightarrow Nb_{ss} + NbB$ exists, instead of generally accepted reaction: $L \leftrightarrow Nb_{ss} + Nb_3B_2$ as indicated in the Nb-B phase diagram. The Nb_3B_2 phase, however, forms by the peritectoid reaction $Nb_{ss} + NbB \leftrightarrow Nb_3B_2$. DTA tests were conducted on annealed Nb-14B, Nb-16B, Nb-18B and Nb-40 alloys, and temperature and heat of phase transition were determined. The eutectic reaction ($L \leftrightarrow Nb_{ss} + NbB$) temperature was determined to be 2104±5˚C, and the heat of phase transition was estimated as from 22 to 30 kJ/mol, depending on the method of calibration used. The thermal event associated with peritectoid reactions was not observed in DTA curves due to sluggish solid state transformation, but the thermal annealing experiments show that peritectoid temperature is above 1900˚C.

Keyword: A. Intermetallics; B. Phase diagrams; B. thermal properties; D. microstructure

Introduction

Composites based on refractory metal silicide quaternary system, such as M-M_5X_3 (where M=Mo or Nb, and X=Si or B) are being considered for high temperature structural applications because of their high temperature strength retention [1-5]. In order to establish the Mo-Nb-Si-B quarternary phase equilibria, accurate binary and ternary equilibria are needed. {Although most binary and ternary phase diagrams are available in *Binary Alloy Phase Diagrams* edited by Massalski et al. [6] and *Handbook of Ternary Alloy Phase Diagrams* edited by Villars in 1995 [7],} Two versions of Nb-B phase diagram, were published, shown in Figure 49a [6] and Figure 49b [8]. One was published in Binary alloy phase diagrams edited by Massalski et al., which was calculated by based on thermodynamic model, while the other one was proposed by Rudy et.al. in 1969 and was experimentally determined by the quenching studies and differential thermal analysis (DTA). In addition, the DTA measurements in Rudy's work was limited to temperatures below 2100°C, which was far below the temperature of most phase transformations in Nb-B system and need further evaluations. While there is a general agreement in the stability of NbB, Nb_3B_4, Nb_5B_6 and NbB_2 phases; however, the reactions involving Nb_3B_2 are in contradiction. Nb_3B_2 phase in Figure 49a is associated with a eutectic, $L \leftrightarrow Nb_{ss} + Nb_3B_2$, and a peritectic $L + NbB \leftrightarrow Nb_3B_2$ reactions, while the one in Figure 49b indicates that the Nb_3B_2 forms by a peritectoid reaction: $Nb_{ss} + NbB \leftrightarrow Nb_3B_2$. To add to the confusion, a recent study by Borges et al. [9] indicated that Nb_{ss} and NbB are the only primary phases in the Nb-rich region, Nb_3B_2 is only formed by the peritectoid reaction: $Nb_{ss} + NbB \leftrightarrow Nb_3B_2$; and there

exists a eutectic reaction: $L \rightarrow Nb_{ss} + NbB$ with the eutectic concentration close to 16%B. The phase transition temperatures for eutectic and peritectoid reactions were not reported.

The present work re-examines the Nb-rich region of the Nb-Si phase diagram using ultra high temperature thermo gravimetric analyzer and metallography to clarify the phase diagram in the vicinity of the Nb_3B_2 phase field.

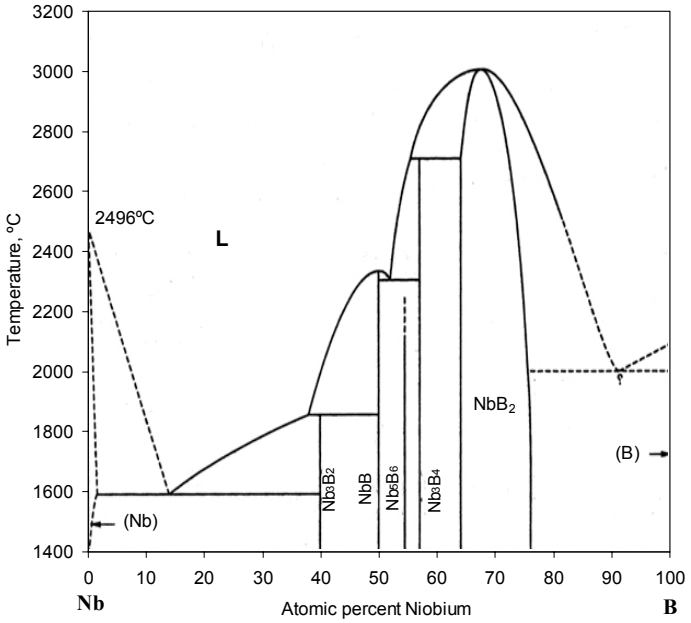

(a)

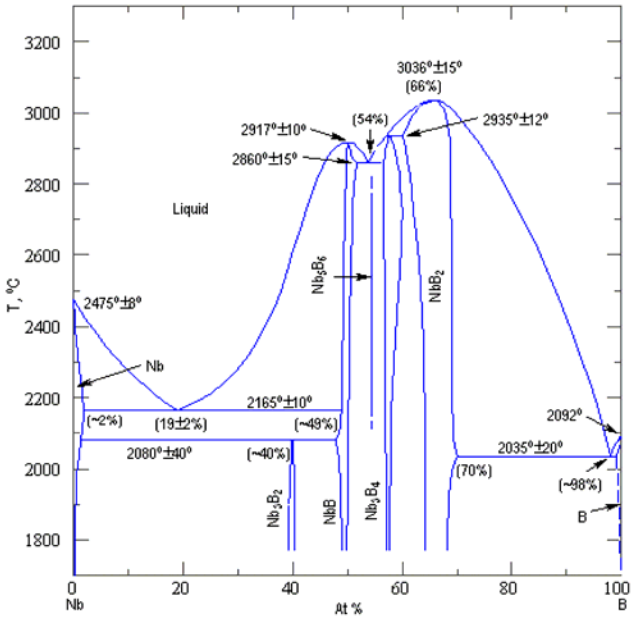

(b)

Figure 49 Nb-B binary phase diagram a) published in *Binary alloy phases diagram* edited by Massalski et al.[6]; b) Proposed by Rudy et al.[8] in 1996. The significant controversy between these two phase diagrams in Nb-rich region (0-50 at.%B) are the stability of Nb_3B_2 and type of invariant reaction which concerning the formation of Nb_3B_2.

Experimental procedure

Sample preparation

All Nb-B binary alloys in this study were synthesized via arc-melting. Arc-melting was performed in an ultra-high purity (UHP) argon atmosphere on a water-chilled copper hearth. The starting materials included niobium (Alfa AESAR, 99.9%) and boron species (Cerac. 99.5%). Sample, which weighed approximately 20g each, were melted at least three times via non-consumable tungsten electrode. The weight losses during the melting were less than 0.4% for all samples. The compositions are listed in Table 8. Only alloys with B concentrations less than 40 at. % were examined.

Table 8 Nominal and calculated composition of selected Nb-B alloy

Nominal composition, at.% B	Initial mass, g	Mass loss, %	Calculated composition, at.% B	
			a	b
10.00	20.70	-0.10	9.32	10.01
14.00	20.34	-0.21	12.63	14.03
16.00	20.63	-0.10	15.40	16.01
18.00	20.36	-0.08	17.50	18.01
22.00	20.30	-0.33	20.20	22.06
30.00	20.70	-0.19	29.16	30.04
40.00	20.15	-0.30	38.98	40.08

Note: Mass variation=[(final mass-initial mass)/final mass]× 100%

a. Composition of alloy assuming mass loss associated with boron volatilization
b. Composition of alloy assuming mass loss associated with niobium volatilization

The cast ingots were heat treated at 1900ºC for up to 24 hours in flowing UHP argon atmosphere. All samples were examined with SEM and energy dispersive spectrometry

(EDS). X-ray diffraction (XRD) analysis was performed on cast and annealed alloys for structure and compositional assessment.

Differential thermal analysis (DTA)

Performing ultra-high temperature thermal analysis is fought with many difficulties: appropriate environment, reaction with the crucible and calibration to name a few. The phase transformation temperatures in Nb-B binary system are typically above 2000ºC, thus an ultra-high temperature TG/DTA instrument (Linseis L81/042C, LINSEIS Inc., Germany) with temperature capability up to 2400ºC fitted with tungsten heating elements and shields was employed to determine phase transition temperatures. The instrument, which runs in static or dynamic gas atmospheres, was equipped with a turbo molecular pump system with a vacuum capability down to 10^{-10} Torr to minimize the atmospheric contaminations. The temperature measurements were carried out by a type C thermocouple (W-5%Rh vs. W-26%Rh). Heating and cooling rate can be accurately controlled from 0 to 50ºC/min in the temperature range 100-2400ºC.

Due to arcing discharge when using Ar above 1800ºC, high purity helium was employed as an inert flowing atmosphere. Even though helium resulted in a larger heat loss due to its much higher specific heat capacity than nitrogen and argon (5.193 vs. 1.04 and 0.52 J/g·ºC), the baseline tests with no sample showed that high thermal capacity of He did not adversely affect controlling the heating rate up to 2300ºC.

After screening potential refractory nitrides, oxides, carbides and borides as a liner material, yttria stabilized zirconia (YSZ, 8wt.%Y_2O_3) was judged to be the best crucible liner material to protect the tungsten crucible. Reactivity of Nb-16B with YSZ is checked by embedding the alloy in YSZ powder and heating to 2300ºC. As shown in Figure 50, no

reaction was detected at the Nb-16B alloy and YSZ powder interface, nor did EDS analysis show presence of Nb in YSZ powder or Y and Zr in Nb-16B alloy confirming that no reaction or dissolution occurs between NbB and YSZ powder up to 2300ºC.

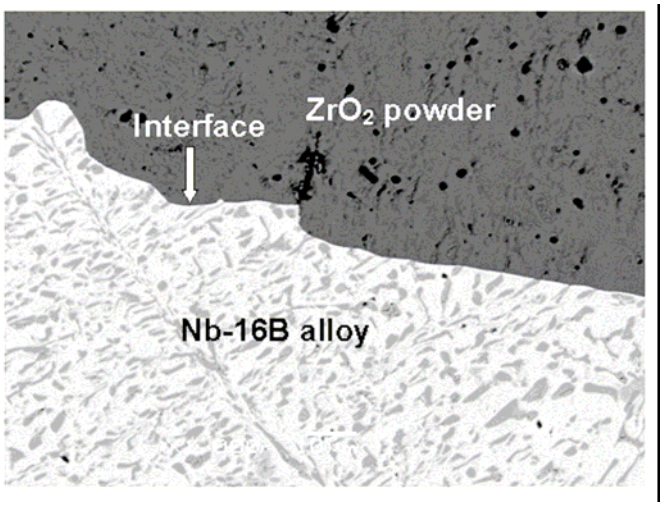

Figure 50 Interface zone between YSZ powder and Nb-16B alloy after heat treatment at 2300ºC. No reaction zone between YSZ and Nb-16B alloy was observed

The YSZ liners were prepared in Materials processing Center (USDOE Ames laboratory) by air plasma spray. The Molten YSZ powder was sprayed onto the rounded tips of graphite rods with appropriate diameter and length to fit the tungsten crucible. YSZ coated graphite rods were held at 1000ºC for 48 hours in flowing air to burn the graphite. Finally, the YSZ crucibles were fired at 1400ºC in air for 2-3 hours to remove the graphite residue.

The arc-melted Nb-B alloys for DTA were cut into 2×2×3mm samples, each weighing about 100mg. The samples were ultrasonically cleaned in ethanol, and then loaded into the YSZ lined tungsten crucible. The reference thermocouple was attached to an identical empty YSZ lined tungsten crucible. The Zr-gettered ultra-high purity helium gas flows through system at 60mL/min throughout the experiment. Before heating, the chamber

was evacuated (<10^{-7} torr) and backfilled with UHP He several times to eliminate any atmospheric impurities. The furnace was heated to 1800ºC at 50ºC/min, followed at slower rates ranging fromfrom 10 to 30 °C/min to 2400ºC for DTA analysis[MJK1].

The equilibrium phase transformation temperature was estimated from the onset temperatures using an extrapolation method proposed by Zhu et al.[10],

$$T_{Measured,onset} = C \times r + T_{equilibrium}\ \text{[MJK2]} \qquad (1)$$

Where C is a constant and r is the heating or cooling rate (ºC/min). In this study, the onset temperatures were typically determined at five different heating rates (10, 15, 20, 25 and 30ºC/min) to obtain a linear extrapolation and determine an accurate equilibrium phase transition temperature $T_{eauilibrium}$. Only the onset transition temperature during heating was considered because of significant undercooling on cooling leading to inaccurate phase transformation temperatures.

Results and discussion

Microstructural analysis

As shown in Figure 51, the cast Nb-10B and Nb-14B alloys exhibit Nb_{ss} as the primary phase with a eutectic microstructure formed by Nb_{ss} and NbB phases, while Nb-22B, Nb-30B and Nb-40B alloys show a primary NbB phase along with the same Nb_{ss}/NbB eutectic microstructure. For Nb-16B alloy, a typical Nb_{ss} + NbB only eutectic microstructure is observed, while for Nb-18B alloy, NbB primary phase with a lamellar eutectic morphology appears. The phase assemblage of various Nb-B alloys was checked by powder XRD analysis. As shown in Figure 52a, only Nb (PDF# 00-035-0789) and NbB (PDF# 00-032-0709) phases were identified, and the fraction of NbB phase increases with increasing B

concentration. No Nb_3B_2 phase was observed in any of the cast alloys. These results are consistent with Borges' observations and the phase diagram proposed by Rudy et al in 1966, and it suggest that the eutectic reaction is $L \leftrightarrow Nb_{ss} + NbB$, rather than the reaction: $L \leftrightarrow Nb_{ss} + Nb_3B_2$ as shown in the phase diagram published in 1990. The eutectic composition is close to 16 at% B.

Annealing cast Nb-B alloys at 1900ºC for 2 hours in argon leads to the formation of Nb_3B_2 (PDF# 00-012-0111) as confirmed by XRD. Both the XRD patterns and the micrographs of the annealed Nb-10B and Nb-16B samples exhibited only Nb_{ss} and Nb_3B_2 phases. The initial NbB in as-cast alloys was completely consumed, suggesting formation of Nb_3B_2 through a peritectoid reaction $Nb_{ss} + NbB \leftrightarrow Nb_3B_2$. This peritectoid reaction is more clearly shown in Figure 53 where NbB was only partially converted to Nb_3B_2 for Nb-30B (Figure 53c) and Nb-40B (Figure 53d) alloys. For these compositions NbB remains as isolated islands surrounded by Nb_3B_2 perhaps due to sluggish diffusion of either B or Nb through the Nb_3B_2 phase.

The XRD and microstructure analyses of cast and annealed Nb-B alloy agree well with the phase diagram proposed in 1966 with respect to phase assemblages and the type of invariant reactions in the Nb-rich side (0-40 at.% B). Accurate estimation of the eutectic and peritectoid reaction temperatures has yet to be done.

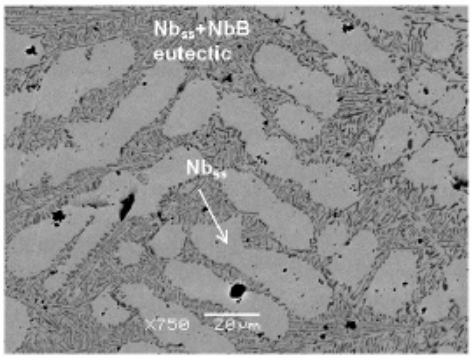

(a)

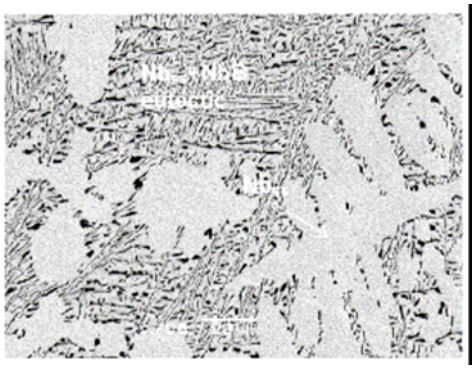

(b)

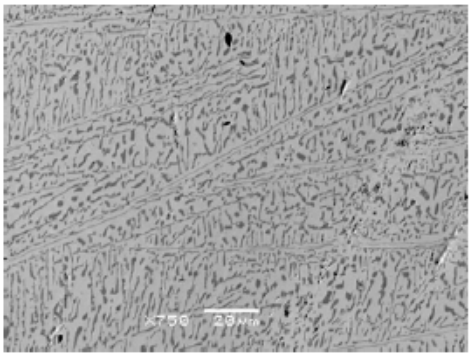

(c)

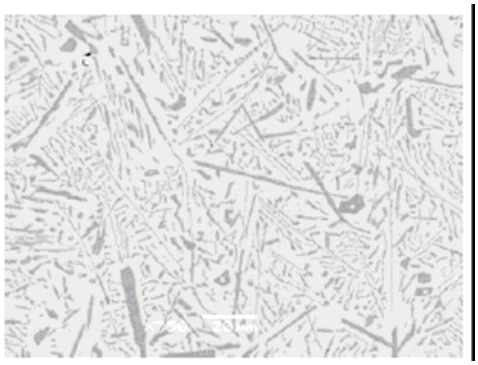

(d)

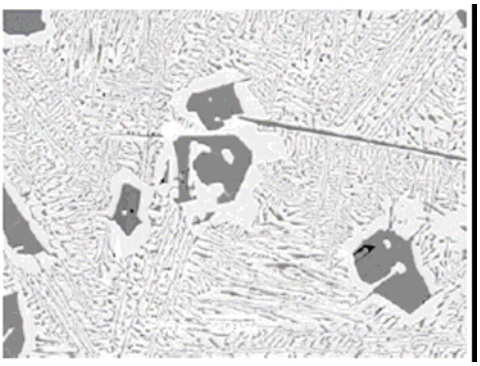

(e)

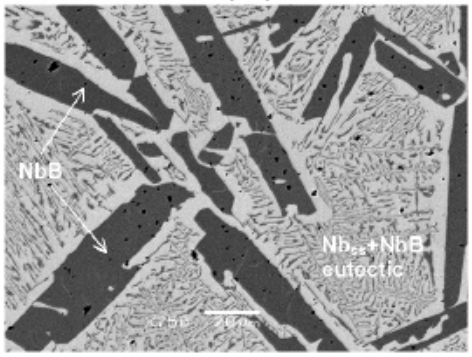

(f)

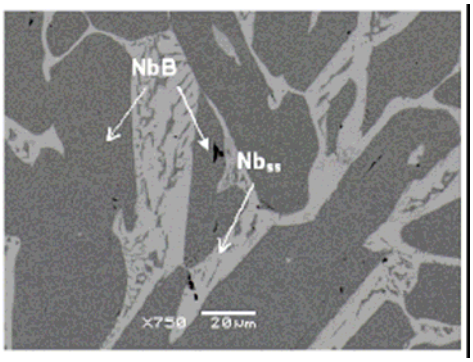

(f)

Figure 51 SEM/BSE micrographs of various cast Nb-B alloys: a) Nb-10B; b) Nb-14B; c) Nb-16B; d) Nb-18B; e) Nb-22B; f) Nb-30B; g) Nb-40B. These micrographs show that Nb_{ss} and NbB are the only two primary phases in the Nb-rich region (0-50 at.%B), and eutectic reaction $L \leftrightarrow Nb_{ss} + NbB$ exists.

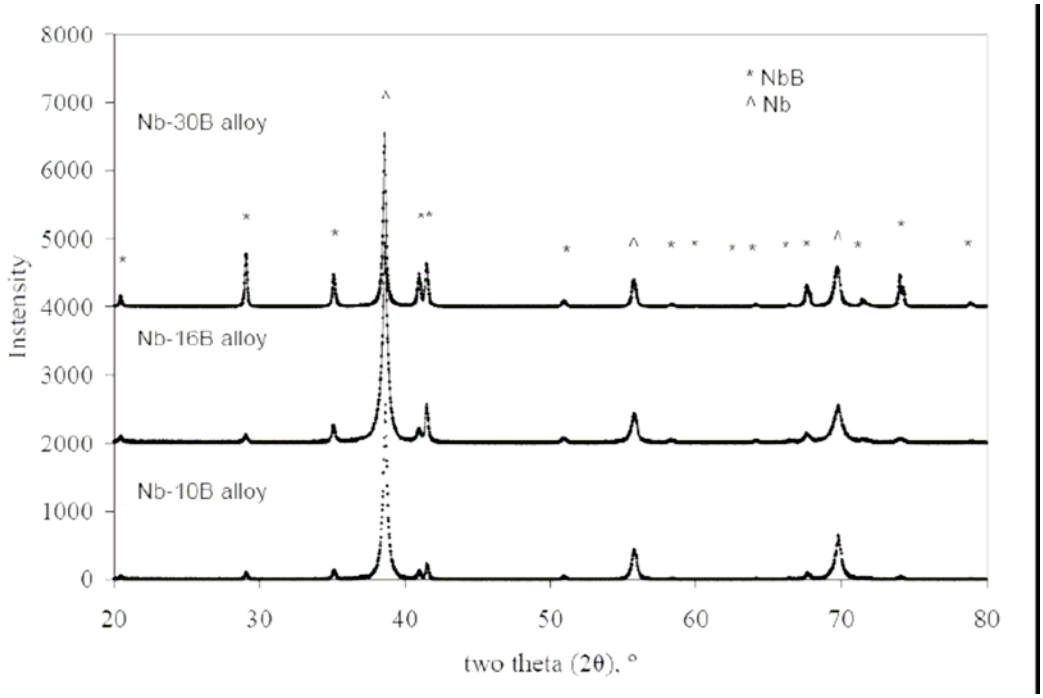

(a)

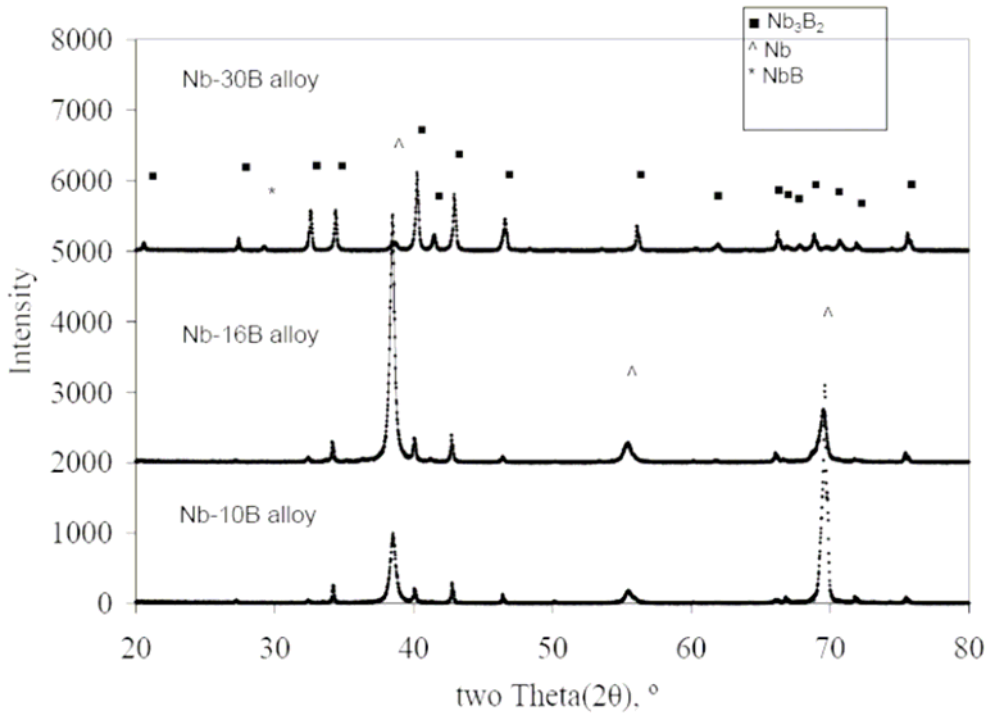

(b)

Figure 52 XRD patterns of a) cast and annealed select alloys (Nb-10B, Nb-16B and Nb-30B), indicating the existence of only Nb and NbB as the stable phases.

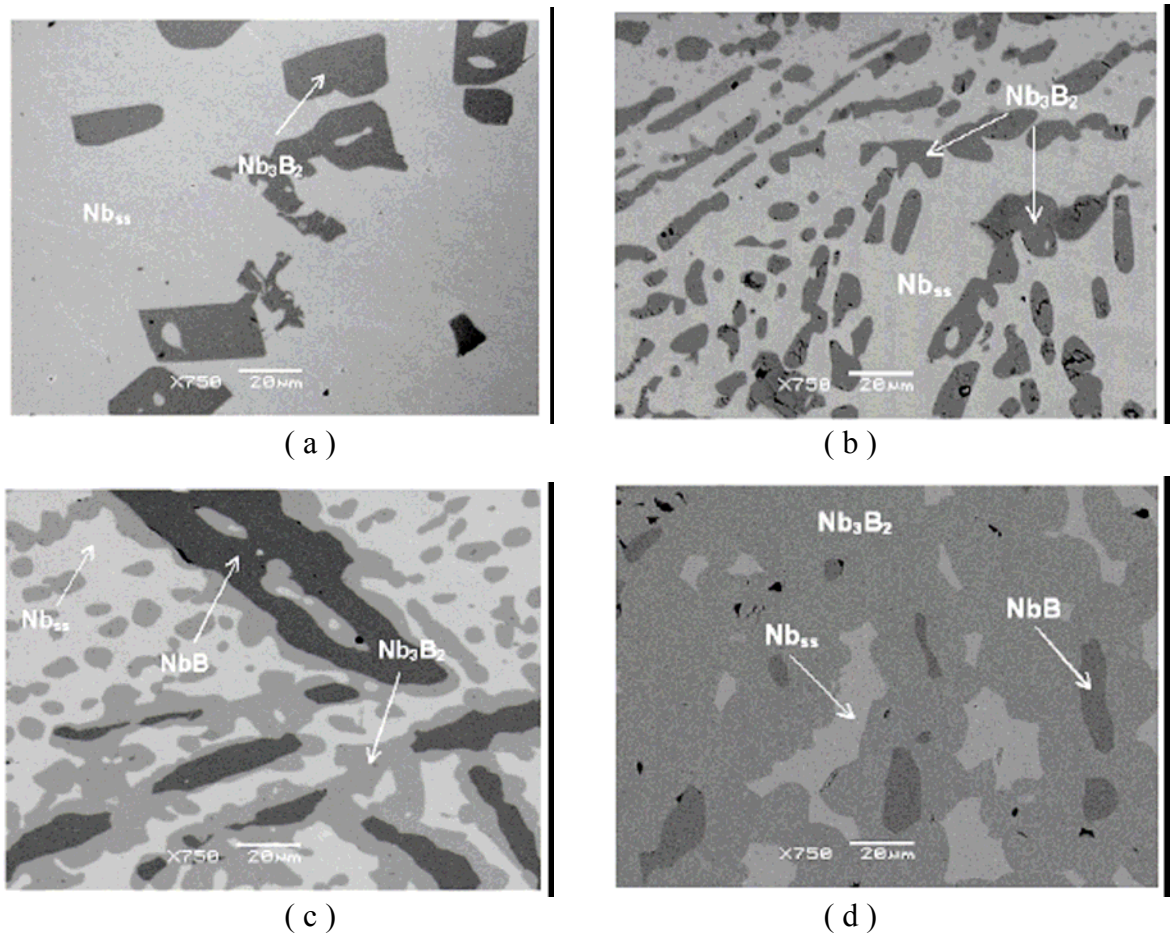

Figure 53 SEM/BSE micrographs of various Nb-B alloys annealed at 1900ºC for 2 hours: a) Nb-10B; b) Nb-16B; c) Nb-30B; d) Nb-40B, indicating the formation of Nb_3B_2 by the peritectoid reaction: $Nb_{ss} + NbB \leftrightarrow Nb_3B_2$.

DTA results

Calibration of temperature and enthalpy

The DTA was calibrated using ASTME 967 standardized procedure (1999)[11]. In the two point method, two celebrants' are chosen to bracket the temperature range of interest. It is assumed that the correct temperature T is related to the experimental temperature T_{exp} by the relationship:

$$T = T_{exp}S + I \qquad (2)$$

S and I are defined by the relationship:

$$S = (T_1 - T_2)/(T_{\exp 1} - T_{\exp 2})$$
$$I = \left[(T_{\exp 1} \times T_2) - (T_{\exp 2} \times T_1)\right]/(T_{\exp 1} - T_{\exp 2}) \qquad (3)$$

where the subscripts 1 and 2 refer to the two calibrants.

Although Differential Thermal Analysis (DTA) is not as accurate as differential scanning calorimetry (DSC) to quantitatively measure the change in enthalpy, a simplification can be made if one assumes a direct relationship between ΔT and ΔH and ignore the influences of the asymmetric heat transfer from the environment to the sample and reference materials. Such an assumption is reasonable when a significant transition heat is measured over a narrow range of temperatures [12]. Thus, in quantitative studies, the heat of transition ΔH of a sample can be related to the area A under the DTA curve by means of a proportionality or instrumental factor ψ [13]:

$$\Delta H = \psi A \qquad (4)$$

In the present study Rh metal , and Al_2O_3, which have melting temperatures of 1963.85ºC and 2053.85 ºC, respectively, have been chosen as calibrants to correct for the temperature near the phase transition temperature of Nb-B alloy. The measured melting temperatures as a function of heating rate for both Al_2O_3 and Rh are shown in Figure 54. The equilibrium temperatures were determined by linearly extrapolating the $T_{measured,\,\text{onset}}$ vs. heating rate, *r,* curve to zero using the equation (1), and the melting temperatures of 1966.1ºC and 2059.4ºC were obtained for Rh and Al_2O_3, respectively. Substituting these values for T_{exp1} and T_{exp2} in equation (3), the following values of S = 0.94646(3) and I = 67.2(9) were obtained for Eq. (2).

The final calibration data are shown in Table 9, The instrumental factors determined using equation 4 are 0.048±0.003 and 0.036±0.001 J/μv·s for Al_2O_3 and Rh, respectively.

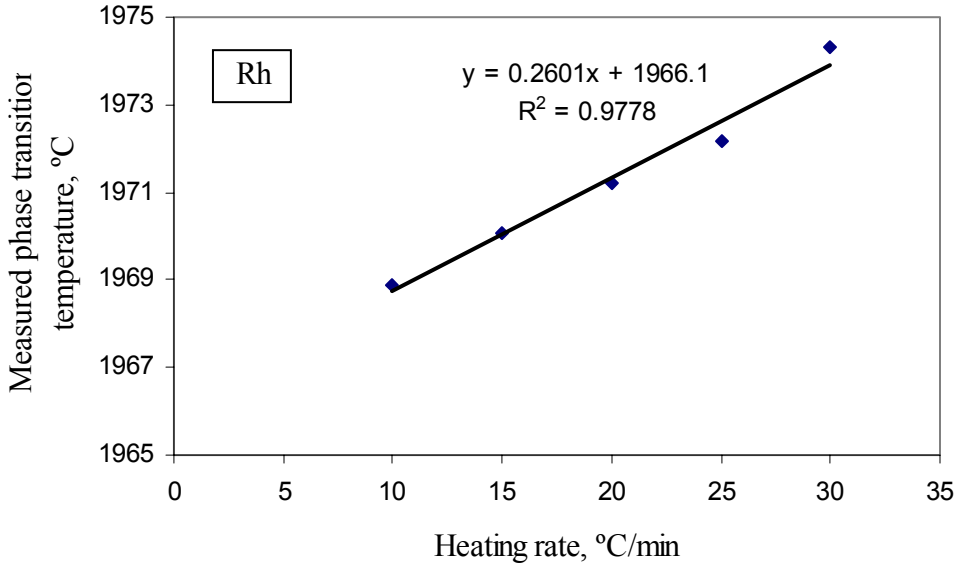

(a)

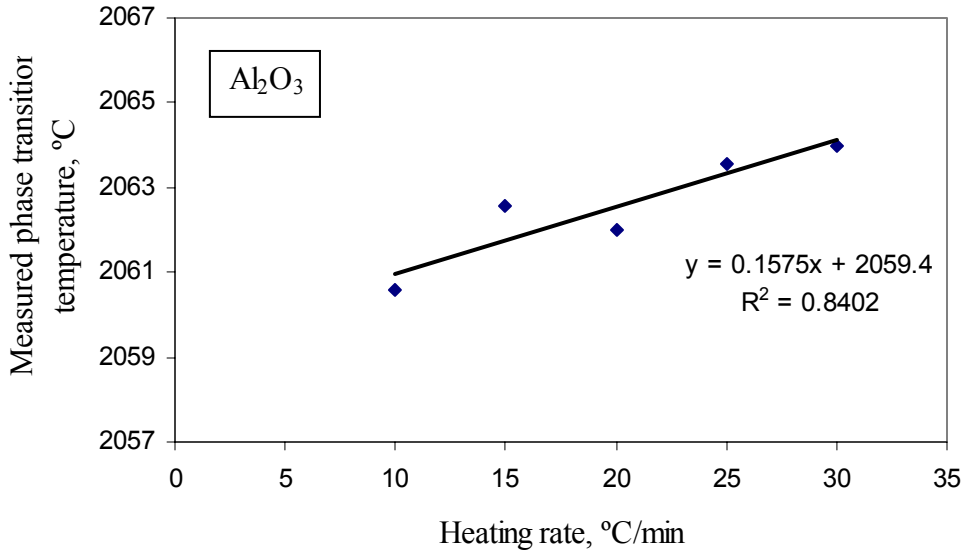

(b)

Figure 54 Measured melting temperatures for a) Rh and b) Al_2O_3 calibrants as a function of heating rate.

Table 9 Measurement of instrumental factor ψ for two Al_2O_3 and Rh calibrants.

Calibrants	$T_{equilibrium, exp,}$ °C	T_m, °C	Average peak area, μv·s/mg	Enthalpy of fusion, ΔH_{fus}, KJ/mol	Instrumental factor, ψ, J/μv·s
Al_2O_3	2059.4	2053.85	22.62±1.20	111.1	0.048±0.003
Rh	1966.1	1963.85	7.26±0.16	26.59	0.036±0.001

Determination of phase transition temperature and enthalpy.

The DTA tests were conducted on the annealed Nb-16B alloy. The typical DTA curve for Nb-16B alloy is shown in Figure 55. Only a negative peak associated with an endothermic thermal event was visible during the heating, and a corresponding positive (exothermic) peak during cooling. This thermal event was thought to be associated with the eutectic reaction $L \leftrightarrow Nb_{ss} + NbB$. DTA tests were also performed on Nb-10B, Nb-14, Nb-18B and Nb-40B alloys, only one endothermic peak was observed in all cases.

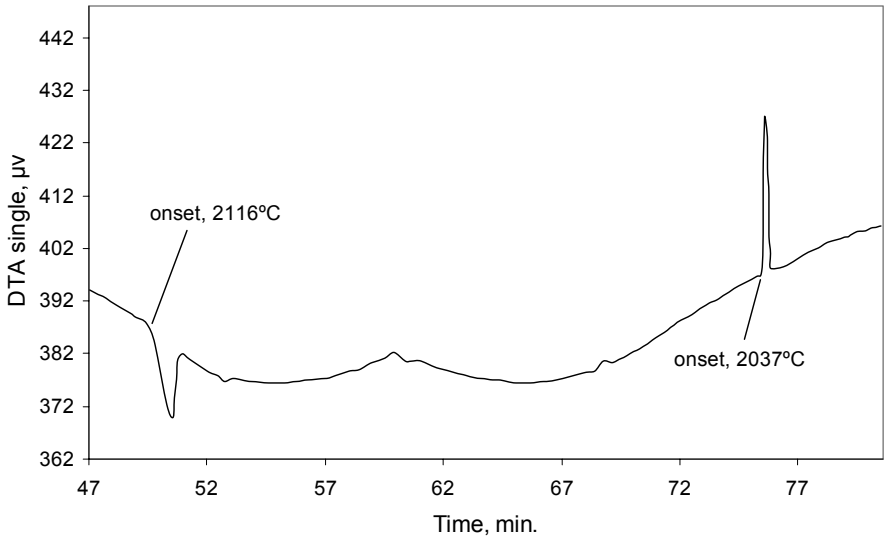

Figure 55 DTA curve for Nb-16B with a heating/cooling rate of 25ºC/min. Note the endothermic reaction on heating is reversible and appears as an exotherm upon cooling but with a significant undercooling.

The thermal event associated with peritectoid reaction $Nb_{ss} + NbB \leftrightarrow Nb_3B_2$ is not visible in DTA curves perhaps due to a sluggish solid state transformation as confirmed by thermal annealing the Nb-30B alloy in Ar at 1900ºC for 24 hours. (Fig. 56)

The measured melting temperature as a function of heating rate for Nb-14B, Nb-16B and Nb-18B alloys are shown in Figure 57. The equilibrium phase transition temperature were determined by linearly extrapolating T vs. heating rate to zero and corrected using Equation (5). The results are summarized in Table 10. The average phase transition temperature for the eutectic reaction is determined to be 2104±5˚C, and the heat of phase transition ranged from 22.5±0.6 to 30.0±1.8 kJ/mol with Rh and Al_2O_3calibrants, respectively. This measured eutectic temperature is somewhat lower than the value (2165±10˚C) reported by Rudy et al [8[MJK3]], which was based on experimental measurements.

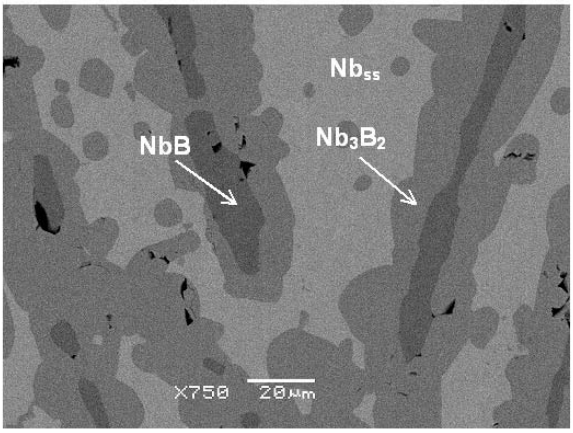

Figure 56 SEM/BSE micrographs of Nb-30B alloy annealed at 1900ºC for 24 hours.

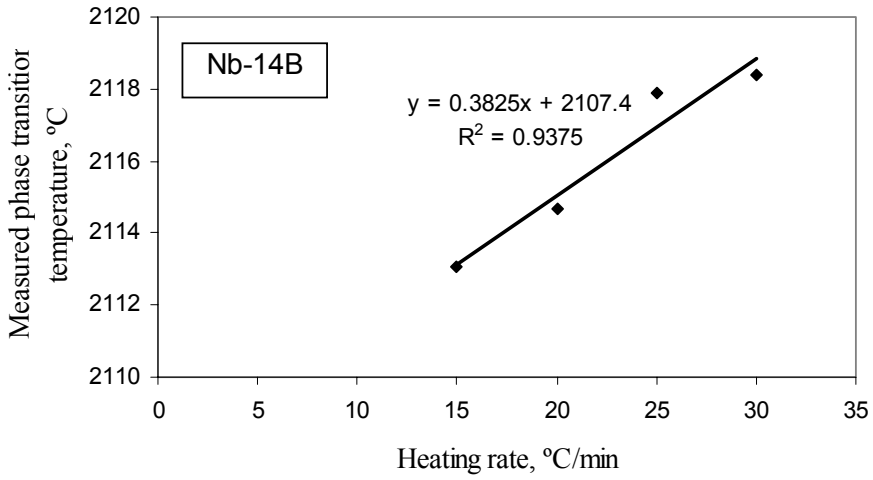
Nb-14B
y = 0.3825x + 2107.4
R2 = 0.9375
Measured phase transitior temperature, ºC
Heating rate, ºC/min
2120
2118
2116
2114
2112
2110
0
5
10
15
20
25
30
35

(a)

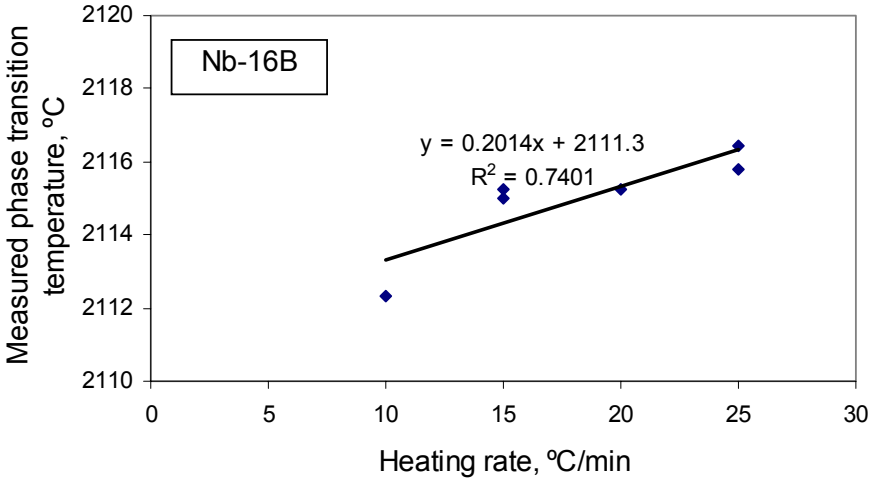
Nb-16B
y = 0.2014x + 2111.3
R2 = 0.7401
Measured phase transition temperature, ºC
Heating rate, ºC/min
2120
2118
2116
2114
2112
2110
0
5
10
15
20
25
30

(b)

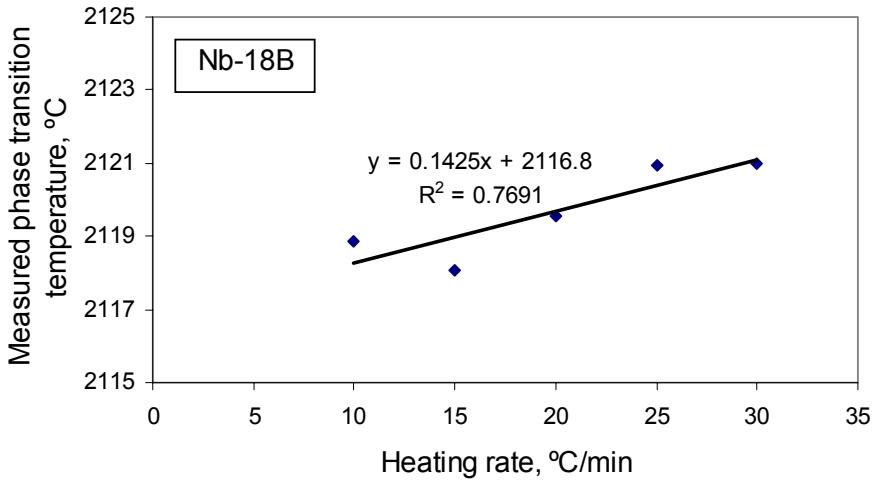

(c)

Figure 57 Measured melting temperatures as a function of heating rate for various annealed alloys: Nb-14B; Nb-16B and Nb-18B.

Table 10 Determination of phase transition temperature and heat for Nb-14B, Nb-16B and Nb-18B alloys

Alloys	$T_{equilibrium, exp}$, °C	$T_{correct}$, °C	Average peak area, μv·s/mg	Measured Enthalpy, ΔH (KJ/mol)	
				With Al_2O_3 correction	With Rh correction
Nb-14B	2107	2100	3.14±0.25	12.3±0.6	9.2±0.3
Nb-16B	2111	2104	7.83±0.46	30.0±1.8	22.5±0.6
Nb-18B	2117	2109	7.32±0.24	27.5±1.6	20.6±0.6
Average $T_{eutectic}$ =2104±5°C					

Conclusions

The phase equilibria in the Nb-rich region of Nb-B system was examined by metallographic and thermal analyses. Two Nb-B phase diagrams available in the literature conflict with respect to formation of Nb_3B_2 were re-evaluated. Our experimental results

confirm the phase diagram proposed by Rudy and Windisch in the composition range of 0-40 at.%B that:

- Nb_{ss} and NbB are the only two primary phases in the composition range of 0-40 at.% B, and the eutectic reaction $L \leftrightarrow Nb_{ss} + NbB$ occurs at ~16 at. %B,
- The eutectic reaction takes place at 2104±5˚C with a heat fusion of 30.0±1.8 and 22.5±0.6 KJ/mol depending on the choice of calibrants Al_2O_3 and Rh, respectively,
- Nb_3B_2 is formed by the peritectoid reaction: $Nb_{ss} + NbB \leftrightarrow Nb_3B_2$, and the peritectoid temperature was difficult to determine accurately but occurs between 1900 and 2100˚C.

Acknowledgements

"This manuscript has been authored, in whole or in part, under Contract No. DE-AC02-07CH11358 with the U.S. Department of Energy. The United States Government retains and the publisher, by accepting the article for publication, acknowledges that the United States Government retains a non-exclusive, paid-up, irrevocable, world-wide license to publish or reproduce the published form of this manuscript, or allow others to do so, for United States Government purposes."

References

[1] Liu Y, Thom AJ, Kramer MJ, Akinc M. Processing and oxidation behavior of Nb-Si-B intermetallics. Processing and Fabrication of Advanced Materials XI, [Proceedings of the International Symposium on Processing and Fabrication of Advanced Materials], 11th, Columbus, OH, United States, Oct. 7-10, 2002 2003:258.

[2] Katrych S, Grytsiv A, Bondar A, Rogl P, Velikanova T, Bohn M. Structural materials: metal-silicon-boron. The Nb-rich corner of the Nb-Si-B system. Journal of Solid State Chemistry 2004;177:493.

[3] Behrani V, Thom AJ, Kramer MJ, Akinc M. Microstructure and oxidation behavior of Nb-Mo-Si-B alloys. Intermetallics 2005;14:24.

[4] Liu Y, Kramer MJ, Thom AJ, Akinc M. Oxidation behavior of multiphase Nb-Mo-Si-B intermetallics. Metallurgical and Materials Transactions A: Physical Metallurgy and Materials Science 2005;36A:601.

[5] Junior DMP, Nunes CA, Coelho GC, Ferreira F. Liquidus projection of the Nb-Si-B system in the Nb-rich region. Intermetallics 2003;11:251.

[6] Massalski TB, Okamoto H, Subramanian PR, Kacprzk L. Binary alloy phase diagrams. Materials Park, Ohio: ASM international 1990.

[7] Villars P. handbook of ternary alloy phase diagrams. Materials Park, OH: ASM international, 1995.

[8] Rudy E, Windisch S. Part I. Related binary systems. Volume X. Systems V-B, Nb-B and Ta-B. Tenary phase equlibria in transition metal-boron-caron-silicion systems. Wright-Patterson Air Force Base: Air Force Materials Laboratory, 1966. p.1.

[9] Borges LA, Jr., Coelho GC, Nunes CA, Suzuki PA. New data on phase equilibria in the Nb-rich region of the Nb-B system. Journal of Phase Equilibria 2003;24:140.

[10] Zhu YT, Devletian JH, Manthiram A. Application of differential thermal analysis to solid-solid transitions in phase diagram determination. Journal of Phase Equilibria 1994;15:37.

[11] Haines PJ, Heal GR, Laye PG, Price DM, Warrington SB, Wilson RJ. Principles of thermal analysis and calorimetry. Cambridge, UK: The Royal Society of Chemistry, 2002.

[12] Wunderlich B. Thermal Analysis. London: Academic Press Limited, 1990.

[13] O'Neill G, Wall WF. High-temperature quantitative DTA analysis. High Temperatures - High Pressures 1979;11:281.

Chapter 6. General Conclusion

This study was motivated by the aim to exploite new high-temperature materials beyond Ni-based superalloys. Some issues, including the oxidation mechanism of Ti_5Si_3-based alloy at elevated temperature, protection of Mo-based Mo-Si-B in-situ composite from high temperature oxidation, reevaluation of Nb-B binary phase diagram, were investigated. Though these results provide a better understanding of high-temperature oxidation and protection of M_5Si_3 (M=Ti, Nb, Mo) based transition-metal silicides, further work is required to make these materials a competitive choice for ultra-high temperature applications.

Oxidation mechanism of Ti_5Si_3 based alloys

Binary Ti_5Si_3 alloys show slow parabolic oxidation kinetics in pure oxygen over the whole homogeneity range (from $Ti_5Si_{2.8}$ to $Ti_5Si_{3.2}$) at 1000ºC due to formation silica-rich scale, while only Si-rich $Ti_5Si_{3.2}$ alloy remains oxidatively stable in air or nitrogen containing atmosphere. The accelerated oxidation occurs for stoichimetric Ti_5Si_3 alloys after a short time period in air or in nitrogen rich atmosphere. Presence of nitrogen alters the oxidation behavior of Ti_5Si_3 at elevated temperature by nucleation and growth of nitride subscale, which prevents the formation of protective silica-enriched layer by embrittlement of alloy via nitrogen dissolution in the structure and leads to the accelerated degradation. Formation of nitride subscale may be avoided when the concentration of N_2 is less than 50%.

In agreement with previous studies, $Ti_5Si_{3.2}$ and $Ti_5Si_3C_{0.5}$ alloys exhibited an excellent oxidation resistance in nitrogen containing atmosphere at 1000ºC. Two possible mechanisms may contribute to this: i) increasing a_{Si}/a_{Ti} favors the formation of SiO_2 over

TiO_2; ii) limited dissolution of nitrogen into interstitial site of Ti_5Si_3 structure inhibits the formation of the nitride subscale.

Silicide Coatings on Multiphase Mo-Si-B Composites

$MoSi_2$-based slilicide diffusion coatings were successfully deposited onto Mo_{ss}-based multiphase Mo-Si-B alloy via pack cementation, the coating process, oxidation behavior and interdiffusion behavior were investigated, the results obtained are summarized as follows:

1. In the pack siliconizing coating, a $MoSi_2$ layer was developed on the three-phase substrate ($Mo+Mo_3Si+Mo_5SiB_2$). After annealing or exposure to air at high temperature, $MoSi_2$ was transformed to T1 phase, which possesses poor oxidation resistance at elevated temperature.
2. Boride phases (MoB and Mo_2B_5) were successfully added to $MoSi_2$ coating either by co-deposition of B and Si or by a two-step process to attempt to improve the poor oxidation resistance of T1 interlayer, and the concentrations of boride phases can be controlled by adjusting the Si/B ratio in the pack mixture. However, those boride phases cannot be stabilized with either $MoSi_2$ or Mo_5Si_3 phases after exposure to high temperature. MoB phase was consumed by the formation of Mo_5Si_3 and the expelled boron diffused downward into substrate to form new borides. As a result, a diffusion zone with t Mo_5Si_3/(T2+MoB) layers formed.
3. Both silicide and boride-silicide coating can prevent the oxidation of Mo-4.3Si-1.1B alloy at 1100ºC in both static and cyclic conditions and estimated to be lasted for thousand of hours, while the coating is lost at 1600ºC due to rapid inter-diffusion between $MoSi_2$ and substrate, which leads to formation of poor

oxidation resistant T1 phase. The lifetime of $MoSi_2$-based coating is limited by Si depletion through the formation of T1 phase.

4. New coating design was proposed based on the diffusion data. T1-based Mo-Si-B coating will reduce the Si depletion rate from the surface by formation of slow growing Mo_3Si or T2 layer without sacrificing the oxidation resistance of the coating, therefore extending the coating lifetime above 1500ºC.

Evaluation of Phase Equilibria in the Nb-rich Portion of Nb-B System

The phase equilibria in the Nb-rich portion of Nb-B system has been evaluated experimentally using metallographic analysis and differential thermal analyzer (DTA). It was shown that Nb_{ss} (solid solution) and NbB are the only two primary phases in the 0-40 at.% B composition range, and the eutectic reaction $L \leftrightarrow Nb_{ss} + NbB$ exists, instead of generally accepted reaction: $L \leftrightarrow Nb_{ss} + Nb_3B_2$ as indicated in the Nb-B phase diagram. However, the Nb_3B_2 phase forms by the peritectoid reaction $Nb_{ss} + NbB \leftrightarrow Nb_3B_2$. DTA tests were conducted on annealed Nb-14B, Nb-16B, Nb-18B and Nb-40 alloys, and temperature and heat of phase transition were determined. The eutectic reaction ($L \leftrightarrow Nb_{ss} + NbB$) temperature was determined to found to be 2104±5˚C, and the heat of fusion was estimated to be 30.0±1.8 and 22.5±0.6 kJ/mol for Al_2O_3 and Rh, respectively. The heat event associated with peritectoid reactions was not observed in DTA traces perhaps due to sluggish solid state transformation, but the heat treatment experiments show that peritectoid temperature is above 1900˚C.

Acknowledgement

The United States Government has assigned the DOE Report number IS-T 2491 to this thesis. Notice: This manuscript has been authored, in whole or part, under Contract No. DE-AC02-07CH11358 with the U.S. Department of Energy. The U. S. Government retains and the publisher, by accepting the article for publication, acknowledges that the United States Government retains a non-exclusive, paid-up, irrevocable, world-wide license to publish or reproduce the published form of this manuscript, or allow others to do so, for U. S. Government purposes.

I would like to thank my major professor, Dr. Mufit Akinc, for his inspiration, invaluable guidance, assistance, and support for this work.

I would like to thank my co-major professor, Dr. Matthew J. Kramer for his guidance and oversight throughout this work.

I would like to thank Dr. Andrew J. Thom, whose valuable assistance, technical discussion and critical assessments are greatly appreciated.

I would like to thank my committee member, Dr. Mufit Akinc, Dr. Matthew J. Kramer, Dr. Alan I. Goldman, Dr. Brian Gleeson, Dr. Kurt Robert Hebert and Dr. Xiaoli Tan I also thank the staff and students in the department of materials science and engineering, Iowa State University, for their help and encouragement. My colleagues, Dr.Chuanping Li, Dr. Xiang Wei, Drew Enlow, Yusuf Yusufoglu, are particularly acknowledged for their assistance during this work.

Finally, special thanks to my parents for their support, understanding and encouragement during my study in USA.